UNIVERSITY OF CALIFORNIA

Los Angeles

Novel Techniques for Neuromodulation and Neural Signal Analysis

A dissertation submitted in partial satisfaction of the

requirements for the degree Doctor of Philosophy

in Bioengineering

by

Yushan Wang

2022

ABSTRACT OF THE DISSERTATION

Novel Techniques for Neuromodulation and

Neural Signal Analysis

by

Yushan Wang

Doctor of Philosophy in Bioengineering

University of California, Los Angeles, 2022

Professor Wentai Liu, Chair

Neuromodulation, targeting either the central nervous system or peripheral nervous system, is a viable therapy for many diseases, particularly for patients who are refractory to traditional treatments.

The first part of this thesis aims to develop the non-invasive neuromodulation technique targeting the central nervous system, specifically the brain with transcranial direct current stimulation (tDCS). Compared to the conventional tDCS which uses two large pad electrodes, high-density tDCS has recently received more attention. With the high-density electrode system, it is able to achieve better stimulation performance in terms of stimulation intensity and focality. To further improve the performance of this promising technique, we characterize the performance with respect to the electrode factor for the high-density tDCS system. In addition, we have developed an optimization algorithm, Stimulation with Balanced Focality and Intensity (SBFI), to guide the high-density system, which provides effective and focal stimulation. The robustness of

the computational model with standard tissue conductivity is also evaluated. The proposed technique can be applied to transcutaneous spinal cord stimulation (tSCS).

The second part aims to develop the electrical modulation technique targeting the peripheral nervous system, specifically one of the second brain organs - colon. Electrical stimulation has been demonstrated as an alternative approach to alleviate intractable colonic motor disorders. However, knowledge of optimal electrical stimulation modalities and regional specific functional effects of colonic neuromodulation is lacking. We have investigated the regional colonic motility in response to different electrical stimulation modalities. In addition, we have developed a novel and efficient technique employing bio-impedance characterization to monitor colonic motor activity.

The dissertation of Yushan Wang is approved.

Daniel T. Kamei

Hsian-Rong Tseng

Pei-Yu Chiou

Million Mulugeta

Wentai Liu, Committee Chair

University of California, Los Angeles

2022

TABLE OF CONTENTS

LIST OF FIGURES

LIST OF TABLES

LIST OF SUPPLEMENTARY MATERIALS

Supplementary video 1: tDCS graphic user interface tutorial.

Supplementary video 2: Example of circular muscle contraction in response to direct proximal electrical stimulation (10 Hz, 2ms, 15 mA) in the proximal colon of an anesthetized Yucatan male castrated pig.

Supplementary video 3: Example of longitudinal muscle contraction in response to direct distal electrical stimulation (10 Hz, 2ms, 15 mA) in the distal colon of an anesthetized Yucatan male castrated pig.

Supplementary video 4: Video animation of the heat map representation of the motility changes (luminal colonic pressure recordings) induced by direct proximal colon electrical stimulation (10 Hz, 2ms, 15 mA, 30 s ON) in the proximal colon. Pressure probe positions are represented on the x-axis going from proximal to distal (Left to Right). Stimulation starts at time t0 and lasts 15 min. As seen in the videos, the colon motor activity is composed of short-distance anterograde and retrograde propagating contractions, which are increased by stimulation. The data are mean ± SEM of recordings from n=7-13 pigs.

Supplementary video 5: Video animation of the heat map representation of the motility changes (luminal colonic pressure recordings) induced by CBVN (2 Hz, 4ms, 5 mA, 30 s ON) in the distal colon. Pressure probe positions are represented on the x-axis going from proximal to distal (Left to Right). Stimulation starts at time t0 and lasts 10 min. As seen in the videos, there is no consistent propagation for longer distances. The colon motor activity is composed of short-distance anterograde and retrograde propagating contractions (within 10cm). The data are mean ± SEM of recordings from n=7-14 pigs.

Supplementary video 6: Video animation of the heat map representation of the motility changes (luminal colonic pressure recordings) induced by S2 stimulation (2Hz, 0.3ms, 0.5mA pulse train with 30Hz, 3 pulses per train, 30s ON) in the colon. Pressure probe positions are represented on the x-axis going from proximal to distal (Left to Right). Stimulation starts at time t0 and lasts 10 min. As seen in the videos, S2 stimulation caused propagative contractions within the distal 10-19 cm region where the distal sensors are located. The data are mean ± SEM of recordings from n=3-4 pigs.

ACKNOWLEDGEMENTS

The first day I heard about the Biomimetic Research Laboratory is still vivid in my memory, as it seems like just yesterday. By then, I was an undergraduate student who had just gotten a chance to glance at the fascinating world of research. I was deeply excited about the research projects in the lab, thinking of the transformative changes the achievements can bring to numerous patients suffering from deafness, blindness, and paralysis. I'm still feeling lucky that I got a chance to contact Prof. Wentai Liu directly and share his passion on research in my junior year, which in the end opened up my gate to the realm of science. The past six years observed my struggling with problems, depression under failures, and most importantly happiness of success. At the end of this short journey, I would share my deepest appreciation with everyone.

First, I would like to express my highest respect and appreciation to my advisor Prof. Wentai Liu, who guided me throughout the way to become an independent researcher. Through countless discussions and brainstorms we had in the past six years, I learned from Prof. Liu what a true scholar should be: passionate, persisted, eager to learn and aiming perfectness all the time. His dedication to research works also inspired me and will embrave me in my career life.

I would also like to extend my sincere gratitude to my Ph.D. committee members, Prof. Daniel T. Kamei, Prof. Hsian-Rong Tseng, Prof. Pei-Yu Chiou, and Prof. Million Mulugeta not only for your valuable time and extreme patience but also for the insightful advice and contributions to my development as a researcher.

I also had the great pleasure of working with our collaborators, Prof. Million Mulugeta, Dr. Muriel Larauche, Dr. Karim Atmani, Dr. James C.Y. Dunn, and Dr. Genia Dubrovsky. I would like to say special thanks to Prof. Million Mulugeta and Dr. Muriel Larauche for the help and

guidance along the way. I've learned a lot from you. All these great works of colonic neuromodulation would not have been possible without the support and nurturing of you.

I would like to thank my lab mates, Yi-Kai Lo, Ying Li, Po-Min Wang, Stanislav Culaclii, Xu Han, Zhaoyi Liu, En-Lin Hsiang, Jonathan Brand, Jacqueline Chai, Kathleen Villaseñor, Yan-Peng Chen, Yu Nong and so on. I'll easily miss the days with you. In particular, I am grateful to Yi-Kai Lo and Ying Li for your constant support, invaluable guidance and selfless encouragement. I also want to thank my collaborators in the lab, Zhaoyi Liu, Jonathan Brand, Jacqueline Chai, and Kathleen Villaseñor, for your help with the realistic models in the balanced stimulation project, as well as Po-Min Wang and En-Lin Hsiang for your help of the colonic modulation and monitoring project.

I also want to thank my friends outside the lab for their love, companion and constant support.

Finally, yet importantly, I would like to express my deepest love to my family, specifically my parents and fiancée Yi Luo. I can't thank you enough.

Chapter 2 is a version of [Wang, Y.; Zhou, H.; Li, Y.; Liu, W. Impact of Electrode Number on the Performance of High-Definition Transcranial Direct Current Stimulation (HD-TDCS). In 2018 40th Annual International Conference of the IEEE Engineering in Medicine and Biology Society (EMBC); IEEE: Honolulu, HI, 2018; pp 4182–4185. https://doi.org/10.1109/EMBC.2018.8513379.], [Qin, J.; Wang, Y.; Liu, W. Current Design with Minimum Error in Transcranial Direct Current Stimulation. In Brain Informatics; Wang, S., Yamamoto, V., Su, J., Yang, Y., Jones, E., Iasemidis, L., Mitchell, T., Eds.; Springer International Publishing: Cham, 2018; Vol. 11309, pp 52–62. https://doi.org/10.1007/978-3-030-05587-5_6.], [Wang, Y.; Liu, W. Optimization for Transcutaneous Spinal Cord Stimulation with a Multi-electrode Array. Program No. 066.10. 2019 Neuroscience Meeting Planner. Chicago, IL: Society

for Neuroscience, 2019. Online.], and [Wang, Y.; Brand, J.; Liu, W. Stimulation Montage Achieves Balanced Focality and Intensity. Algorithms vol. 15, no. 5, 2022, https://doi.org/10.3390/a15050169.], Chapter 3 is a version of [Larauche, M.; Wang, Y.; Wang, P.-M.; Dubrovsky, G.; Chen, Y.-P.; Dunn, J.; Taché, Y.; Liu, W.; Mulugeta, M. Regional Colonic Motility Response to Colon Tissue, Celiac Vagus and Sacral Nerve Electrical Stimulation. The FASEB Journal 2020, 34 (S1), 1–1. https://doi.org/10.1096/fasebj.2020.34.s1.09888.], [Larauche, M. H.; Wang, Y.; Wang, P.-M.; Dubrovsky, G.; Lo, Y.-K.; Hsiang, E.; Dunn, J. C.; Taché, Y.; Liu, W.; Mulugeta, M. The Effect of Colonic Tissue Electrical Stimulation and Celiac Branch of the Abdominal Vagus Nerve Neuromodulation on Colonic Motility in Anesthetized Pigs. Neurogastroenterology & Motility 2020, 32 (11). https://doi.org/10.1111/nmo.13925.], and [Wang, Y.; Wang, P.-M.; Larauche, M. H.; Mulugeta, M.; Liu, W. Monitoring Colon Motility in Anesthetized Pig in Response to Direct Distal Colon Stimulation with Bio-impedance. Submitted to Scientific Reports.]. Our researches were supported in part by the Bioengineering Department fellowships, NIH OT2 OD024899, and the CURE: Digestive Diseases Research Center P30 DK 41301, Dr. Patrick Soon-Shiong Endowment Funds, and Chan Soon-Shiong Bionic Engineering Center at UCLA (Project Number: CNSI-2012-1184), all at UCLA.

VITA

2012-2016 B.S. Precision Instruments, Tsinghua University, China

PUBLICATIONS AND PRESENTATIONS

Wang, Y.; Wang, P.-M.; Larauche, M. H.; Mulugeta, M.; Liu, W. Monitoring Colon Motility in Anesthetized Pig in Response to Direct Distal Colon Stimulation with Bio-impedance. Submitted to *Scientific Reports*.

Wang, Y.; Brand, J.; Liu, W. Stimulation Montage Achieves Balanced Focality and Intensity. Algorithms vol. 15, no. 5, 2022, https://doi.org/10.3390/a15050169.

Larauche, M. H.; **Wang, Y.**; Wang, P.-M.; Dubrovsky, G.; Lo, Y.-K.; Hsiang, E.; Dunn, J. C.; Taché, Y.; Liu, W.; Mulugeta, M. The Effect of Colonic Tissue Electrical Stimulation and Celiac Branch of the Abdominal Vagus Nerve Neuromodulation on Colonic Motility in Anesthetized Pigs. Neurogastroenterology & Motility 2020, 32 (11). https://doi.org/10.1111/nmo.13925.

Wang, Y.; Larauche, M. H.; Wang, P.-M.; Dubrovsky, G.; Dunn, J. C.; Tache, Y.; Liu, W.; Mulugeta, M. Mo1152 Spectral Analysis of Frequency of Colon Motility in Anesthetized Pigs: Effect of Direct Colon Tissue and Autonomic Nerve Electrical Stimulation. Gastroenterology 2020, 158 (6, Supplement 1), S-804. https://doi.org/10.1016/S0016-5085(20)32693-7.

Larauche, M.; **Wang, Y.**; Wang, P.-M.; Dubrovsky, G.; Chen, Y.-P.; Dunn, J.; Taché, Y.; Liu, W.; Mulugeta, M. Regional Colonic Motility Response to Colon Tissue, Celiac Vagus and Sacral

Nerve Electrical Stimulation. The FASEB Journal 2020, 34 (S1), 1–1. https://doi.org/10.1096/fasebj.2020.34.s1.09888.

Wang, P.-M.; Culaclii, S.; Seo, K. J.; **Wang, Y.**; Fang, H.; Lo, Y.-K.; Liu, W. Challenges in the Design of Large-Scale, High-Density, Wireless Stimulation and Recording Interface. In Interfacing Bioelectronics and Biomedical Sensing; Cao, H., Coleman, T., Hsiai, T. K., Khademhosseini, A., Eds.; Springer International Publishing: Cham, 2020; pp 1–28. https://doi.org/10.1007/978-3-030-34467-2_1.

Wang, Y.; Liu, W. Optimization for Transcutaneous Spinal Cord Stimulation with a Multi-electrode Array. Program No. 066.10. 2019 Neuroscience Meeting Planner. Chicago, IL: Society for Neuroscience, 2019. Online.

Qin, J.; **Wang, Y.**; Liu, W. Current Design with Minimum Error in Transcranial Direct Current Stimulation. In Brain Informatics; Wang, S., Yamamoto, V., Su, J., Yang, Y., Jones, E., Iasemidis, L., Mitchell, T., Eds.; Springer International Publishing: Cham, 2018; Vol. 11309, pp 52–62. https://doi.org/10.1007/978-3-030-05587-5_6.

Wang, Y.; Zhou, H.; Li, Y.; Liu, W. Impact of Electrode Number on the Performance of High-Definition Transcranial Direct Current Stimulation (HD-TDCS). In 2018 40th Annual International Conference of the IEEE Engineering in Medicine and Biology Society (EMBC); IEEE: Honolulu, HI, 2018; pp 4182–4185. https://doi.org/10.1109/EMBC.2018.8513379.

CHAPTER 1

Introduction

Neuromodulation has been widely applied to fundamental research to better understand the nervous systems as well as to the clinical therapy of a variety of diseases. Well-known examples include manipulating neural activities in the brain to modulate the brain functions [1]–[3], spinal cord implants to restore the motor function after spinal cord injury [4]–[6], and gastrointestinal implants to monitor and treat GI motility disorder[7]–[9]. These applications require continuous technological advancement and knowledge of specific functional effects. Despite technological advances to date, there are still challenges to overcome. Concretely, an effective stimulation should be capable of selectively activating the desired neurons of interest while avoiding others, making selectivity and focality critical concerns in electrical stimulation systems. However, in the high-density stimulation interface with the conventional stimulation paradigm, the resolution of stimulation is poor as the delivered charge from the stimulating electrodes would inevitably spread to nearby tissues. An in vitro study to perform and validate focalized stimulation using a multi-electrode array has been conducted in [10]. However, in order to further the stimulation focality/selectivity, it is essential to develop a stimulation approach that can focalize the electrical field in the desired region with ease. In addition, while enthusiasm is high for this popular therapeutic approach, the optimal neuromodulation modalities, effects, and mechanisms are not well known, especially when targeting the regions/organs with complex functions. The brain and colon (known as a part of the second brain) are the most representative examples. Overcoming these challenges is desperately needed to continue driving the technology toward better modulation effects and filling the knowledge gap. This thesis aims at developing advanced optimization

methods to provide focalized and effective neural stimulation with a multi-electrode system, as well as region-specific functional mapping and monitoring of the colonic neuromodulation.

For neuromodulation, we mainly focus on noninvasive electrical stimulation techniques with a high-density electrode system targeting the cortex. Benefits of a high-density electrode system include the ability to target multi-site stimulation, avoid specified regions, and provide more flexible stimulation configurations with the same target and safety constraints. Furthermore, it is critical to achieving spatially precise stimulation. Performing selective and focalized stimulation to specific neurons would greatly ameliorate the stimulation efficacy by avoiding the undesired spread of electrical charge. And the focalized stimulation can only be accomplished by a high-density electrode system. There are many factors that can impact the stimulation performance, such as the number of electrodes in the system and the computational model used for the system's current assignment. The first contribution of this dissertation systematically studies the influence of different electrode-related factors on the performance of stimulation and develops optimization algorithms, which guide developments of the high-density electrode system and support focalized/selective stimulation. Further, it is important to recognize the gap between the computational model and clinical application. Therefore, this dissertation also explores the robustness of the computational model and prepares for future clinical studies.

Electrical stimulation is also believed to be effective in modulating the part of the second brain – colon by applying directly to the colonic tissue or the nerves of the autonomic nervous system. The interest in this electroceutical-neuromodulation is increasing, an alternative approach to alleviate intractable colonic motor disorders. However, the knowledge of region-specific functional effects of colonic neuromodulation and effective electrical stimulation modalities is lacking. Furthermore, the colonic motility, playing a critical role in accessing the effectiveness of

these emerging therapies, is complex, and its accurate analysis remains a challenge. Various methods have been proposed to monitor the colonic motility, and while each has contributed to a better understanding of colon motility, a significant limitation has been the spatial and temporal low-resolution in colon motility data acquisition and analysis. The second contribution of this dissertation investigated the regional colonic motility response to different electrical stimulation modalities, which provides a foundational basis to guide safe and effective neuromodulation for patients suffering from intractable colonic motility disorders. On top of that, this dissertation develops the spectral analysis of the intracolonic pressure to uncover important features (frequency pattern and power) of intestinal phasic contractions under different electrical stimulation protocols. Furthermore, a novel technique based on bio-impedance characterization is proposed and validated to monitor colonic motor activity at high spatial and temporal resolution.

Chapter 2 aims to improve the performance of the high-density electrode system in focalized stimulation. We first establish a computational model of high density transcranial direct current stimulation (tDCS) and systematically study the influence of different electrode-related factors on the stimulation performances. Then, the optimization algorithm using a regularization matrix $\boldsymbol{\lambda}$ is developed to explore the balance between stimulation intensity and focality. The simulation study is designed such that the performance of state-of-the-art algorithms and the proposed algorithm can be compared via quantitative evaluations. The results show that the proposed algorithm, with a reasonable number of electrodes, not only achieves desired intensity but also smaller target error and better focality. Robustness analysis indicates that the simulation results with the computational model are stable within the ranges of the scalp and Cerebrospinal Fluid (CSF) conductivities, while the skull conductivity is most sensitive and should be carefully considered in real clinical

applications. The same strategies have been demonstrated to be applicable to the transcutaneous spinal cord stimulation (tSCS).

Chapter 3 focuses on the functional mapping and modulation techniques of the colonic nervous system. In this dissertation, we investigated the regional colonic motility response to electrical stimulation of the colonic tissue and nerves in an anesthetized porcine model and demonstrated the effective stimulation modalities. In addition, we propose a novel technique based on bio-impedance characterization to monitor colonic motor activity. We demonstrate that the proposed bio-impedance-based method can monitor colonic motor patterns at high spatial and temporal resolution.

Chapter 4 summarizes the dissertation and points out some future directions.

CHAPTER 2

Non-invasive neuromodulation Achieves Balanced Focality and Intensity

The technique of transcranial direct current stimulation (tDCS) has been recently attracting more and more attention in research and clinic applications to elicit modulation of neural activities non-invasively for the treatment of psychiatric conditions and neurological diseases. Although tDCS has a lot of practical advantages such as portability, flexibility and tolerable stimulation duration, it faces several challenges such as the limited stimulation intensity and focality of detecting the stimulating electric field. To address these issues, high-density tDCS has been developed in the past. With a high-density electrode system, high-density tDCS provides a higher degree of freedom to achieve better stimulation results.

In this chapter, we first introduce the background of the high-density tDCS. To improve the high-density tDCS, we establish the computational model and explore the factors that affect tDCS performance. Stimulation with Balanced Focality and Intensity (SBFI), an optimization-based algorithm, is proposed to further investigate the technique with balanced the stimulation focality and intensity. Several state-of-the-art methods are introduced and compared with SBFI. The advantages and disadvantages of different optimization algorithms are discussed. Then, the robustness of the computational model is studied, and a graphic user interface is built for future clinical applications. Moreover, we extend this study to another non-invasive neuromodulation system (transcutaneous spinal cord stimulation tSCS). We demonstrate that the proposed techniques can be applicable to tSCS. SBFI can enable the high-density electrode system to maintain the stimulation intensity and affects fewer non-target spinal cord segments, indicating a great potential for future implementation.

2.1 Introduction

As a non-invasive neuromodulation method, transcranial direct current stimulation (tDCS) shows therapeutic potential to treat many brain disorders and improve brain functions, such as major depression [11]–[13], epilepsy [14]–[16], and Parkinson's disease [17]–[19]. It also has garnered great interest because it may benefit healthy individuals as well [20]–[23]. Conventional tDCS applies a constant, low direct current through two large pad electrodes to stimulate a specific brain region. It is challenging to achieve accurate activation or inhibition at a specific region without interfering with other regions in the brain. Numerous efforts have been made to improve this promising technique, such as using multiple electrodes to achieve focalized EEG-guided stimulation. For example, the GTEN system (EGI, Eugene, OR, USA) with 256 channels integrated the reciprocity theorem and EEG-based source localization tools such as sLORETA. However, it has many deficiencies. First of all, state-of-art source localization algorithms such as gFOTV can improve its localization accuracy and degree of focalization [24], [25]. Importantly, the density of the electrode system does affect stimulation outcomes, and 256 may not be high enough to reach the plateau [26]–[29]. The most important drawback is that the reciprocity theorem may not be ideal, especially in the multiple target case. It may stimulate the average location of these targets and result in a broadly distributed stimulation pattern. Consequently, one of the emerging challenges of utilizing a high-density electrode system for tDCS is to determine the optimal current at each electrode. An optimal current pattern will enable high-density electrode systems to provide stimulation with high focality, accuracy, and intensity.

So far, optimization-based methods are the most popular solution to assign injected current values. As an overdetermined problem, the Least Squares solution is a straightforward approach

[30], which minimizes the second-order error term. Considering the safety issue in clinical use, constraints are then added when applying the algorithm; thus, it can be referred to as the Constrained Least Squares method (CLS). Its optimal current pattern often produces relatively focal stimulation but low stimulation intensity; one possible explanation for this is that the target region is generally tiny compared to the whole brain. To overcome this challenge, the Least Squares method has been improved by assigning weight to balance the tiny target region and large non-target ones in a technique called the Weighted Least Squares method [30], [31]. It is able to produce higher stimulation intensity; however, the weight factor must be given by the clinician, which is a non-trivial task. Another developed technique optimizes for the intensity at the target region and is named the Max Intensity (MI) method [27], [32]. This method tends to achieve high stimulation intensity but is more likely to activate large non-target areas. Thus, this motivates the introduction of more constraints on non-target areas to improve the MI method [33], [34]. However, the additional constraints may lead to no feasible solution set and also longer computational time. These improvements all indicate the key point behind this optimization problem—that is, to find ways of balancing the stimulation intensity and focality. One novel solution named Linearly Constrained Minimum Variance (LCMV) [30] adopts ideas from the beamforming problem. The algorithm has a hard constraint in that the stimulation intensity at the target region is enforced to be exactly equal to the desired one, while a cost function minimizes the energy of the non-target regions. This strategy is aimed at ensuring the stimulation's effectiveness but has pitfalls. LCMV minimizes the effects on the non-target areas under the premise that the hard constraint is fulfilled. When the desired electric field at the target regions is difficult to achieve, it can greatly sacrifice the non-target region and produce a spread-out electric field distribution. In the worst case, it may even fail to attain the hard constraint, thus giving no feasible solution.

To balance the trade-off and overcome these pitfalls, we propose a new method combining the principles of LCMV and MI. The new method, *Stimulation with Balanced Focality and Intensity (SBFI)*, maximizes the energy in the target region and minimizes the rest of the energy in non-target regions. We also adopt an idea from the Weighted Least Squares method by adding a stimulation parameter $\boldsymbol{\lambda}$ in SBFI to balance the intensity and focality of the target regions and non-target regions. Computational simulation experiments were conducted using the aforementioned methods and the proposed SBFI method. The quantitative results show that SBFI achieves better performance in balancing the stimulation intensity and focality for both single and multiple target studies. Robustness experiments indicate that the results are stable with different scalp and cerebrospinal fluid (CSF) conductivities, while skull conductivity is most sensitive and should be carefully considered in real clinical applications. The proposed optimization method SBFI shows good robustness among tested methods in terms of the overall electric field distribution deviations and the maximum intensity changes at the target area.

2.2 Framework and Computational Model

2.2.1 Mathematical Formulation

To formulate this optimization problem, let's consider the head as a volume conduction model, which consists of multiple tissues, each with different electrical conductivity. Furthermore, the whole volume is discretized into small voxels. The cortex now has n elements, and the electric field in the cortex resulting from the electrical stimulation is denoted by $\boldsymbol{e}_{3n\times 1}$. The stimulation is expected to have a desired electric field distribution in the application, which is denoted by $\boldsymbol{e}_d$.

And $\boldsymbol{e}_0$, as a submatrix of $\boldsymbol{e}_d$, represent the specified electric field intensity and orientation at the target(s). For a stimulation system with m electrodes on the scalp, we use $\boldsymbol{s}_{m\times 1}$ to denote the injected current in the system. Considering the fact that head tissues are mainly resistive when tDCS is applied, the electric field distribution can be regarded as quasi-static. Under this condition, the applied current $\boldsymbol{s}_{m\times 1}$ and electric field $\boldsymbol{e}_{3n\times 1}$ are linearly related as:

$$\boldsymbol{e}_{3n\times 1} = \boldsymbol{K}_{3n\times m} \cdot \boldsymbol{s}_{m\times 1}$$

The coefficient matrix $\boldsymbol{K}_{3n\times m}$, known as the lead field matrix, provides the mapping information between the injected currents of the electrode system and the electric field value at each voxel of the brain. The $\boldsymbol{K}_{3n\times m}$ matrix can be obtained by constructing a realistic volume conduction model and solving Maxwell's equations.

To guarantee the stimulation is within the safety limits, it is necessary to introduce constraints for the optimization model. Generally, there are three common safety concerns. First, the sum of all current inflow should be equal to the sum of all current outflow based on the charge conservation law

$$\sum s_i = 0$$

Second, the current injected into each electrode cannot exceed I_{max}. This is especially important for high-density electrode systems to avoid side effects such as pain and skin injury. This constraint can be written as

$$|s_i| \leq I_{max}, \text{for any } i$$

Lastly, we limit the sum of all current inflow to the body. If we use I_{total} to represent the maximum sum currents injected into the body, then the constraint will be

$$\sum |s_i| \leq 2I_{total}$$

In our study, we set $I_{max} = 2\text{mA}$, and $I_{total} = 4\text{mA}$, which are reported to be safe [35]–[37].

The feasible sets of the optimization model are defined as:

$$\boldsymbol{s} = \left\{\boldsymbol{s} \in \mathbb{R}^m : \sum s_i = 0, |s_i| \leq I_{max}, \sum |s_i| \leq 2I_{total}\right\}$$

Then, we introduce the l_∞-norm and the l_1-norm of a vector, i.e., $\|\mathbf{x}\|_\infty = \max_{1 \leq i \leq m} |x_i|$ and $\|\mathbf{x}\|_1 = \sum |x_i|$ for any $\mathbf{x} \in \mathbb{R}^m$. Using the vector norms, we can get an equivalent form:

$$\boldsymbol{s} = \{\boldsymbol{s} \in \mathbb{R}^m : \boldsymbol{s}^T \mathbf{1} = 0, \|\boldsymbol{s}\|_\infty \leq I_{max}, \|\boldsymbol{s}\|_1 \leq 2I_{total}\}$$

where $\mathbf{1} = (1, \ldots, 1)^T \in \mathbb{R}^m$.

2.2.2 Quantitative Evaluation of the Stimulation Performance

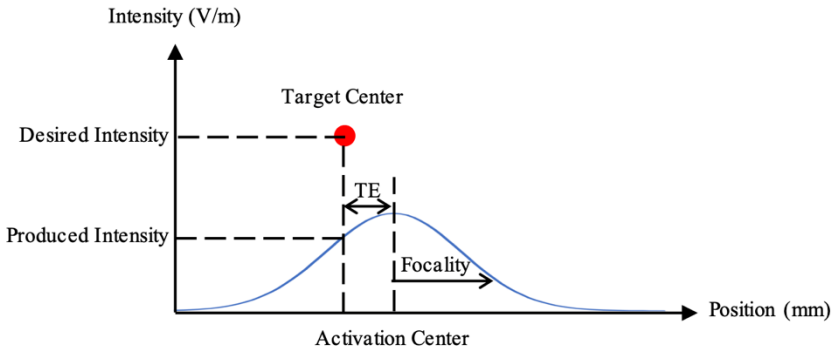

Figure 2.1: The illustration of quantitative evaluations.

To evaluate the stimulation performance fairly and comprehensively, we use four quantitative evaluation criteria, i.e., the stimulation intensity, precision, accuracy and the electrode number. The quantitative evaluation illustration is shown in Figure 2.1. Note that we evaluate the performance of each target region separately if we stimulate the multiple targets at the same time.

First is the stimulation intensity in volts per meter, which shows the maximum electric field of the target region. In general, higher intensity is preferred. An intensity of 0.1 ~ 0.3V/m is reported

to be efficient [30], [38], [39]. In addition, clinical application favors the result that is close to the desired electric field distribution in the target region.

$$E = \boldsymbol{e}_{max} = max(\boldsymbol{e}_{tar})$$

Secondly, the target error (TE) is defined as the Euclidean distance between the mass centers of the target and the solution regions [28].

$$TE = \|\boldsymbol{MC}_0 - \boldsymbol{MC}\|_2, \qquad (\boldsymbol{MC}_0)_j = \frac{\sum_i (\boldsymbol{e}_0)_{ij} \cdot \boldsymbol{p}_{ij}}{\sum_i (\boldsymbol{e}_0)_{ij}}, \qquad (\boldsymbol{MC})_j = \frac{\sum_i (\boldsymbol{e})_{ij} \cdot \boldsymbol{p}_{ij}}{\sum_i (\boldsymbol{e})_{ij}}$$

where $j \in \{x, y, z\}$, $\boldsymbol{p}_i$ is the coordinates of the ith voxel. The mass center of the target region and the activation region is $\boldsymbol{MC}_0$ and $\boldsymbol{MC}$, respectively. With units of millimeters, TE is a way of evaluating the stimulation accuracy: the smaller the TE, the higher the accuracy.

The third is the focality [28] measured in millimeters, which is represented by the radius in which the cumulative energy is *half* of the total energy. If we use $\Gamma(r)$ to represent the voxel set within a distance r from the center of the target region, $E(\boldsymbol{r})$ is the portion of the energy of $\Gamma(r)$.

$$\boldsymbol{r}_{0.5} = \boldsymbol{r}|_{E(\boldsymbol{r})=0.5}, \qquad E(\boldsymbol{r}) = \frac{\sum_{i \in \Gamma(\boldsymbol{r})} \|\boldsymbol{e}(\boldsymbol{r}_i)\|_2^2}{\sum_i \|\boldsymbol{e}(\boldsymbol{r}_i)\|_2^2}$$

Focality indicates the stimulation precision. Smaller values of $\boldsymbol{r}_{0.5}$ indicate that most of the energy is concentrated in a smaller region, and thus off-target brain regions are less likely to be activated.

In addition, the number of electrodes used in the montage is provided, which reflects the technology limitation.

2.2.3 Realistic Head Model and Electrode Model

The computational realistic head model utilized in our study is derived from the anatomical FieldTrip template [40] from the Statistical Parametric Mapping (SPM) Canonical Brain, which provides anatomical information on the scalp, skull, cerebrospinal fluid (CSF), and cortex. The Boundaries of all the tissue layers of the model were first saved in stereolithography (STL) format and then converted to the solid models using SolidWorks (Dassault Systèmes SOLIDWORKS Corp., Waltham, Massachusetts, USA). The conductivity values are adopted from the literature [30], where $\sigma_{Scalp} = 0.465\,\mathrm{S/m}$, $\sigma_{Skull} = 0.01\,\mathrm{S/m}$, $\sigma_{CSF} = 1.65\,\mathrm{S/m}$, and $\sigma_{Cortex} = 0.2\,\mathrm{S/m}$ respectively.

In addition, the electrode model was constructed using SolidWorks, the location of which is based on the international electroencephalography (EEG) system. The electrodes consist of the metal layer and the gel layer, where the gel layer lays between the metal and scalp as the real clinical application. Both the layers have the same diameter and thickness of 1mm.

As described previously, the injected current at each electrode has a linear relationship with the electric field value in each voxel, which is exactly the single element of the lead field matrix. Using FEM and solving the Laplace equation in the realistic head model, we obtain one column of $\boldsymbol{K}_{3n\times m}$ by assigning a unit current (1mA) to that corresponding electrode and then complete the lead field matrix by repeating m times. All the simulation work is done by COMSOL Multiphysics (COMSOL Inc., Burlington, MA).

2.2.4 Process Automation

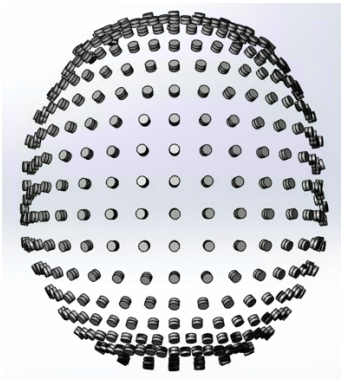

Figure 2.2: High-density electrode model.

The electrode modeling and simulation are time-consuming and mindless work. Each electrode is first built and then adjusted its orientation normal to the scalp surface manually, which will be repeated m times to model a m-electrode system. From our experiences, it took more than 48 hours to build 342 electrodes (Figure 2.2) and more than 7 days to run the 342 simulations to obtain the lead field matrix as described in the previous section. Those processes require more time as the number of electrodes increases. Besides, errors can easily occur in any step of those manual construction, including missing electrodes and missing orientation adjustments. Those errors could be noticed eventually in the simulation procedure. However, the errors in simulation, like the repeated simulation of the same electrode mistakenly, may be hard to identify and lead to failure. Therefore, process automation is proposed to overcome those limitations and resolve the problems.

2.2.4.1 SolidWorks Macro Control

Macro, based on visual basic syntax, is used to operate SolidWorks to achieve electrode construction automatically. The input data required by Macro includes one single electrode template, electrode positions, and the normal direction of each electrode. The application of Macro

can significantly save the high-density electrode system construction time; for instance, it decreased the operation time from more than 48 hours to 30 minutes for 342-electrode system modeling.

2.2.4.2 COMSOL Java Control

Java is proposed to control the COMSOL to achieve electrode simulation automatically. With the basic physics settings, the java script can control COMSOL conduct simulation for one electrode after another without additional work. The simulation of a 342-electrode system can be done in a day without error.

2.3 Influence of Different Electrode Factors on High-Density tDCS Performance

The performance of high-density tDCS is influenced by several electrode-related factors, such as electrode number, electrode size, and electrode shape. Fernandez-Corazza et al. compare 128 and 256 electrode cases and find that greater electrode density improves focality, directionality and intensity parameters [26]. Faria et al. have shown that smaller stimulation electrode produces a more focal current density distribution when using two circle electrodes system [41]. Coincidentally, Nitsche et al. find that stimulation focality can be improved by reducing the size of the stimulation electrode and by increasing the size of the reference electrode [42]. In general, previous related studies are isolated and based on the conventional system or the ring electrode montage. A systematic study of the influence of various electrode-related factors on the performance of high-density tDCS is still missing. To further improve the performance of high-density tDCS, it is important to characterize the performance with respect to the electrode factor.

Herein, we proposed a systematic study based on the high-density electrode system. Electrode number, electrode size, and electrode shape were the three factors proposed to be studied. The most common optimization method Least Square with safety constraints was applied, and the aforementioned evaluation criteria were compared to quantitatively analyze how these factors will influence tDCS performance.

$$\boldsymbol{s} = arg\min_{\boldsymbol{s}} \|\boldsymbol{K}\boldsymbol{s} - \boldsymbol{e}_d\|^2$$

The desired e-field intensity $\boldsymbol{e}_d$ of the optimization problem is $0.3\ \mathrm{V/m}$ in our experiments to meet the effectiveness requirement as described. Different targets were chosen: target 1 is the motor cortex region, target 2 is the auditory cortex, and target 3 is the left dorsolateral prefrontal cortex which is identified to be important for depression treatment. With those different regions of target, we aimed to analyze various target conditions that may occur in clinical use in order to draw a pervasive conclusion. Also, considering that the different target voxels at the specific location may influence the performance, ten sets of target voxels in each region were randomly selected to evaluate the average performance. Thus, in addition to the quantitative evaluation criteria, we also used Box-plot to demonstrate the numerical analysis.

2.3.1 Influence of Electrode Number

We first studied how the number of electrodes impacts the performance of high-density tDCS. We constructed several high-density electrode systems of 21, 32, 64 and 342 electrodes (Figure 2.3). The diameter of each electrode was fixed to 6mm.

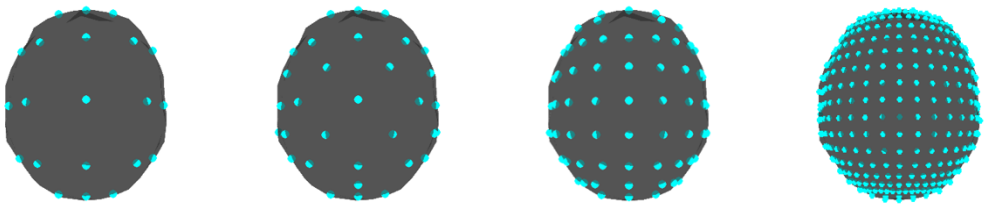

Figure 2.3: The model of multi-electrode systems of 21, 32, 64 and 342 electrodes.

Comparison of the focality, TE, and intensity has been done at different selected target regions by varying the electrode number. Figure 2.4 shows the results of the normalized E-field distribution. Each column represents a specific target region, where from left to right are the motor cortex, auditory cortex and left dorsolateral prefrontal cortex. And the four rows are the results of 21, 32, 64, and 342 electrodes.

Clearly, the visual inspection shows that the focusing capability is significantly improved as the number of electrodes increases. In all three stimulation cases, the e-field created by 21-electrode stimulation is broadly distributed, which almost undesirably spreads the half of the cortex. When the electrode number n is equal to 32, the activation region is smaller than the 21-electrode stimulation. If the electrode number is set at 64, the e-field distribution is much more focal. Moreover, when the electrode number reaches 342, the focusing capability is greatly improved, and the focality can be as small as 1cm.

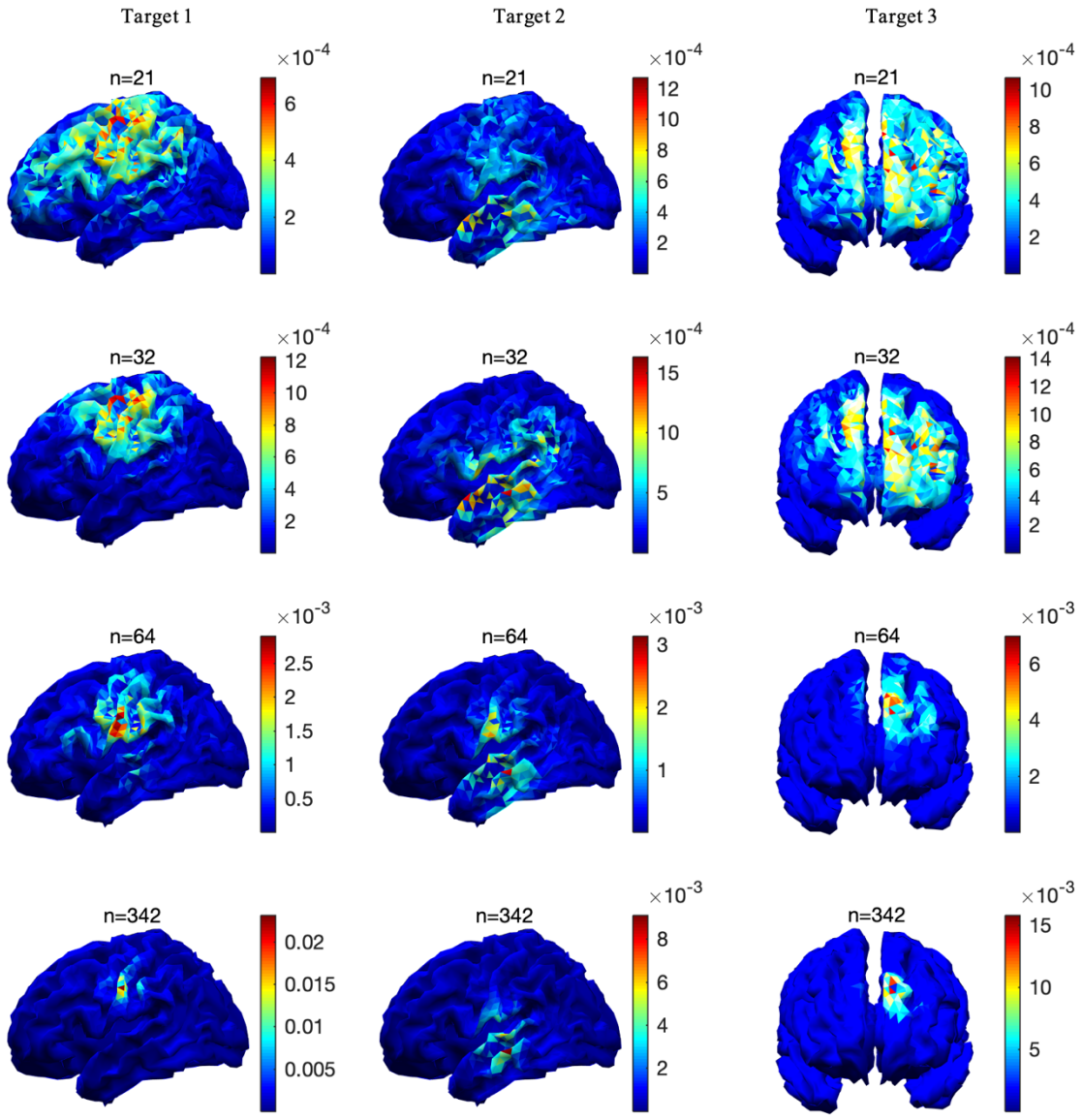

Figure 2.4: Performance comparison at the different number of electrodes (21, 32, 64, and 342).

Furthermore, several sub-regions of each target area are chosen for the evaluation of focality, TE, and intensity. The results of all three target regions are in accord. The numerical result for each target is shown in Figure 2.5 using box plots, including the lower quartile, median and upper quartile. From top to bottom, the three rows are the results of intensity, TE, and focality. The range

indicates the performance varies at different target locations. And the ranges of both focality and TE are the smallest when the electrode number is 342, which indicates that precise and accurate stimulation can be obtained by a configuration of a higher electrode number.

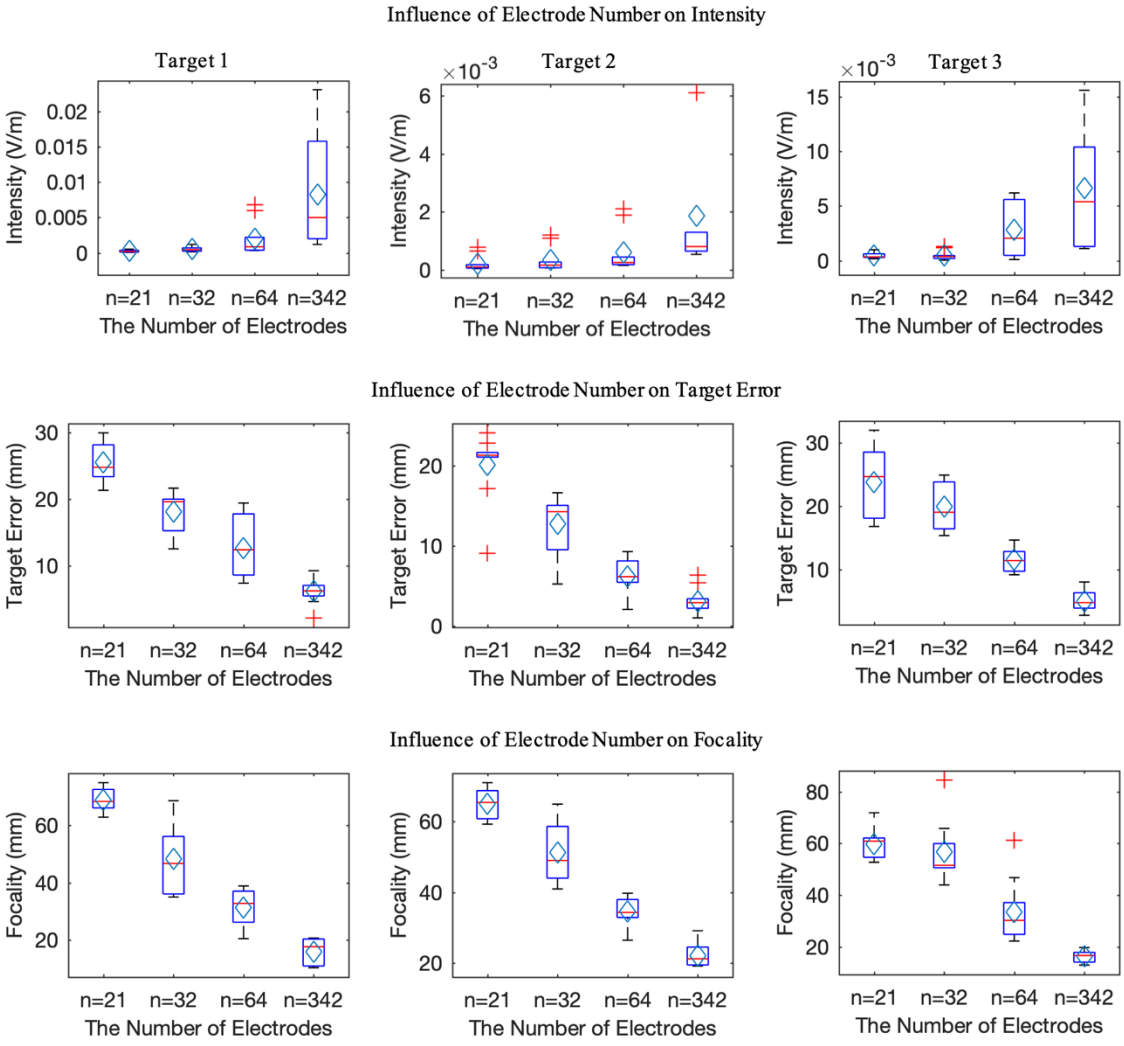

Figure 2.5: Box and whisker plot shows the trends at different electrode numbers when stimulating different target regions.

The red bar represents the median value, and the diamond in each box indicates the average value. The “whiskers” above and below the box show the values of the highest non-outlier and lowest non-outlier. The red cross sign represents the outliers.

Though the range in the intensity figure is the largest, the intensity of the target region is improved. The red bar in each "box" represents the median value, which decreases in focality and TE and increases in intensity with more electrodes. A similar trend occurs in the diamond plotted in each "box" representing the average value.

The results of the electrode currents obtained by the algorithm show that the optimal currents $\boldsymbol{s}$, far from reaching the safety constraints, are not enough for applications. This indicates that the electrodes do not fully use the allowable current. The fewer electrode number, the worse the phenomena. To make full use of the current and results in the desired higher intensity without enlarging the focality and TE, we could increase the current by multiple a scaling factor (t) to reach the safety constraints. It is very clear that the formulation of $t \times \boldsymbol{s} = \boldsymbol{s}^* = arg\min_{\boldsymbol{s}} \|\boldsymbol{K}\boldsymbol{s} - \boldsymbol{te}_d\|^2$ will not change the focality and TE. This remedy method provides a way of increasing the intensity created by different electrode systems. Thus, the electrode system can make full use of the allowable current and produces the highest intensity while maintaining the optimal focality and TE. Comparing the intensity of each system after this method, the 342-electrode system still achieves higher intensity than other systems with smaller electrode numbers. Considering the focality and TE, the values will not be changed. As we discussed in the previous paragraph, the focusing capability and stimulation accuracy are greatly improved as the number of electrodes increases.

Combining together the E-field distribution, focality, TE, and intensity, it indicates that the increase of the electrode number can achieve better performance in focusing capability, stimulation accuracy, and intensity of HD-tDCS regardless of the target regions.

As the conclusion suggests, we can achieve better performance of tDCS by increasing the number of electrodes regardless of the target types and target areas. Thus, we propose to build a

high-density electrode system. The placement of high-definition tDCS is based on the international EEG system, including the 10/20, 10/10, and 10/5 systems [43], [44]. The ”20”, “10”, and “5” refer to the fact that the actual distances between adjacent electrodes are either 20%, 10%, or 5% of the total front-back or right-left distance of the skull.

Currently, the highest electrode number is 342, whose placement is based on the 10/5 EEG system. However, more electrodes are required, and this 10/5 system is not enough. Thus, we proposed to extend the 10/5 system to the 10/2.5 system. As the definition indicates, the distance between adjacent electrodes will be 2.5% of the whole length. The extended 10/2.5 system is shown in Figure 2.6.

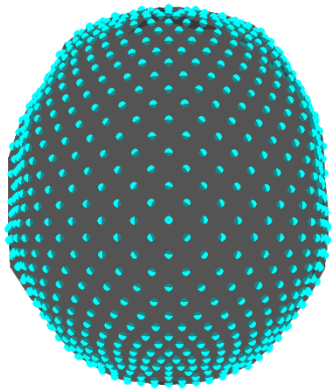

Figure 2.6: The extended 10/2.5 system.

Considering the 10% circle, based on our analysis, the number of electrodes in this 10% circle (N) can be calculated by the following formula.

$$N = 2^{2n+4} + 2^{n+1} + 1$$

where n reflects the distance between adjacent electrodes as a percentage of the total front-back or right-left distance of the skull. For example, $n = 0$ for the 10/20 system. The exact values are in the table below. Additional electrodes can also be placed outside the 10% circle, which is

based on the specific need, like the cheek. So, there will be more than a thousand electrodes when applying the new 10/2.5 system.

Table 2.1: The 10/2.5 system

System	n	N
10/20	0	19
10/10	1	69
10/5	2	265
10/2.5	3	1041

2.3.2 Influence of Electrode Size

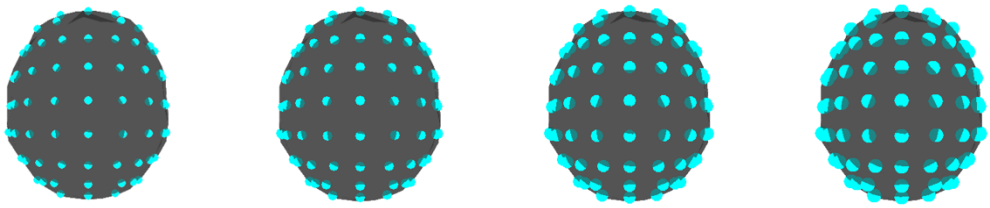

Figure 2.7: The model of multi-electrode systems with 6mm, 8mm, 12mm and 16mm in diameter.

We then explored how the size of electrodes impacts the performance of high-density tDCS. The diameters we studied vary from 6mm, 8mm, 12mm, to 16mm (Figure 2.7). The number of all those electrode models is 64, and they share the same center position.

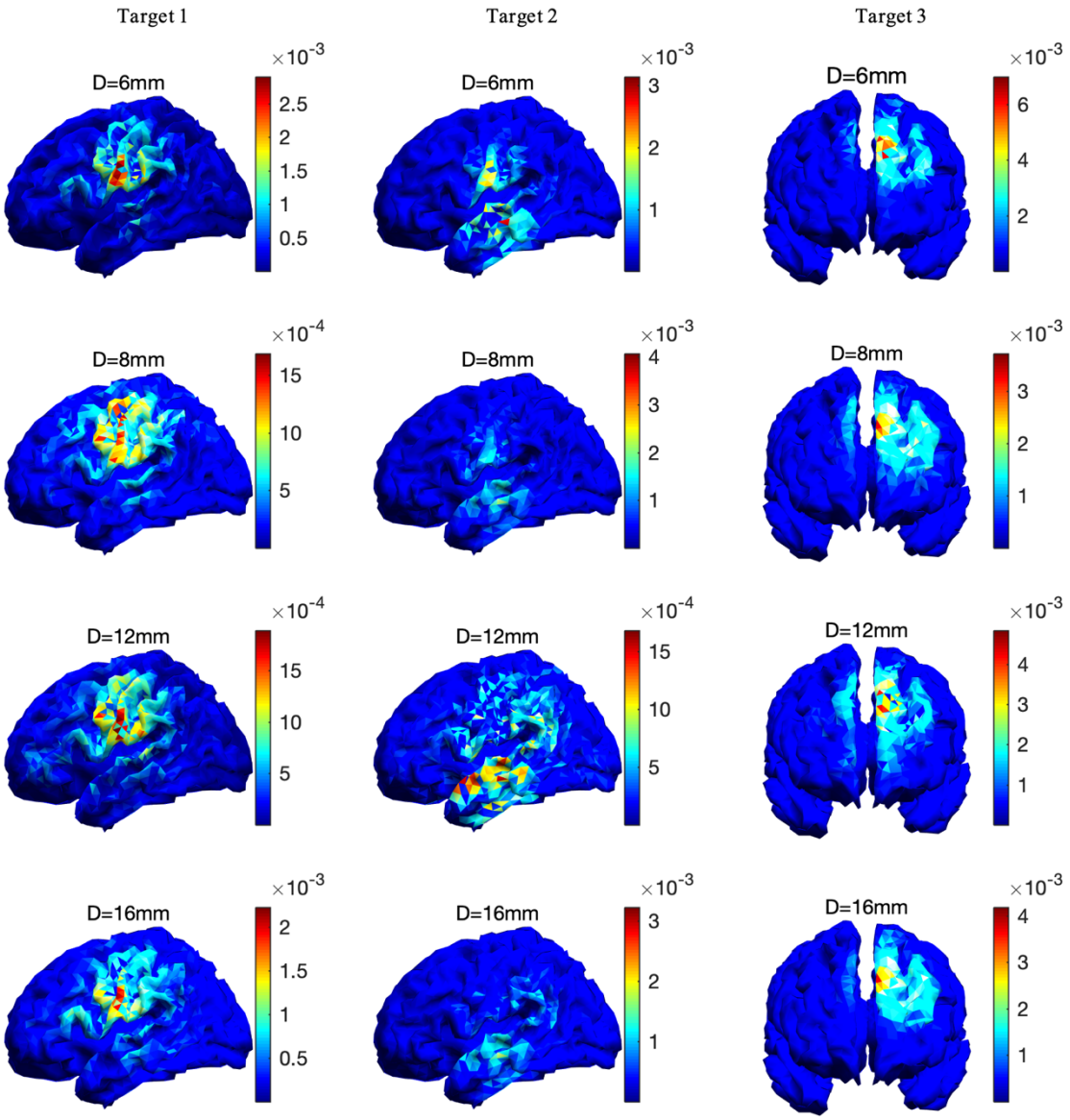

Figure 2.8: Performance comparison at different sizes of electrode.

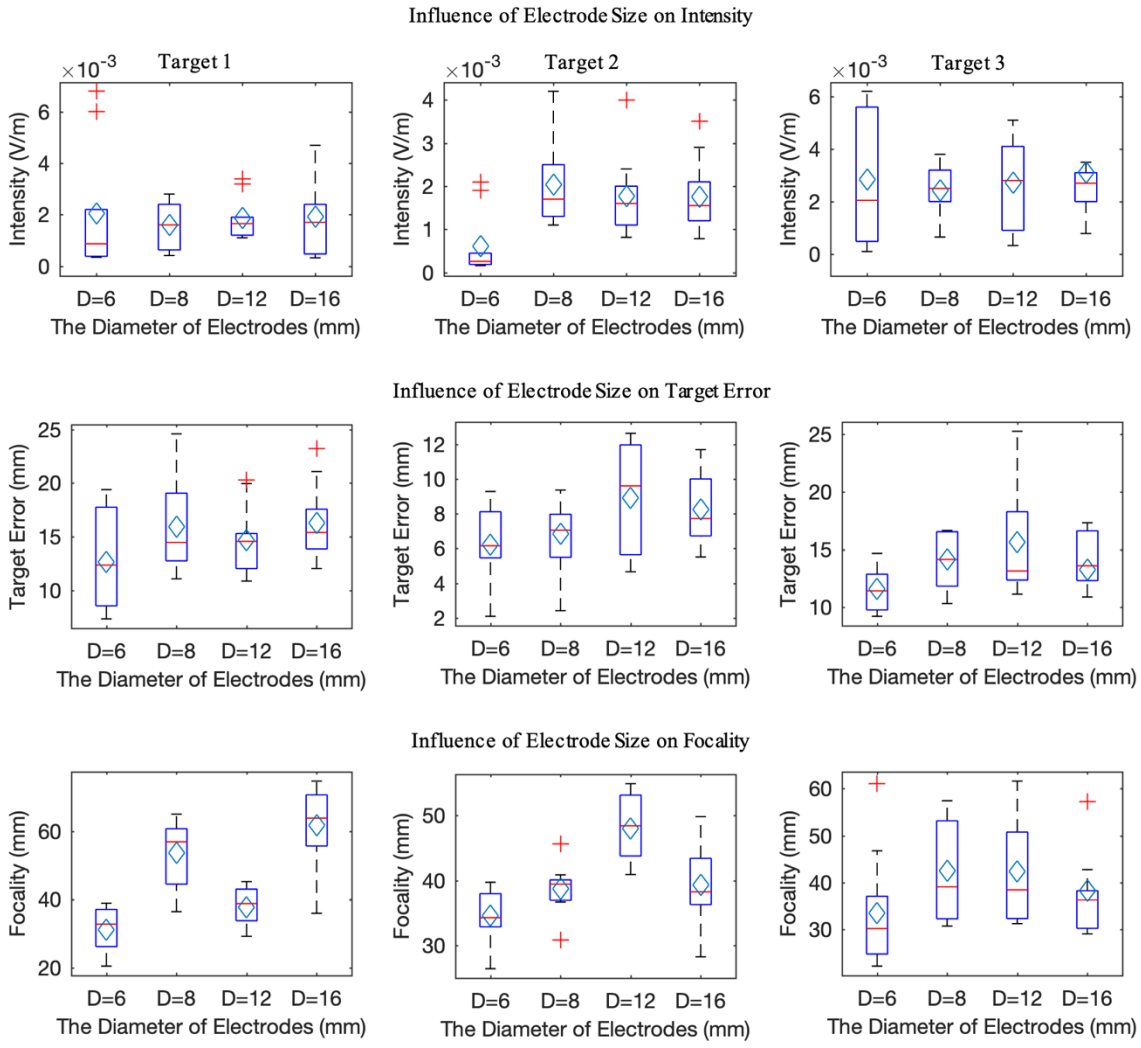

Figure 2.9: Box and whisker plot shows the results at different electrode sizes when stimulating different targets.

The red bar represents the median value, and the diamond in each box indicates the average value. The “whiskers” above and below the box show the values of the highest non-outlier and lowest non-outlier. The red cross sign represents the outliers.

The same comparison has been done to study the influence of electrode size. But from Figure 2.8 and Figure 2.9, there is no clear overall trend for its influence on all three criteria. There are

differences among the four systems, which are inconsistent and vary with the target regions, especially for the 8mm, 12mm, and 16mm systems. According to those results, we could not draw any conclusion that electrode size will have a great influence on tDCS performance.

2.3.3 Influence of Electrode Shape

Figure 2.10: The model of multi-electrode systems with a different shape. From left to right are round electrodes, fractal electrodes, and annulus electrodes.

As for the electrode shape, besides the round electrode, we also designed fractal electrodes [45], [46] and annulus electrodes [47]. The number, surface area and the position of all those electrode models are the same (Figure 2.10).

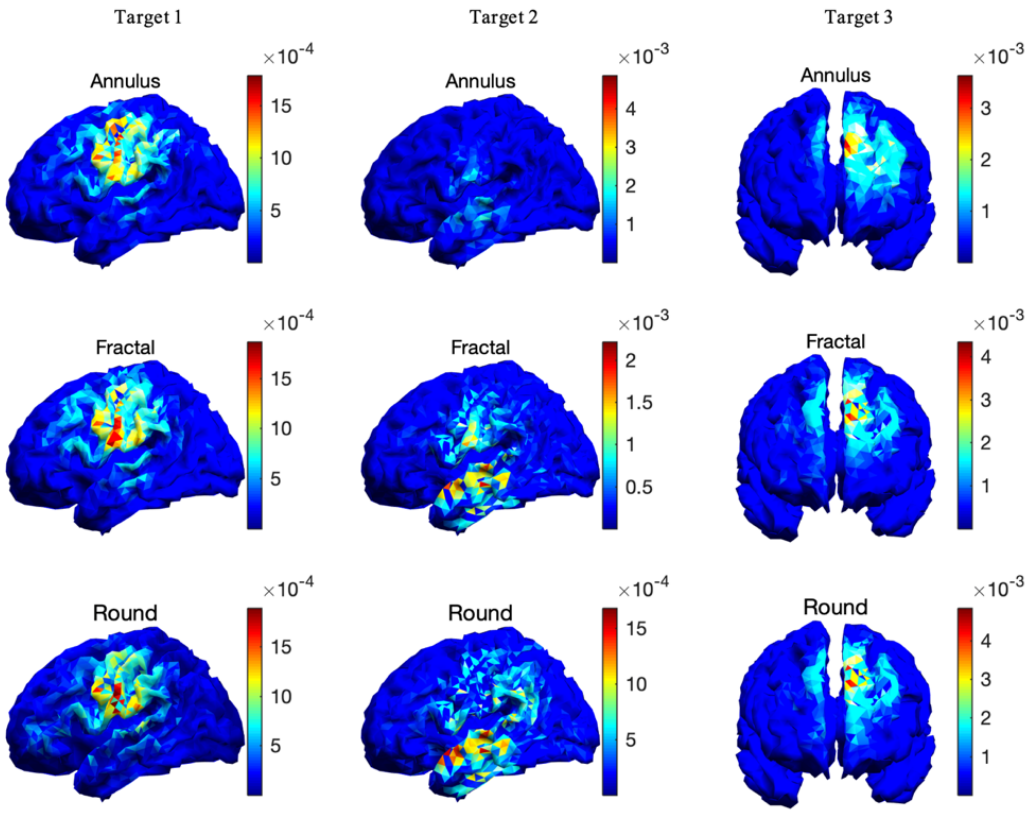

Figure 2.11: Performance comparison at different shapes of electrode.

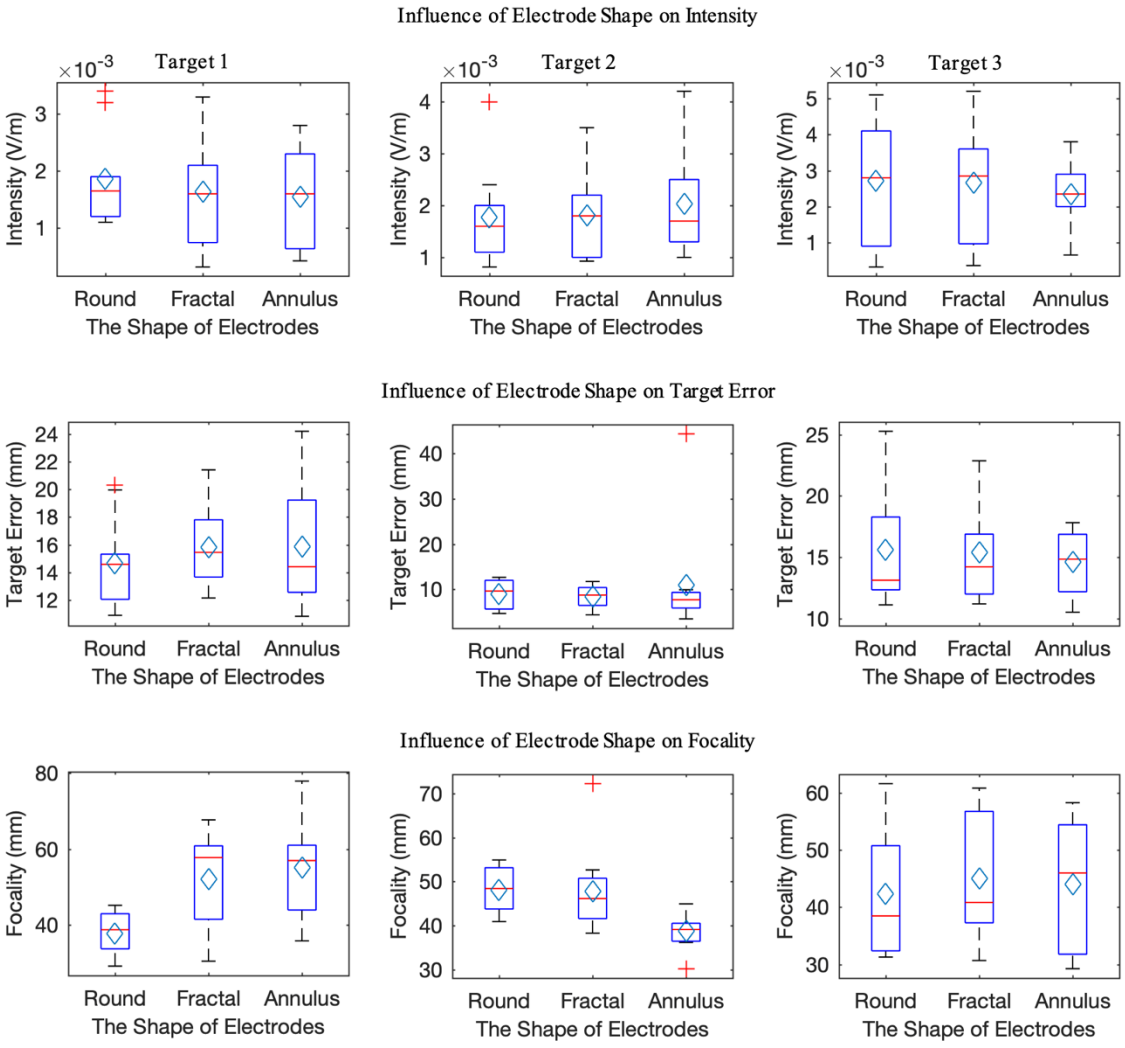

Figure 2.12: Box and whisker plot shows the results at different electrode shapes when stimulating different targets.

The red bar represents the median value, and the diamond in each box indicates the average value. The “whiskers” above and below the box show the values of the highest non-outlier and lowest non-outlier. The red cross sign represents the outliers.

The results in Figure 2.11 and Figure 2.12 show that the electrode shape does not play an important role in improving the tDCS performance, as suggested in the previous study. The

intensity, TE, and focality of the systems with different electrode shapes are almost at the same level regardless of the target situations. Therefore, it's reasonable to conclude that the electrode shape does not make a large difference in tDCS performance in terms of the stimulation intensity and focusing ability.

2.4 Optimization Algorithms in High-Density Electrode System Stimulation

2.4.1 Prior Arts

There are some pieces of literature that aim to further develop the high-density tDCS technique by making use of its high degree of freedom. Various optimization-based methods have been proposed and applied to design a better stimulation pattern and assign current weightings to different electrodes. Different optimization algorithms, incorporating a variety of constraints, can make better use of the high-density electrode system to achieve better stimulation effects. In this section, we will review some popular state-of-the-art optimization algorithms in tDCS.

Constrained Least Squares method (CLS)

The least square is to minimize a second-order error term, which is the most common method for solving the over-determined problem [30], [31]. With the safety constraints introduced in the previous section, it will be referred to as the Constrained Least Squares method (CLS) in this thesis.

$$\boldsymbol{s} = arg\min_{\boldsymbol{s}} \|\boldsymbol{K}\boldsymbol{s} - \boldsymbol{e}_d\|^2$$

The advantage of the CLS is that it can achieve a relatively better focusing ability. On the other hand, the intensity is always too low to activate any target region.

Maximum Intensity (MI)

Maximum Intensity, different from the CLS, maximizes the intensity at the target elements [27], [32]–[34]. If we use $\boldsymbol{C}$ to represent the coefficient matrix of only the target elements, the model of MI can be expressed as follows

$$\boldsymbol{s} = arg\max_{\boldsymbol{s}} \boldsymbol{e}_0{}^T \boldsymbol{C}\boldsymbol{s}$$

$\boldsymbol{C}$ is the submatrix of $\boldsymbol{K}$. $\boldsymbol{e}_0{}^T \boldsymbol{C}\boldsymbol{s}$ is the projection of the electric field at the target node on a vector pointing in the direction of the desired field. The advantage of MI, as the name suggested, is that its intensity at the target region is the maximum value. However, the algorithm achieves high intensity by sacrificing the focusing ability, which will always result in a broadly distributed electric field.

Linearly Constrained Minimum Variance (LCMV)

Linearly constrained minimum variance (LCMV) [30] is similar to the scheme of the beamforming technique; the algorithm enforces a hard linear constraint, that is, the desired e-field distribution at the target along each direction while utilizing the remaining degrees of freedom to minimize the total energy.

$$\boldsymbol{s} = arg\min_{\boldsymbol{s}} \|\boldsymbol{K}\boldsymbol{s}\|^2$$

$$\text{subject to } \boldsymbol{C}\boldsymbol{s} = \boldsymbol{e}_0$$

The advantage of this LCMV method is that it can achieve electric field distribution at the target region as expected. However, there are several shortcomings. The most fatal problem is that it will have no feasible solution if the premise that desired electric field at the target region is not satisfied.

The possibility of having an empty feasible solution set increases when targeting multiple regions or avoiding specific regions. Moreover, there is no guarantee that the resulting electric

field exhibits a maximum at the target, and LCMV may also stimulate an undesired cortex region in order to meet the hard constraint.

Stimulation with Optimal Focality and Intensity (SOFI)

The idea of Stimulation with Optimal Focality and Intensity (SOFI) is combining LCMV and MI to achieve higher intensity as well as better focusing ability [48]. λ is the optimization parameter to balance the trade-off between the intensity and the focality. If w is the ratio between the total number of voxels and the number of target voxels, the objective function of SOFI can be expressed as

$$\boldsymbol{s} = \arg\min_{\boldsymbol{s}} \left(\frac{1}{w} \|\boldsymbol{K}\boldsymbol{s}\|^2 - \lambda \boldsymbol{e}_0{}^T \boldsymbol{C}\boldsymbol{s} \right)$$

The advantage of the SOFI method is that it can achieve better performance both in intensity and focusing ability compared to the other algorithms. The limitation occurs in multiple-target stimulations. SOFI is not able to well balance the performance for each target region, which will be shown later.

2.4.2 Proposed Algorithm: Stimulation with Balanced Focality and Intensity (SBFI)

With the intent to balance the tradeoff between stimulation focality and intensity, Stimulation with Balanced Focality and Intensity (SBFI) combines both in the cost function. The focality is represented by the total energy of the non-target regions $\|\boldsymbol{D}\boldsymbol{s}\|^2$. Here, $\boldsymbol{D}$ is the submatrix of $\boldsymbol{K}$ relating the injected current at non-target regions. The intensity can be expressed by $\boldsymbol{e}_0{}^T \boldsymbol{C}\boldsymbol{s}$. The distribution of the desired electric field intensity at the target is $\boldsymbol{e}_0$ and $\boldsymbol{C}$ is the coefficient matrix of current at the target region(s). Thus, the cost function of SBFI can be further written as:

$$\boldsymbol{s} = arg\min_{\boldsymbol{s}} \left(\frac{n_{tar}}{n_{non}} \|\boldsymbol{D}\boldsymbol{s}\|^2 - \lambda \boldsymbol{e}_0{}^T \boldsymbol{C}\boldsymbol{s} \right)$$

where λ is the optimization parameter to balance the first term of focality and the second term of intensity. Higher λ favors intensity, while smaller λ tends to have better focality. The number of voxels at the target and non-target regions are n_{tar} and n_{non}, respectively.

The proposed objective function, as an improvement of SOFI, increased the intensity by changing the focality term $\|\boldsymbol{Ks}\|^2$ to $\|\boldsymbol{Ds}\|^2$. The cost function of SOFI can be rewritten as:

$$\arg\min_{s}(\|\boldsymbol{Ks}\|^2 - \lambda \boldsymbol{e}_0{}^T \boldsymbol{Cs}) \iff \arg\min_{s}(\|\boldsymbol{Ds}\|^2 + \|\boldsymbol{Cs}\|^2 - \lambda \boldsymbol{e}_0{}^T \boldsymbol{Cs})$$

The optimal solution for the cost function of SOFI is denoted as $\boldsymbol{s}_1$, while the optimal solution of the cost function of SBFI is denoted as $\boldsymbol{s}_2$. Both cost functions share the same feasible solution set T that meets the constraints. We have $\boldsymbol{s}_1, \boldsymbol{s}_2 \in T$. Thus, we have the following two inequalities:

$$\begin{cases} \|\boldsymbol{Ds}_1\|^2 + \|\boldsymbol{Cs}_1\|^2 - \lambda \boldsymbol{e}_0{}^T \boldsymbol{Cs}_1 \le \|\boldsymbol{Ds}_2\|^2 + \|\boldsymbol{Cs}_2\|^2 - \lambda \boldsymbol{e}_0{}^T \boldsymbol{Cs}_2 \\ \|\boldsymbol{Ds}_2\|^2 - \lambda \boldsymbol{e}_0{}^T \boldsymbol{Cs}_2 \le \|\boldsymbol{Ds}_1\|^2 - \lambda \boldsymbol{e}_0{}^T \boldsymbol{Cs}_1 \end{cases}$$

The two inequalities can be reformulated into one as follows:

$$\Rightarrow \|\boldsymbol{Ds}_1\|^2 + \|\boldsymbol{Cs}_1\|^2 - \lambda \boldsymbol{e}_0{}^T \boldsymbol{Cs}_1 \le \|\boldsymbol{Ds}_2\|^2 + \|\boldsymbol{Cs}_2\|^2 - \lambda \boldsymbol{e}_0{}^T \boldsymbol{Cs}_2$$

$$\le \|\boldsymbol{Ds}_1\|^2 + \|\boldsymbol{Cs}_2\|^2 - \lambda \boldsymbol{e}_0{}^T \boldsymbol{Cs}_1$$

$$\Rightarrow \|\boldsymbol{Ds}_1\|^2 + \|\boldsymbol{Cs}_1\|^2 - \lambda \boldsymbol{e}_0{}^T \boldsymbol{Cs}_1 \le \|\boldsymbol{Ds}_1\|^2 + \|\boldsymbol{Cs}_2\|^2 - \lambda \boldsymbol{e}_0{}^T \boldsymbol{Cs}_1$$

$$\Rightarrow \|\boldsymbol{Cs}_1\|^2 \le \|\boldsymbol{Cs}_2\|^2$$

The optimal intensity of the cost function of SOFI is always lower than the optimal intensity of the cost function of SBFI.

Furthermore, the algorithm can be expanded to fulfill the needs of targeting multiple brain regions in a single stimulation session. For example, different erectile dysfunction (ED) symptoms are mapped to different cortical targets, and stimulating a single target may be insufficient to

address multi-dimensional ED pathology [49]–[51]. In addition, network-targeted transcranial direct current stimulation (net-tDCS) is able to change the excitability of the sensorimotor network (SMN) and show the potential to manipulate network connectivity patterns [52]. Similarly, multi-target stimulation is desirable in the potential application of stopping the seizure with the guidance of neural recording techniques [53], [54]. However, stimulation performance at different targets may not be the same because of the complex brain structure. Thus, the optimization parameter λ is further refined by $\boldsymbol{\lambda} = diag(\lambda_1, \lambda_2, \dots, \lambda_{n_{tar}})$ to balance the stimulation effects of different targets.

$$\boldsymbol{s} = arg \min_{\boldsymbol{s}} \left(\frac{n_{tar}}{n_{non}} \|\boldsymbol{Ds}\|^2 - \boldsymbol{e}_0{}^T \boldsymbol{\lambda}^T \boldsymbol{Cs} \right)$$

Since this optimization problem is convex, it can be efficiently solved by software such as CVX.

2.4.3 Experiment Design and Results

2.4.3.1 Simulation Protocol

To test the performance of the proposed algorithms and compare it to the conventional two-electrode system and several available algorithms mentioned, we designed various stimulation cases based on different clinical applications. First, the simplest test is to stimulate a single target containing only one voxel in the motor cortex with the desired intensity of 0.3 V/m; this scenario mimics common clinical use. The second test is to stimulate multiple targets derived from synthetic data. As indicated in Figure 2.13, the stimulation targets contain three brain regions with a maximum electric field of 0.3727 V/m in the left frontal lobe, 0.3522 V/m in the left occipital lobe, and 0.2841 V/m in the left temporal lobe. Our third test measures how each algorithm performs

for real EEG data from a seizure patient [25], [48]. The target regions are identified by EEG source localization [25]. In addition to examining SBFI performance on multiple targets in real seizure data, this study also demonstrates the applicability of our method to EEG-guided brain stimulation. Similar to the synthetic case, there are three target areas in the EEG-guided case. One is in the occipital cortex with a maximum electric field of 0.1107 V/m, while the other two are on the left and right prefrontal lobe with intensities of 0.0702 V/m and 0.0844 V/m, respectively. Due to the infeasibility of a conventional two-electrode system to target multiple areas, it is excluded in the performance comparison study of optimization algorithms for multiple targets.

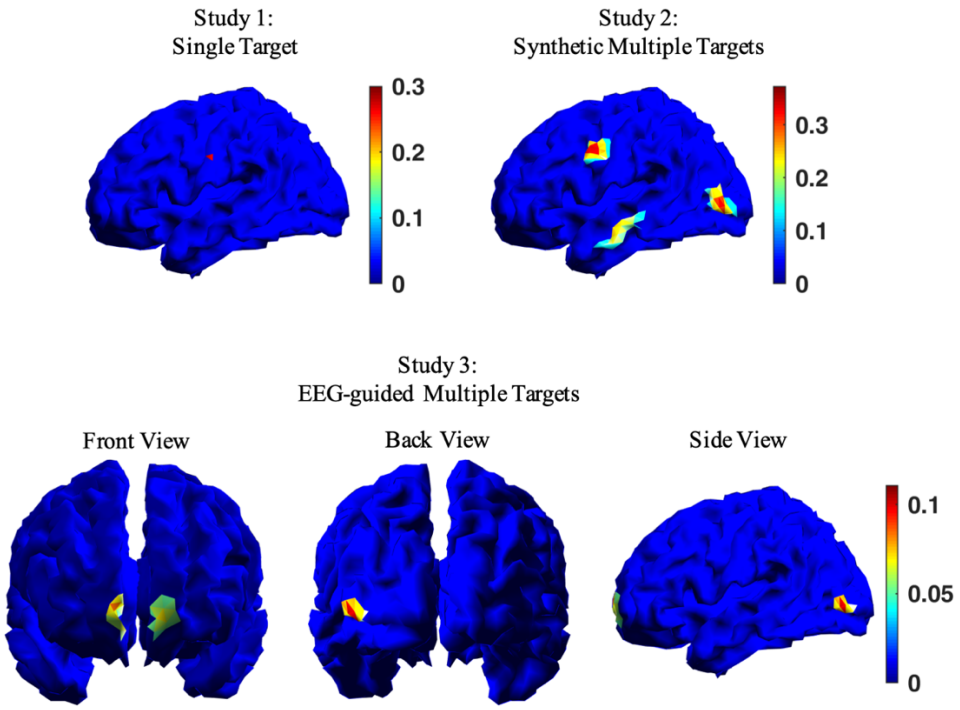

Figure 2.13: Three simulation studies with the different target(s). Study 1: single target. Study 2: Synthetic multiple targets. Study 3: EEG-guided multiple targets.

2.4.3.2 Results

Study with Single Target

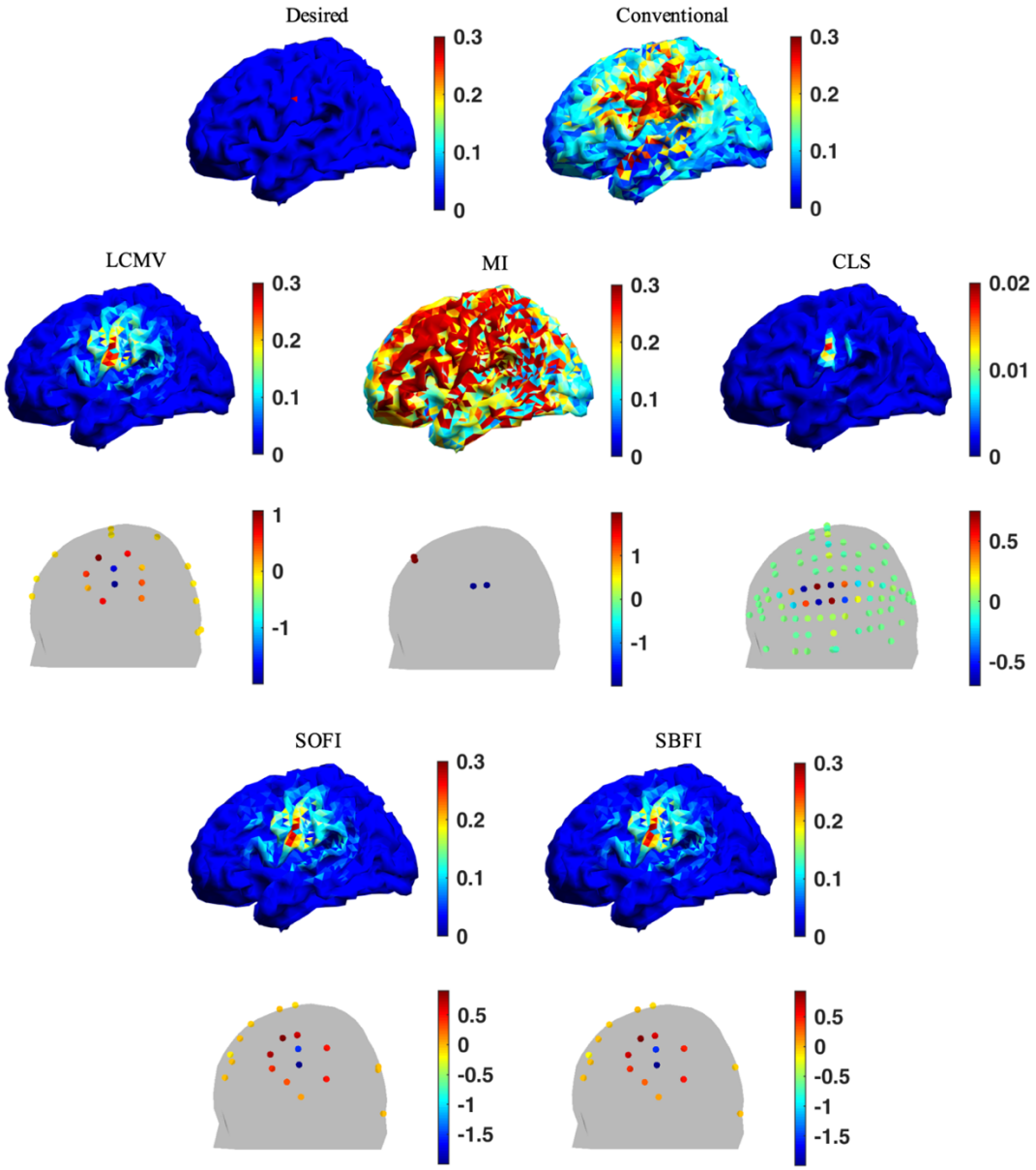

Figure 2.14: Electric field in (V/m) and current pattern in (mA) of different optimization algorithms for the single target protocol.

Table 2.2: Quantitative Evaluations of Single Target Stimulation

Methods	Intensity (V/m)	TE (mm)	Focality (mm)	Electrode Number
Desired	0.3			
Conventional	0.4385	28.3738	63.5043	2
MI	0.7449	29.1206	81.9083	4
CLS	0.0171	6.9016	10.8616	80
LCMV	0.3	9.6710	25.2921	21
SOFI	0.3011	7.3715	22.1196	20
SBFI	0.3018	7.3776	22.1130	19

The advantages of using multiple electrodes over the conventional system with two large pad electrodes can be demonstrated in the results of the electric field distribution with a single target in Figure 2.14, as well as the quantitative evaluations in Table 2.2. The conventional montage produces a maximum electric field of 0.4385 V/m with a focality of 63.5043 mm. The figure clearly indicates this spread-out distribution not only activates the target in the motor cortex but also the entire left hemisphere. A target error of 28.3738 mm shows that the conventional montage does not create an accurate stimulation either. The performance of the MI algorithm is similar to the conventional montage with even higher electric field intensity and worse focality and accuracy, which is as expected. The MI method maximizes the intensity at the target, reaching 0.7449 V/mm with only 4 electrodes. Although its intensity is more than 1.5 times higher than the conventional system, it affects larger brain regions, especially the frontal lobe. The focality and target error are 81.9083 mm and 29.1206 mm, respectively. The CLS method has the opposite results of the MI algorithm and conventional montage. CLS produces an extremely precise and accurate stimulation pattern among all methods with a focality of 10.8616 mm and a target error less than 1 cm. However, the outcome intensity of CLS is around 17 times lower than the desired value. Such a low intensity may not be feasible in real clinical applications. Additionally, this montage requires

80 electrodes, which introduces additional drawbacks compared to the other methods. As for the LCMV, SOFI, and the proposed SBFI method, Figure 2.14 shows that the performance of those three is comparable. All successfully find a balance between MI and CLS algorithms with around 20 electrodes. The desired intensity 0.3 V/m at the target region is achieved, while the focality and target error are within control. The focality of LCMV is 25.2921 mm, and its target error is 9.6710 mm. The proposed SBFI method with $\lambda = 0.0316$ is slightly better at the focality of 22.1130 mm and target error of 7.3776 mm. With the same λ value, SOFI has a slightly lower intensity as predicted. Compared to the conventional montage and MI algorithm, these dramatic improvements in focality and target error indicate that more energy is focused in a smaller region surrounding the target point, which promises more effective and safe stimulation.

Study with Multiple Targets

When stimulating disjointed target regions, the conventional 2-electrode montage is no longer feasible, and using a multiple-electrode system is the only reasonable approach. Thus, the multiple-target studies exclude the conventional system, and comparisons are made only between different optimization methods. It is worth pointing out that LCMV performs reasonably in the single target case, but due to the hard constraint. The LCMV method has no feasible solution set for multiple target cases tested in our study. Therefore, we were not able to compare the performance of LCMV with all the other methods. The failure to have a feasible solution is the key drawback of the LCMV method, and this motivates us to develop the SOFI and SBFI model.

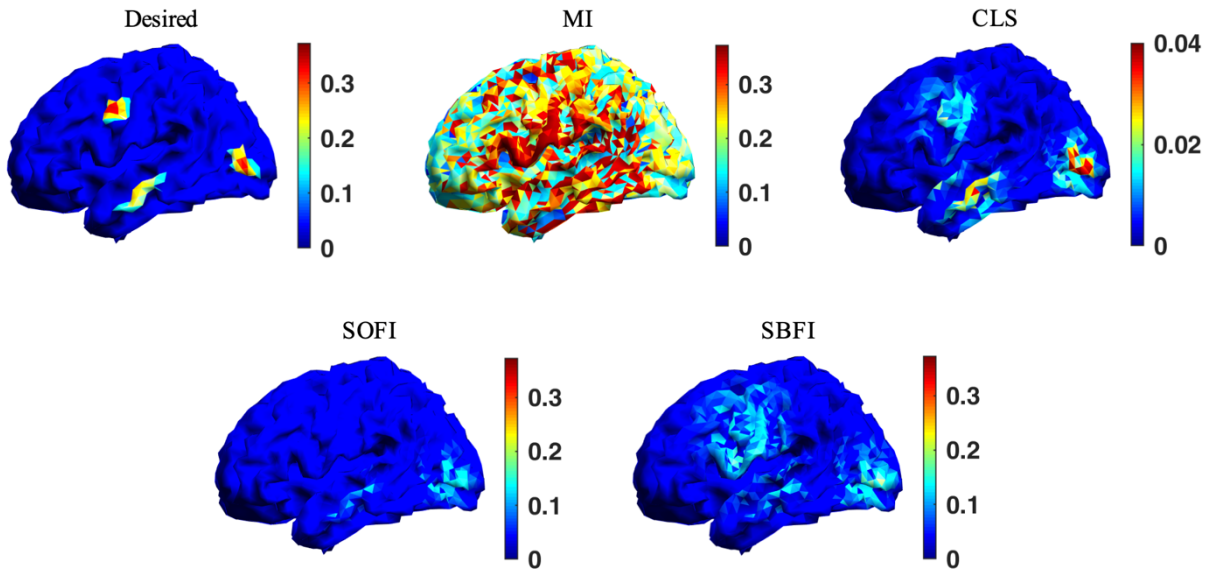

Figure 2.15: Results of different optimization algorithms for the synthetic multiple targets protocol.

Table 2.3: Quantitative Evaluations of Synthetic Multiple Targets Stimulation

Methods	Intensity (V/m)			TE (mm)			Focality (mm)			Electrode Number
Desired	0.3727	0.3522	0.2841							
MI	0.4243	0.3628	0.7083	29.9582	34.1547	21.8123	77.6548	84.3150	63.4031	4
CLS	0.0208	0.0461	0.0370	10.6171	4.4076	4.9572	15.6967	12.5975	17.4074	46
SOFI	0.0394	0.1417	0.0995	14.5507	8.0578	4.2719	31.8758	21.6644	17.2168	26
SBFI	0.1325	0.1906	0.1439	13.0181	9.8556	10.2435	34.9998	24.3398	37.4852	26

The results of synthetic multiple targets are shown in Figure 2.15. Similar to the results of the single target study, CLS can mimic the electric field distribution pattern of the desired result, except the intensities of all three regions are almost an order of magnitude smaller than the desired value. The effectiveness of stimulation is questionable at such low intensities. On the contrary, the MI method produces enough intensities in those three areas but sacrifices the focality. From the distribution figure, it is hard to recognize three discrete areas. The MI method appears to activate

the whole left hemisphere instead. As for the SOFI method with $\lambda = 0.15$, it failed to activate all three areas. In the case of the proposed SBFI method, effective and precise stimulation can be achieved simultaneously with $\boldsymbol{\lambda} = diag(0.5885, 0.247, 0.247)$. The intensity of all three regions is higher than 0.1 V/m, which is enough to induce cortical changes, as shown in the literature [30], [38], [39]. Although the focality values of the three regions are relatively higher than in CLS and SOFI, the energy outside the target region is actually lower than the threshold, which in turn will not be able to activate neurons. Thus, it is an acceptable tradeoff to see this small increase in focality value. Overall, the proposed SBFI method provides a good balance between stimulation intensity, precision, and accuracy. It not only can provide sufficient stimulation intensity as done in the MI method but also is able to minimize target error and focality simultaneously. Besides, it can balance the stimulation effects among all target areas as expected. Quantitative evaluation details are shown in Table 2.3.

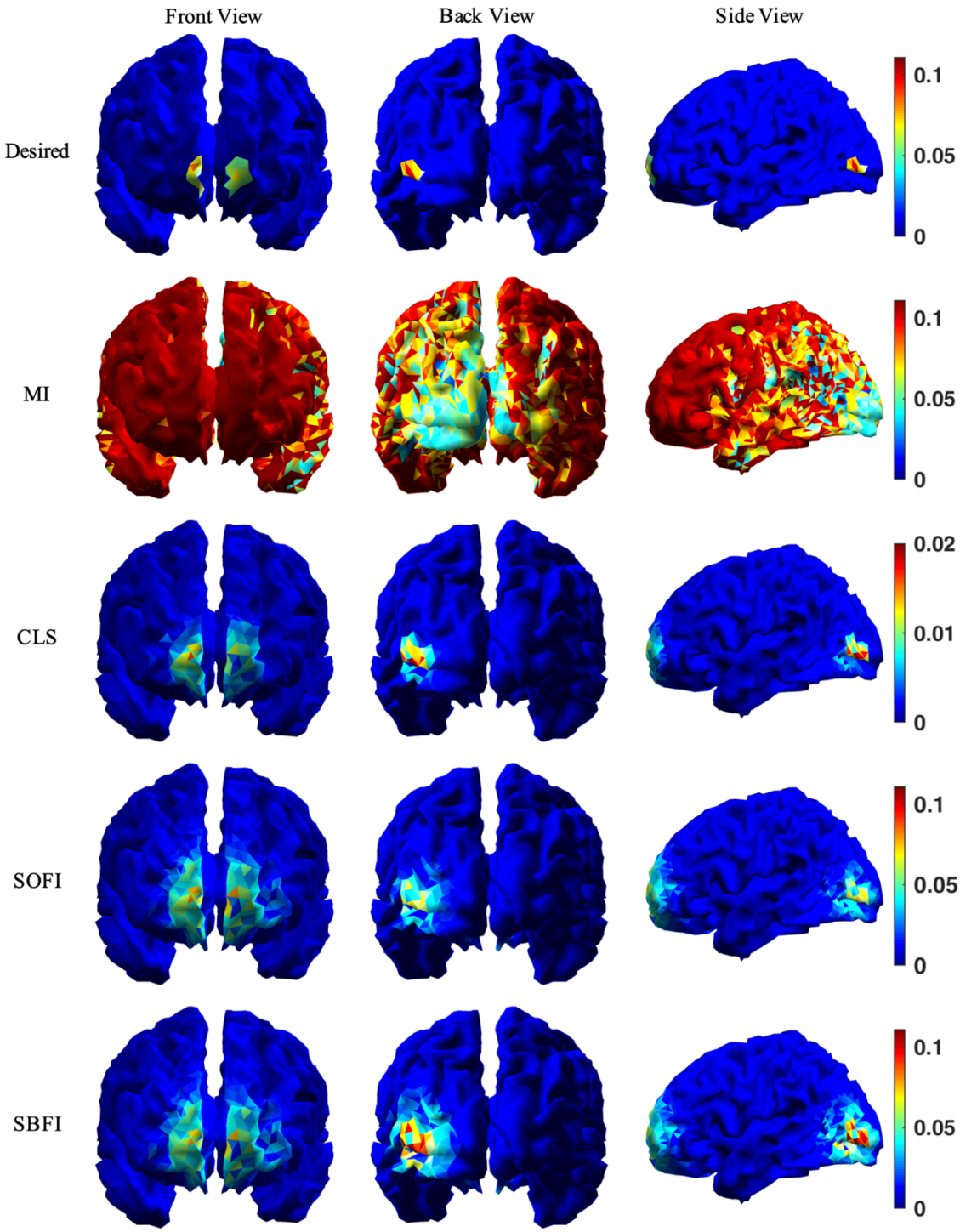

Figure 2.16: Results of different optimization algorithms for the EEG-guided stimulation.

Table 2.4: Quantitative Evaluations of EEG-guided Stimulation

Methods	Intensity (V/m)			TE (mm)			Focality (mm)			Electrode Number
Desired	0.1107	0.0702	0.0844							
MI	0.0707	0.7248	0.4432	77.3818	30.3521	46.1655	86.7308	51.0670	75.1968	4
CLS	0.0205	0.0114	0.0162	5.0799	5.5740	5.5362	8.8909	13.3186	13.1918	72
SOFI	0.0769	0.0785	0.0840	7.7114	11.8733	9.8017	13.9977	27.2759	25.8349	35
SBFI	0.1199	0.0745	0.0792	8.4630	12.1275	9.9984	14.5168	27.1422	20.7317	33

Similar results are obtained for the EEG-guided multiple targets study, as shown in Figure 2.16 and Table 2.4. CLS can preserve the distribution pattern but always fails to achieve enough intensity. MI undoubtedly reaches desired intensity, but the high intensity is at the cost of stimulation focality and accuracy. This EEG-guided case shows that MI even impacts both hemispheres, which may be due to the fact that there are targets on both hemispheres. It is worth pointing out that CLS and MI work towards two extremes: MI favors the intensity of the targets, and CLS produces more focal stimulation. However, SBFI can balance the trade-off between intensity and the focality of all target regions. By choosing the proper optimization parameters $\boldsymbol{\lambda} = diag(0.147, 0.1049, 0.1049)$, SBFI achieves desired intensity at all three target regions with reasonable focality and target error.

2.4.4 Discussion

2.4.4.1 Electrode configuration

The electrode configuration for all studies clearly shows that MI always uses 4 electrodes, where 2 are used for stimulation, and the other 2 are for current return. The two stimulation electrodes deliver most of the current to the targets to increase the intensity. However, with the safety constraint on the total amount of the injected current, no spare electrodes can be used to

neutralize the effects in non-target regions. This is why MI usually has poor focality and target error. In contrast, CLS needs more electrodes than any of the other methods. These electrodes counteract each other to eliminate effects at non-target areas, which explains the good focality and small target error in all CLS results. The large number of electrodes also contributes to low intensity since each electrode can only deliver a small current to meet the safety constraint on the total current. Therefore, the strategy is to keep the number of electrodes neither too large nor too small, which is the unique approach of SBFI. In a sense, some electrodes deliver enough current to ensure the desired intensity, while others are used to decrease the unwanted effects at non-target brain regions.

2.4.4.2 Regularization with Single Lambda and Multi-lambda

As described in the methods section, multiple targets studies can be mitigated by adopting $\boldsymbol{\lambda} = diag(\lambda_1, \lambda_2, \dots, \lambda_{n_{tar}})$ such that balancing each target can be done simultaneously. The motivation to extend one scalar λ to multiple λ_i is that some targets may be in a dominant position and easier to stimulate than others. As shown in the synthetic multiple target case, SOFI using a scalar λ fails to balance the three target regions. The desired intensity of all three target regions is similar, but the result intensity at the motor cortex region is much lower than the other two regions. It appears the system does not favor the targets on the motor cortex region. One possible explanation could be the size of the target region. Intuitively, it is easier for the system to stimulate a large region than a tiny region because fewer electrodes are needed to minimize the intensity at the surrounding non-target region. If the target size is defined as the maximal distance between the target voxels and target mass center, the size of the motor cortex target is 12.9444 mm, which is the smallest among the three, compared to 13.6425 mm on the occipital lobe and 17.7783 mm on the temporal

lobe. Thus, in order to compensate for this unbalanced distribution of size, we have to assign different λ_i for different target regions. Ideally, we could set the optimal λ_i for each voxel. However, for simplicity, currently we have all the voxels in the same region share the same λ.

2.4.4.3 The Choice of Lambda

The results clearly show the proposed SBFI method can achieve a reasonable balance between the intensity and focality by fine-tuning the optimization parameter $\boldsymbol{\lambda}$ under different conditions. This flexibility allows the system to achieve different optimal results tailored to various applications. Decreasing the values of $\boldsymbol{\lambda}$ will increase the weight of the first term $\|\boldsymbol{Ds}\|^2$, which controls focality. The result will always have better focality and lower target error but relatively lower intensity. Increasing the values of $\boldsymbol{\lambda}$ will increase the weight of the second term $\boldsymbol{e}_0{}^T\boldsymbol{CS}$, which controls intensity; the result tends to have higher intensity at the cost of focality and target error. Take the example of multiple synthetic target simulation, when $\boldsymbol{\lambda}$ is chosen to be $\boldsymbol{\lambda}_1 = diag(0.5885, 0.247, 0.247)$, the algorithm favors intensity. When $\boldsymbol{\lambda}$ is chosen to be $\boldsymbol{\lambda}_2 = diag(0.1085, 0.055, 0.055)$, the algorithm favors focality. As expected in Table 2.5 and Figure 2.17, the focality and target error of SBFI ($\boldsymbol{\lambda}_2$) are better than the case of SBFI ($\boldsymbol{\lambda}_1$), but the intensities are lower. Compared to CLS, SBFI achieves the highest intensities at all three target regions while at the same level of the focality and target error. Mathematically, increasing the values of $\boldsymbol{\lambda}$ allows the second term to dominate, and the cost function is closer to the MI method. When $\boldsymbol{\lambda}$ approaches infinity, SBFI is equivalent to the MI algorithm. The first term leads the optimization if $\boldsymbol{\lambda}$ is decreased, as the cost function mainly minimizes the energies of the non-target area.

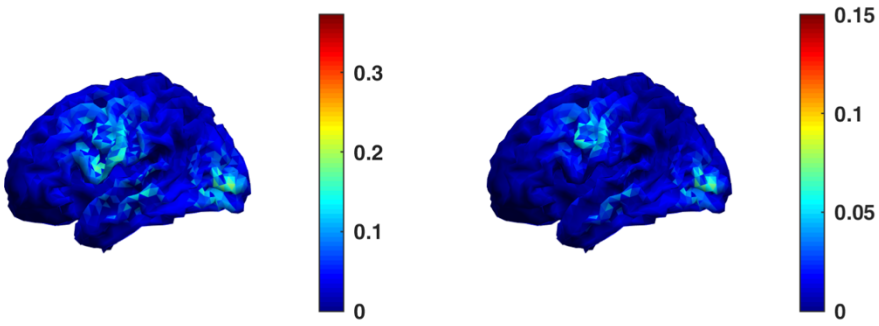

Figure 2.17: The electric field distribution pattern using different optimization parameters in $\boldsymbol{\lambda}$. The comparison is based on the protocol of synthetic multiple targets. Left: the results of $\boldsymbol{\lambda_1}$. Right: the results of $\boldsymbol{\lambda_2}$.

Table 2.5: Quantitative Comparison Between Different λ

lambda	$\boldsymbol{\lambda}_1$	$\boldsymbol{\lambda}_2$
Intensity (V/m)	0.1325	0.0657
	0.1906	0.0704
	0.1439	0.0405
TE (mm)	13.0181	9.7954
	9.8556	7.6622
	10.2435	5.1718
Focality (mm)	34.9998	26.7367
	24.2298	15.4913
	27.4851	16.9662

The selection of $\boldsymbol{\lambda}$ strongly affects the outcome of intensity and focality. From the simulation study, we found that the optimal $\boldsymbol{\lambda}$ varies from case to case, and thus there is no single fixed optimal value for every stimulation problem. Consequently, it is critical to decide the parameter $\boldsymbol{\lambda}$ to balance the intensity and focusing ability. Sophisticated methods for dynamically choosing $\boldsymbol{\lambda}$ must be developed in the case of closed-loop stimulations for evolving sources. Nevertheless,

insights could be obtained by studying the relationship among $\boldsymbol{\lambda}$, the number of target voxels, and the size of target regions. For example, $\boldsymbol{\lambda}$ is higher when stimulating a single target with only one voxel and is much lower when stimulating multiple targets with hundreds of voxels. Thus, it is reasonably predicting that optimal $\boldsymbol{\lambda}$ is inversely proportional to the number of target voxels and then adjusts $\boldsymbol{\lambda}$ accordingly.

2.4.5 Conclusion

In this dissertation, we develop an optimization algorithm, Stimulation with Balanced Focality and Intensity (SBFI), to support high-density tDCS. SBFI can provide a balance between stimulation intensity and focality by adjusting optimization parameter $\boldsymbol{\lambda}$ with a reasonable number of electrodes. Compared to the conventional montage and other popular optimization methods, SBFI not only can obtain sufficient stimulation intensity but also minimize target error and improve stimulation focality simultaneously. In addition, SBFI is better than other algorithms especially in the multiple targets situation that it can balance the stimulation effects among different target areas with ease. A series of simulation experiments present its potential for implementation in different clinical applications, especially stimulation for multiple targets.

2.5 Preparation for Clinical Application

2.5.1 Robustness Study: Effects of Different Tissue Conductivity on Template Model

In the real world, uncertainty in tissue conductivity can result in different electric field distributions from our expected, idealized models ($\sigma_{Scalp} = 0.465\,\mathrm{S/m}$, $\sigma_{Skull} = 0.01\,\mathrm{S/m}$,

$\sigma_{CSF} = 1.65\ \mathrm{S/m}$, and $\sigma_{Cortex} = 0.2\ \mathrm{S/m}$); this greatly affects the robustness of the computational model. The conductivity variations result in a different coefficient matrix $\boldsymbol{K}'_{3n\times m}$; accordingly, with the same current pattern $\boldsymbol{s}_{m\times 1}$, it produces an electric field vector $\boldsymbol{e}'_{3n\times 1} = \boldsymbol{K}'_{3n\times m} \cdot \boldsymbol{s}_{m\times 1}$ that is different from the expected electric field distribution using standard conductivity values. The dissimilarity between $\boldsymbol{e}'_{3n\times 1}$ and the expected distribution $\boldsymbol{e}_{3n\times 1}$ reflects the robustness of the computational model. In this study, we observe how small changes in tissue conductivity can create differences between $\boldsymbol{e}'_{3n\times 1}$ and $\boldsymbol{e}_{3n\times 1}$, thereby analyzing the robustness of our model. Based on the literature [55]–[57], we assumed that the conductivities of the main tissues have uniform distributions with a unit of S/m, i.e., $P_{scalp}(x|\sigma) \sim U(0.2, 0.6)$, $P_{skull}(x|\sigma) \sim U(0.001, 0.04)$, $P_{CSF}(x|\sigma) \sim U(1.20, 2.01)$, and $P_{cortex}(x|\sigma) \sim U(0.05, 0.71)$. An overview of both single and multiple targets with different algorithms is given to demonstrate the general effects of conductivity changes. The detailed influences are revealed by an example of single target stimulation with SBFI in the main text.

2.5.1.1 Evaluation Metrics

Mean Square Error (MSE), the common image measurement, is adopted to evaluate the dissimilarity between $\boldsymbol{e}'_{3n\times 1}$ and $\boldsymbol{e}_{3n\times 1}$. A higher MSE indicates that the electric field distribution is more sensitive to changes in conductivity, and that the computational model is therefore less robust with respect to conductivity uncertainty.

$$MSE = \frac{1}{n}\sum(\boldsymbol{e}'_{3n\times 1} - \boldsymbol{e}_{3n\times 1})^2$$

Then the intensity, TE, and focality of $\boldsymbol{e}'_{3n\times 1}$ are compared with $\boldsymbol{e}_{3n\times 1}$. Finally, the maximum changing rate will be given, defined as the maximum changing value divided by the maximum conductivity changes ($\Delta E/\Delta\sigma$, $\Delta TE/\Delta\sigma$, $\Delta focality/\Delta\sigma$).

2.5.1.2 Results

We investigated our model's robustness to changes in conductivity values: including scalp conductivity, skull conductivity, cerebrospinal fluid (CSF) conductivity, and brain cortex conductivity. Since the electrical properties of these tissues can vary slightly between patients, we use the term "conductivity uncertainty" to describe the small changes made to our model parameters during our robustness study.

The overall impact of conductivity uncertainty

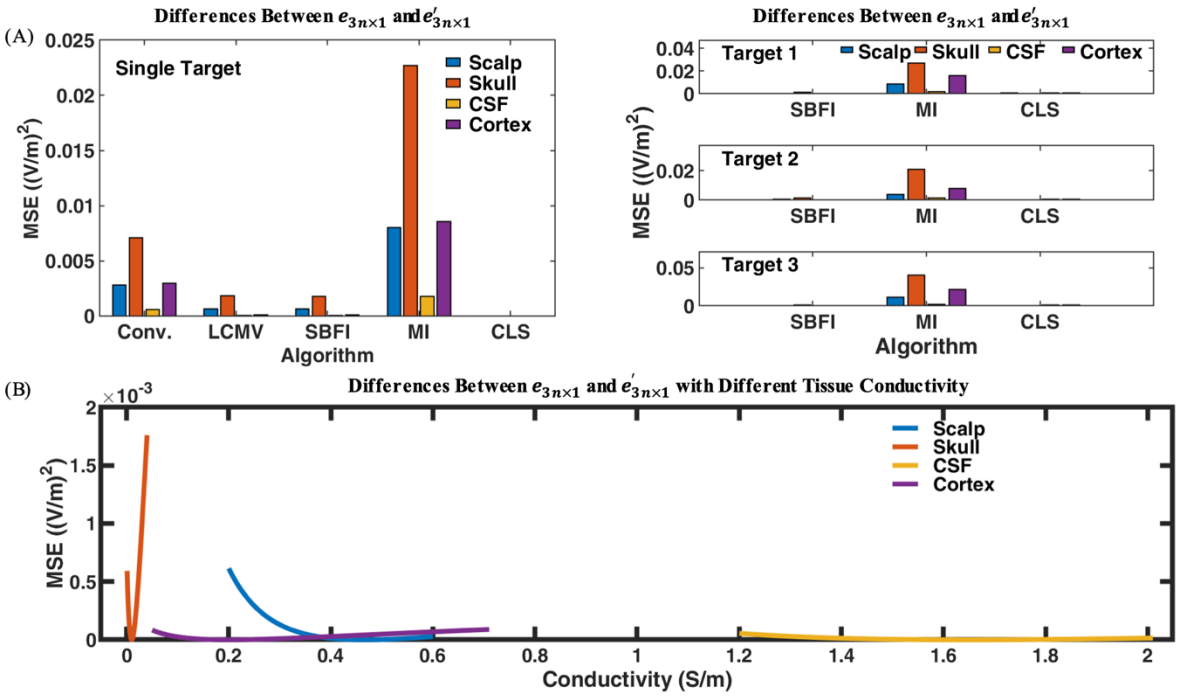

Figure 2.18: The overall impact of conductivity uncertainty.

(A) Mean Square Error (MSE) between expected electric field *e* and electric field *e'* due to uncertainty in tissue conductivity. Left: single target. Right: synthetic multiple targets, from top to bottom are the results for target 1, 2, and 3, respectively. The effects on MSE in general: skull > scalp ≈ cortex > CSF. (B) Example of the MSE changes. When the conductivity of a tissue is

equal to that tissue's original conductivity from the model, the MSE is trivially zero. However, as we shift the tissue's conductivity away from its starting value, the error increases. Larger slopes on the graph above indicate high sensitivity to conductivity changes and, therefore, low robustness to uncertainty. Within the possible conductivity changes, the model is most sensitive to the skull and least sensitive to CSF.

Table 2.6: Dissimilarity Results of the Robustness Test ((V⁄m)^2)

Single Target					
Tissue	Conventional	LCMV	SBFI	MI	CLS
Scalp	0.0028	6.43×10^{-4}	6.14×10^{-4}	0.0080	6.79×10^{-7}
Skull	0.0071	0.0018	0.0018	0.0227	2.80×10^{-6}
CSF	5.71×10^{-4}	6.23×10^{-5}	5.51×10^{-5}	0.0018	4.49×10^{-8}
Cortex	0.0030	9.41×10^{-5}	8.89×10^{-5}	0.0085	3.12×10^{-8}

Figure 2.18 (A) shows the maximum MSE due to conductivity uncertainties for each algorithm. In all cases, the MSE peak appears at the skull layer, and the valley appears at the CSF layer. These accordant peaks and valleys indicate a predominant impact of skull conductivity on model robustness and a minor impact of the CSF on model robustness. The scalp layer and cortex layer have similar heights in-between, which indicates the comparable and moderate influences of the scalp and cortex in general. Figure 2.18 (B) shows an example of MSE analysis in a single-target experiment with our SBFI method. MSE increases as the model's conductivity values deviate from their idealized values, which creates a concave "V" shape for each tissue. Note that the concave "V" shape associated with the skull is much sharper and higher than the others—this shows that the model is more sensitive to small uncertainties or deviations in skull conductivity. The observed trends are consistent with all stimulation scenarios regardless of target types and optimization algorithms.

The impact on intensity by conductivity uncertainty

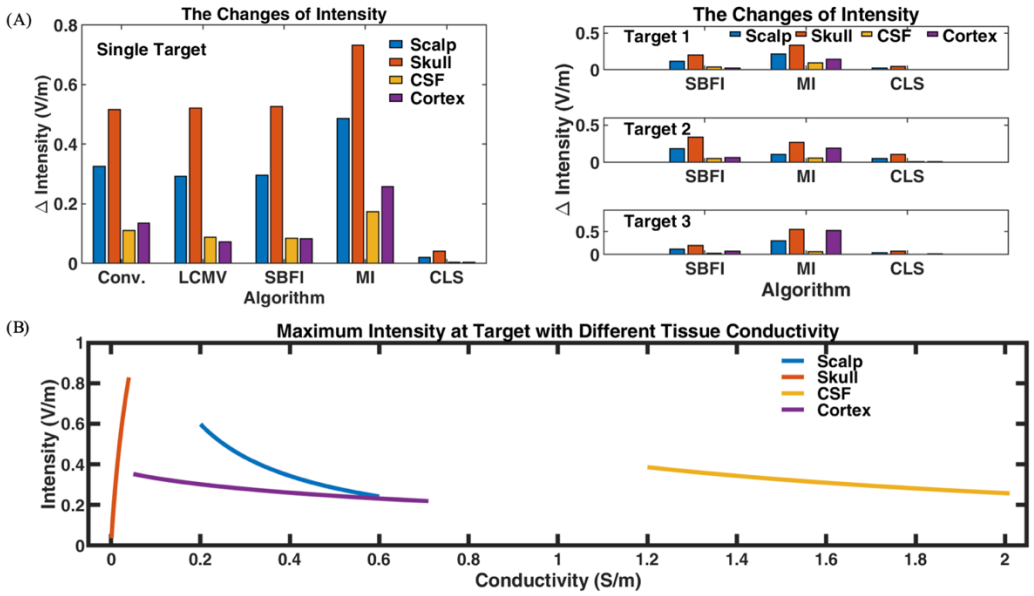

Figure 2.19: The impact on intensity by conductivity uncertainty.

(A) Maximum Intensity deviation from the expected value due to the conductivity uncertainty. Left: single target. Right: synthetic multiple targets, from top to bottom are the results for target 1, 2, and 3, respectively. The effects on intensity in general: skull > scalp > CSF ≈ cortex. (B) Example of the intensity changes. The large intensity spans on the graph above indicate the strong impact of the conductivity changes. Within the possible conductivity changes, skull conductivity increase greatly increases the intensity, while the conductivity increases in scalp/CSF/cortex decrease the intensity.

Table 2.7: Intensity Results of the Robustness Test

Tissue	σ (S/m)	Max Intensity (V/m)	Min Intensity (V/m)	Rate ((V/m)/(S/m))
Scalp	0.2-0.6	0.5978	0.2418	0.8899
Skull	0.001-0.04	0.8283	0.0366	20.2990
CSF	1.20-2.01	0.3860	0.2574	0.1588
Cortex	0.05-0.71	0.3522	0.2192	0.2016

Figure 2.19 and Table 2.7 show that the skull's conductivity uncertainty has the most powerful impact on the electric field intensity. An increase in skull conductivity induced a dramatic intensity growth on the target region. In contrast, the maximum intensity of the target region negatively correlates to the conductivity of the scalp, CSF, and cortex, on which the scalp has moderate effects stronger than the CSF and cortex. One possible explanation for the trends could be related to the conductivity ranges. The conductivity of the scalp/CSF is always much higher than the inner tissue layer skull/cortex. Therefore, the current tends to be shunted through the layers of the scalp/CSF instead of the skull/cortex. If the scalp/CSF conductivity increases, current shunted though the scalp/CSF will increase, weakening the intensity at the cortex. If the skull conductivity increases, less current will be shunted at the scalp/skull boundary. While at the skull/CSF boundary, the skull conductivity is still considerably lower than the CSF. The significant conductivity differences ensure an increase in the net current flowing into the CSF and cortex, resulting in an intensity increase at the cortex.

The impact on TE by conductivity uncertainty

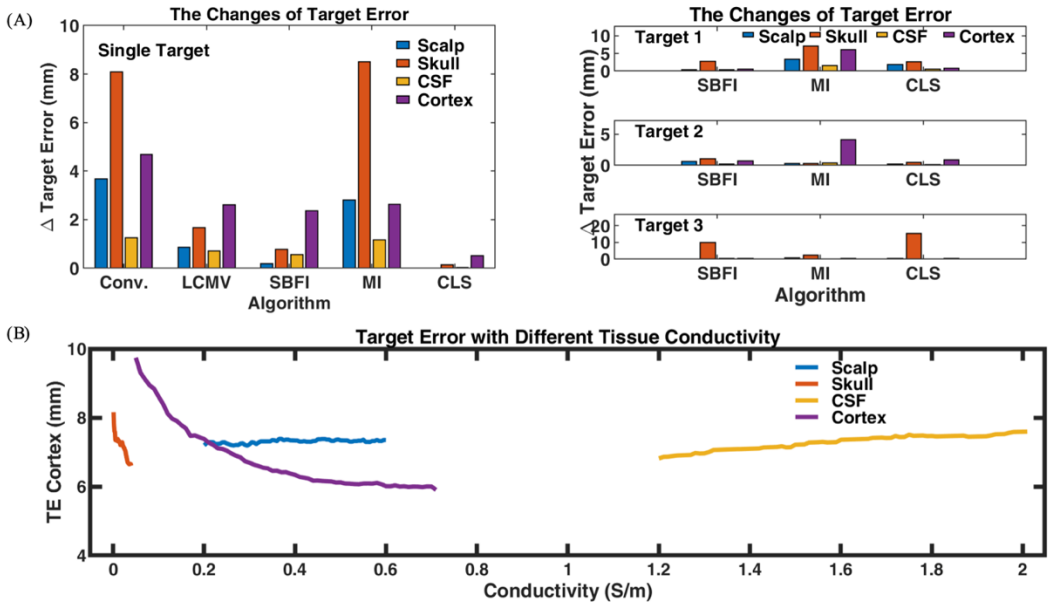

Figure 2.20: The impact on TE by conductivity uncertainty.

(A) Maximum TE deviation from the expected value due to the conductivity uncertainty. Left: single target. Right: synthetic multiple targets, from top to bottom are the results for target 1, 2, and 3, respectively. The effects of TE in general: skull > cortex > scalp > CSF. (B) Example of the TE changes. TE has non-monotonic and divergent changing forms. Overall, TE tends to decrease when the skull/cortex conductivity increases, while scalp/CSF has no clear tendency. TE spans caused by the cortex are the largest, which indicates the strong impact of the cortex.

Table 2.8: Target Error Results of the Robustness Test

Tissue	σ (S/m)	Max TE (mm)	Min TE (mm)	Rate ((mm)/(S/m))
Scalp	0.2-0.6	7.3824	7.1837	0.4969
Skull	0.001-0.04	8.1584	6.6051	39.83
CSF	1.20-2.01	7.5909	6.8166	0.956
Cortex	0.05-0.71	9.743	5.9004	5.8221

Regarding TE in Figure 2.20, the scalp and CSF generally have the least impact capped at 4mm, which have no clear trend of increasing or decreasing for all scenarios. The skull and cortex can alter the TE greatly up to 16mm. Overall, the TE tends to decrease when the skull/cortex conductivity increases. Sometimes, the cortex even induces more TE changes than the skull. However, considering the conductivity change of the skull is 94% smaller than the cortex ($\Delta\sigma_{skull} = 0.039\,\mathrm{S/m}$ and $\Delta\sigma_{cortex} = 0.66\,\mathrm{S/m}$), the skull-induced TE changing rate is actually 6 times higher than the cortex, as shown in Figure 2.20 (B). Thus, it is still reasonable to envision that the skull generally has stronger effects on TE than the cortex does.

The impact on focality by conductivity uncertainty

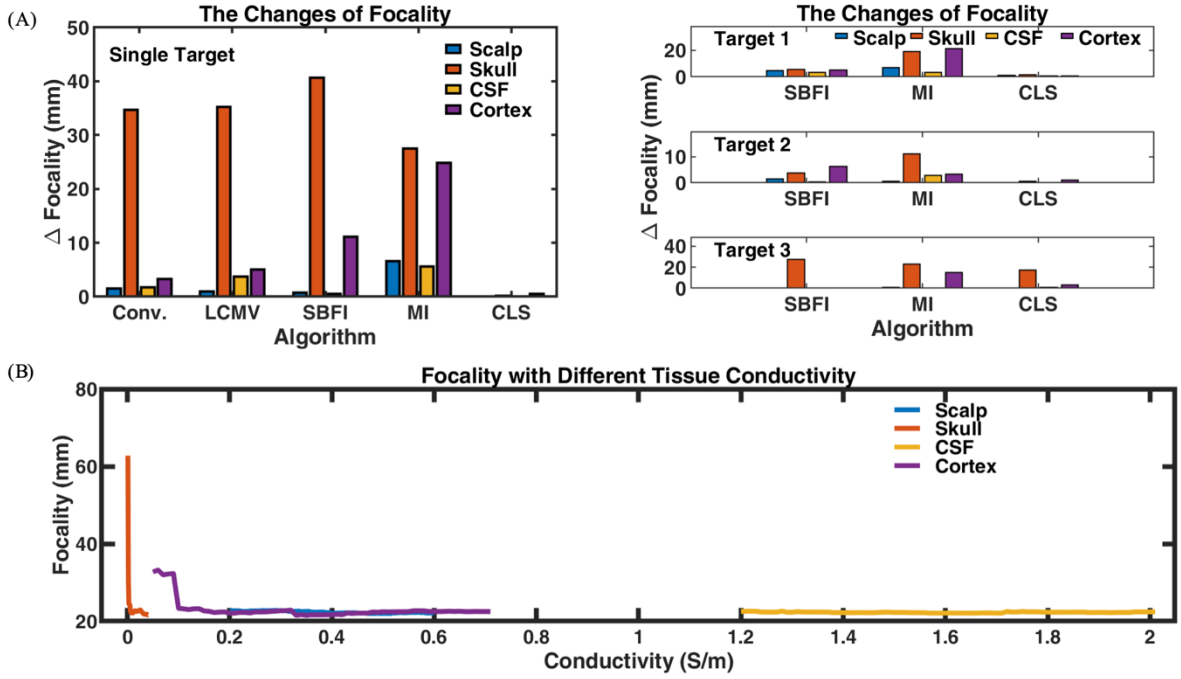

Figure 2.21: The impact on focality by conductivity uncertainty.

(A) Maximum focality deviation from the expected value due to the conductivity uncertainty. Left: single target. Right: synthetic multiple targets, from top to bottom are the results for target 1, 2, and 3, respectively. The effects on focality in general: skull>cortex>CSF≈scalp. (B) Example

of the focality changes. No clear tendency for the focality changes. Most focality changes happen when the skull conductivity is small.

Table 2.9: Focality Results of the Robustness Test

Tissue	σ (S/m)	Max Focality	Min Focality (mm)	Rate ((mm)/(S/m))
Scalp	0.2-0.6	22.808	22.007	2.0023
Skull	0.001-0.04	62.773	21.635	1054.8
CSF	1.20-2.01	22.598	22.102	0.6123
Cortex	0.05-0.71	33.227	21.522	17.736

Similar to the TE test, the scalp and CSF show minor and comparable effects on focality, usually inducing focality changes less than 10mm. Figure 2.21 (A) also reveals the main influence of skull conductivity uncertainty on focality. The skull-induced focality changes can be larger than 40mm, but most of them happen when $\sigma_{skull} \leq 0.005\,\mathrm{S/m}$. When $\sigma_{skull} > 0.005\,\mathrm{S/m}$, the focality change is less than 1.5mm. This also occurs in the other scenarios, but the tuning point is not always the same. The impact of the cortex on focality is more complicated and varies significantly with algorithms and target types. The highest change is ~25mm, but sometimes the influence can be as weak as the scalp/CSF effects.

2.5.1.3 Discussion

Robustness tests here identify the important roles of the tissue conductivities in the optimal stimulation, which is consistent with the existing literature [55], [56]. Through the systematic studies, we investigate the tissue conductivity variation effects for high-density electrode system stimulations with different target types and different algorithms. Overall, scalp and CSF produce slight effects on stimulation target error and focality. Unfortunately, conductivities of the skull and cortex itself greatly influence the electric field distribution over the cortex. These results indicate

the need for individual modeling, especially for the parameter settings of the clinical applications. Another possible solution is to construct general models of specific populations. For example, the tissue conductivities of children, adults, and the aging population vary a lot, while they may be stable within their own group [58]–[60]. Furthermore, conductivity discrepancies resulting from pathologies are also being investigated [61]–[63]. The electrical property changes in disease states may greatly change the electric field distribution and alter the stimulation results. Thus, the specific simulation model for certain disease treatments should be carefully considered. As a result, more experiments should be conducted to investigate the joint influence of different tissue conductivity, various stimulation protocols, electrode characteristics, and more precise human head models, etc.

It is interesting to note the robustness differences among algorithms that the MI method is in general less robust than other optimization algorithms. The conventional montage is slightly better than the MI method with relatively lower bars in Figure 2.18 – Figure 2.21 (A), but the robustness is not as good as LCMV or SBFI. LCMV and SBFI have comparable robustness against tissue conductivity uncertainty. The reason for the more robust behavior could be that both algorithms try to balance both target ($\boldsymbol{e}_0{}^T\boldsymbol{CS}$) and non-target regions ($\|\boldsymbol{Ds}\|^2$) with more electrodes. Therefore, the current distribution in the brain could be relatively more controllable, which leads to more robust results in the face of conductivity uncertainty. The results of LS are the least affected by conductivity changes—far less than the others because of its low intensity over the whole cortex.

2.5.1.4 Conclusion

In the robustness studies, the proposed method SBFI shows good robustness with different tissue conductivity variations. Among the tested algorithms, SBFI has relatively lower deviations from the overall electric field distribution and fewer intensity changes at the target area. The

robustness experiments further suggest the high impact of skull conductivity variations, which requires more consideration in modeling studies and clinical implementation.

2.5.2 GUI tool

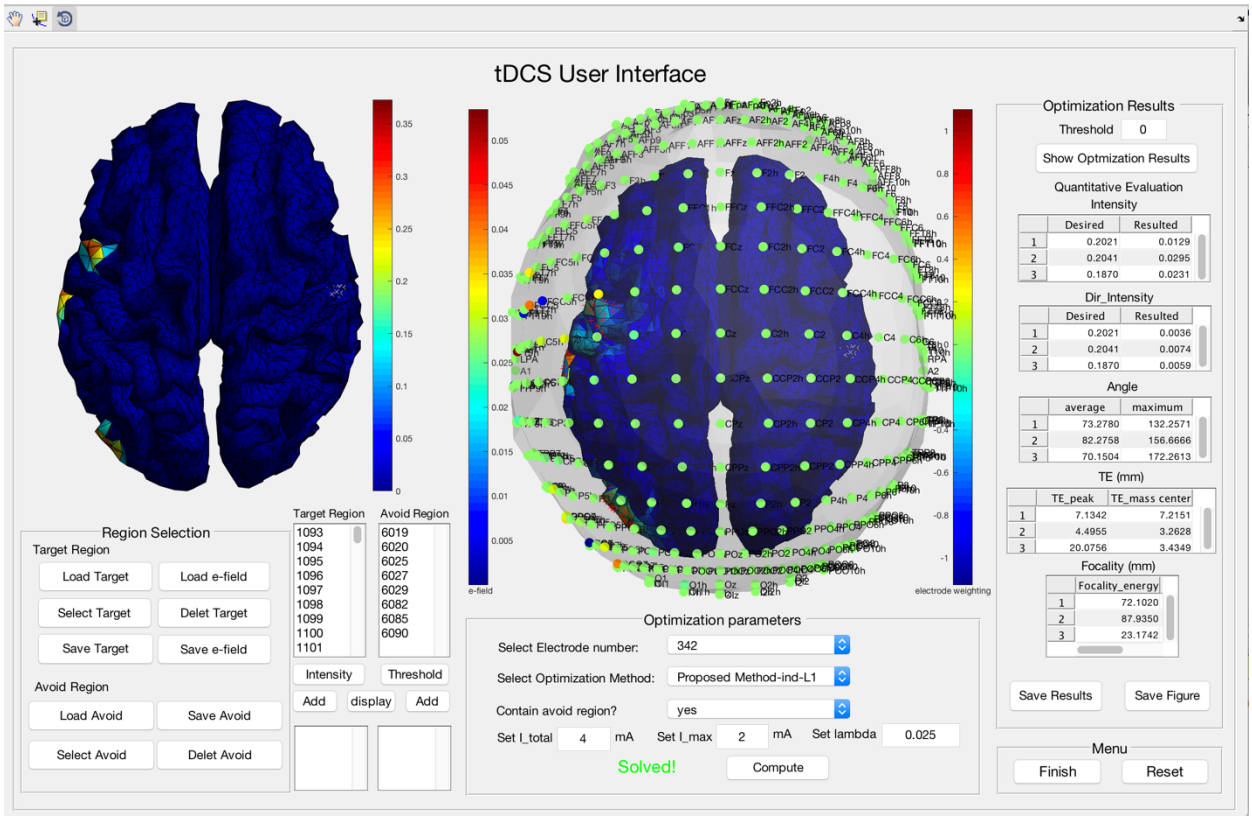

Figure 2.22: tDCS Graphical User Interface.

Simulation studies demonstrate the potential of the proposed computational model in clinical applications. However, there is a need for users, i.e., researchers and clinicians, to understand the coding languages or to type commands in order to run the computational model. Therefore, a MATLAB Graphical User Interface (GUI) is developed to eliminate the difficulties and add interactivity to the computational model (Figure 2.22 and supplementary video 1). It contains three main functional sections that are stimulation setting, optimization setting, and results displaying.

The stimulation setting section on the left allows users to set up the targets and their desired electric field after loading the head model. Users can choose, add, and delete the target or avoid regions directly by clicking the voxels of the head model shown in the left figure displaying zone, the index of which will be indicated in the corresponding text box below that zone. Then, users can specify the desired intensities of the target regions or the maximum intensities of the avoid regions. All the settings can be saved to the work space, together or separately, for backup or future use. Also, this section supports loading the previously saved settings for users' convenience. In the optimization setting section on the middle bottom, users have the flexibility in choosing or specifying: 1) the electrode system having different number of electrodes, 2) the optimization methods and their parameters, and 3) the safety constraints. With the chosen method, it starts running by clicking the *Compute* button. It will flash with *Solved* in green if the problem has a feasible solution and *No Solution* in red otherwise. If it's solved, the simulation results will be shown after clicking *Show Optimization Results* button on the upper right. The electric distribution over the cortex and its corresponding electrode configuration will be presented in combination in the middle figure displaying zone. All the quantitative evaluations will be given on the right. Both the figure results and matric results can be saved as needed in the results displaying section. The main menu on the lower right of the screen is designed to have a *Finish* and a *Reset* shortcut button to close the GUI or reset the settings.

2.6 Optimization for Transcutaneous Spinal Cord Stimulation (tSCS) through a Multi-Electrode Array

2.6.1 Introduction

Transcutaneous spinal cord stimulation (tSCS), similar to epidural spinal cord stimulation, is a potential neuromodulation therapy that has multiple applications, such as restoration of motor function in patients with spinal cord injury (SCI) [64]–[66], treatment of chronic refractory pain [67]–[70] and spasticity modification [71], [72]. Instead of implanting electrodes into the body, conventional tSCS uses one or two large electrodes placed over the back and one or two return electrodes on the abdomen to perform electrical neuromodulation. This conventional configuration allows currents injected from the electrode on the back to flow through the body and be collected by the return electrode. Nonetheless, one critical issue of this configuration is the inability of better delivering the stimulation current to the target without activating undesired regions.

On the other hand, instead of using the conventional configuration, tSCS through a multiple electrode array has also been investigated. A 3×8 electrode pad placed over T10-L2 vertebrae was tested [73]. The results show that the electrode array could produce a more focal electric field distribution along the longitudinal direction when choosing a separate electrode strip (a raw of three electrodes) for stimulation and further enable the segmental selective stimulation of posterior root-muscle reflexes. However, the desired efficacy diminishes when three separate electrodes are connected together through a continuous hydrogel layer. Though the above study demonstrates the potential of using multiple electrodes to achieve focal and selective stimulation, a better mechanism to utilize the multi-electrode array is still missing.

Through our prior study [48], [74], careful selection of the current weighting for each stimulation electrode can significantly improve the spatial resolution of the stimulation via a multi-electrode array. The same principle can be applied to the non-invasive tSCS while appropriate electrode-body modeling and optimization algorithms to determine the stimulation strategy are needed. The idea stimulation result is to correctly stimulate the target region, maximize the intensity at the target, and minimize the energy at the non-target area, which corresponds to the stimulation accuracy, intensity, and selectivity. State-of-the-art optimization algorithms for electrical stimulation can achieve some of the above features at the cost of stimulation accuracy. Furthermore, there is a lack of accurate human body modeling, allowing the quantitative investigation of various algorithms for tSCS.

In this thesis, we developed a 3D real spinal cord model and extended the proposed optimization algorithm SBFI to the tSCS technique.

2.6.2 Methods

2.6.2.1 Realistic 3D Spinal Cord Model

The computational model is derived from cryosection images of The Visible Human Project (VHP) [75], which is shown in Figure 2.23. The first step is tissue segmentation and is done by Invesalius (Renato Archer Information Technology Center., Campinas, São Paulo, Brazil). The torso was segmented into twelve layers, including three layers of skin (SC, SG, and dermis), fat, epidural fat, abdomen, muscle, vertebrae, intervertebral disc, CSF, gray matter, and white matter. Meshmixer (Autodesk, San Rafael, CA, USA) and SolidWorks (Dassault Systèmes SOLIDWORKS Corp., Waltham, Massachusetts, USA) are used for further boundary repair, model dimension transformation and file format conversion. The procedure of realistic spinal cord

model construction can be applied to either MRI or CT data. The reason we used the cryosection image is its higher resolution and smaller spacing interval compared to the MRI and CT data of the VHP data, which makes the model more precise and accurate for the rest of the work.

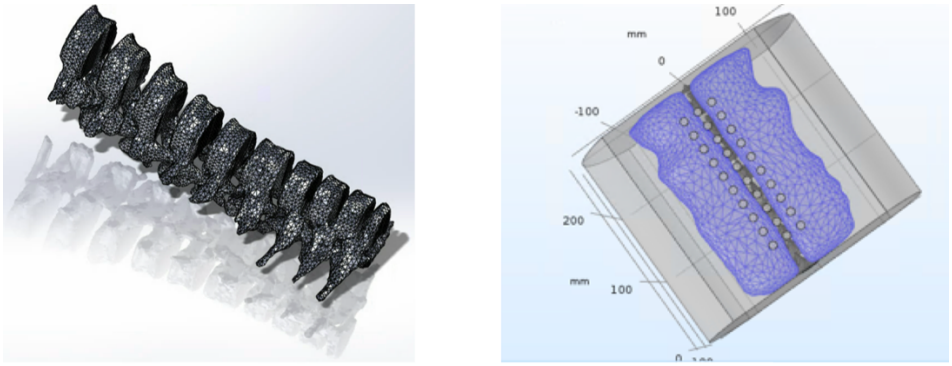

(A) (B)

Figure 2.23: 3D model. (A) Vertebrae model derived from The Visible Human Project. (B) Position of the electrode array.

Besides the spinal cord model, we also need to construct an electrode model for both single electrode and array electrodes. The single electrode has a size of 3cm in diameter, which is the common size for the commercialized device. The single electrode was placed on the back over the T11 and T12 spinous processes. For the electrode array, we built a 3×10 array with a 20mm pitch for both line and column spacing, and the diameter of the electrode is 1cm. The array electrodes were placed on the back, covering T8 to L3, and the center column is lying above the midline of the spinal cord. The return electrodes of both single and array systems share the same position on the abdomen. The relative position of the electrode and vertebrae is shown in Figure 2.23 (B).

2.6.2.2 Mathematical Model

Similar to the tDCS problem, the mathematical model of the tSCS can be constructed by using the finite element method (FEM). In the tSCS study, the voltage Hessian distribution of the spinal

cord, as the nerve activating function defined by the well-known Cable Equation, is of interest [76]. The model is discretized into small voxels, and the number of voxels that belongs to the white matter (nerves) is denoted by n. In addition, we denote injected currents of m electrodes by $S_{m\times 1}$. Following the superposition principle, the voltage Hessian feature of the white matter has a linear relationship with the injected current. If we use vector $H_{3n\times 1}$ to represent the voltage Hessian feature of the white matter, the relationship can be expressed by the equation:

$$H_{3n\times 1} = K_{3n\times m} \cdot S_{m\times 1}$$

Being similar to the tDCS problem, $K_{3n\times m}$ is the lead field matrix and can be calculated by solving Maxwell's equations.

For safety purposes, the stimulation intensity is reported to be free from pain and tolerable when it is no larger than 200mA with a carrier frequency of 10kHz [77]. Besides, following the conservation law of currents, the net currents through the body should be zero. Therefore, the mathematical model is revised to be a constrained optimization. The constraints are as follows in which $I_{max} = 80\text{mA}$, and $I_{total} = 160\text{mA}$.

$$\boldsymbol{s} = \{\boldsymbol{s} \in \mathbb{R}^m : \|\boldsymbol{s}\|_\infty \leq I_{max}, \|\boldsymbol{s}\|_1 + |\boldsymbol{s}^T \mathbf{1}| \leq 2I_{total}\}$$

where $\mathbf{1} = (1, \dots, 1)^T \in \mathbb{R}^m$.

As a result, the cost function of SBFI can be modified as follows:

$$\boldsymbol{s} = arg\min_{\boldsymbol{s}} \left(\frac{n_{tar}}{n_{non}} \|\boldsymbol{D}\boldsymbol{s}\|^2 - \boldsymbol{H}_0{}^T \boldsymbol{\lambda}^T \boldsymbol{C}\boldsymbol{s} \right)$$

where $\boldsymbol{D}$ is the submatrix of $\boldsymbol{K}$ that describes the linear connections between injected currents and the Hessian feature at the non-target area. $\boldsymbol{C}$ is the submatrix of $\boldsymbol{K}$ delivering the linear relationship between currents and target region(s). $\boldsymbol{H}_0$ is the Hessian feature of the target(s).

2.6.6.3 Simulation Protocol

Researches show that lumbosacral spinal cord stimulation with a single electrode placed over T11 and T12 spinous processes can excite muscles innervated by L2-S2, including rectus femoris (RF), biceps femoris (BF), tibialis anterior (TA), and triceps surae muscle group (TS) [78]. Thus, we designed to simulate the lumbosacral spinal cord stimulation protocol and compare the results of a single electrode and electrode array. The target tissue that we aim to stimulate is white matter (nerves) since the dorsal root is the main target region in many clinical applications such as pain control and lumbosacral spinal network modulation. The desired voltage Hessian intensity is the same as the Hessian intensity of the target produced by the conventional single electrode, which is $1500\ \mathrm{V/m^2}$. Different optimization algorithms are tested and compared based on the same electrode array.

2.6.6.4 Quantitative Evaluation of the Stimulation Performance

Similarly, three evaluation metrics of the activated area intend to judge the stimulation efficacy, precision, and accuracy quantitatively. The first criterion is the intensity of the hessian features at the target region with a unit of volt per meter squared; higher intensity is believed to make the treatments more effective. The second measurement is the target error (TE) of the stimulation, which is the distance between the mass center of the target region and the mass center of the activated region. The unit of TE is millimeter. TE describes the stimulation accuracy; small TE indicates that the area activated by the stimulation is close to the target region and, consequently, could achieve the correct function as expected. The focality evaluation is slightly different from the tDCS study considering the anatomy differences. The spinal cord is not fully covered by the vertebrae. The intervertebral discs and intervertebral foramens, with high conductivities, will shunt

the current and cause high hessian features at the nearby spinal cord segments. Therefore, we evaluate the area (cubic millimeter) that has been activated at other spinal cord segments. The threshold is set to be equal to the desired hessian intensity.

2.6.3 Results

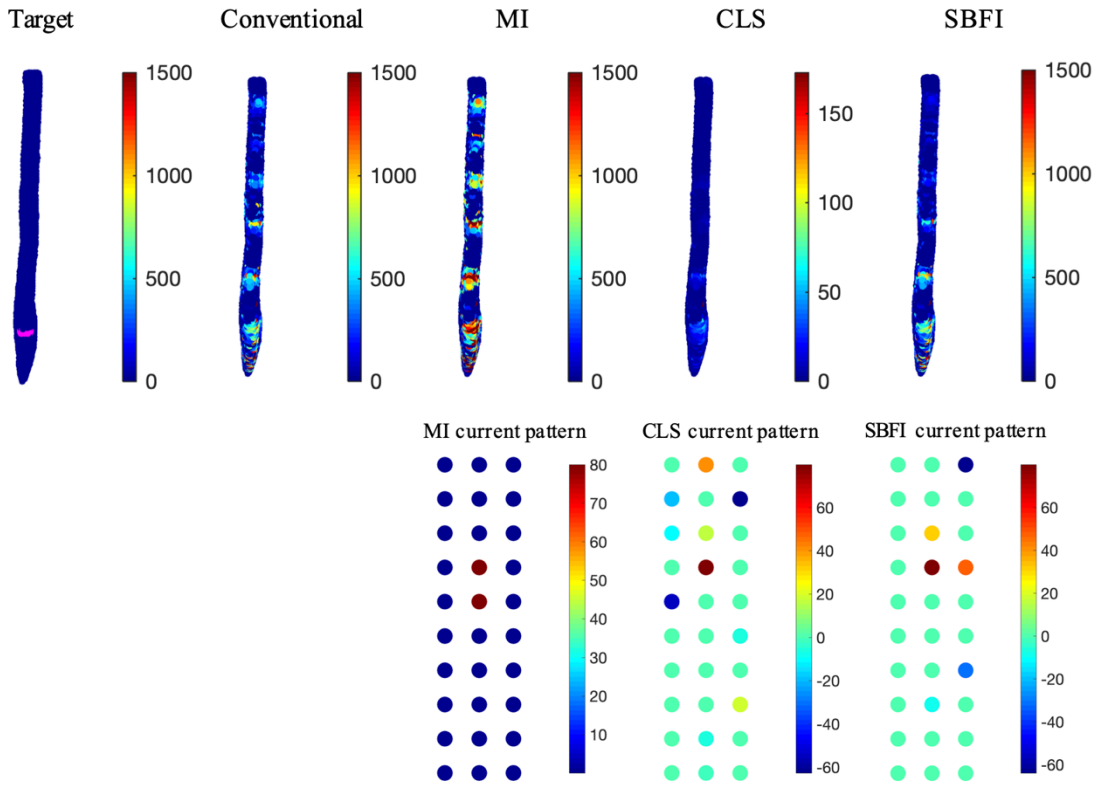

Figure 2.24: Results of conventional tSCS and different optimization-based multi-electrode tSCS.

Table 2.10: Quantitative Evaluations of tSCS

Methods	Hessian (V/m^2)	TE (mm)	The area (mm^3) that has been activated in other segments					
			Non-target 1	Non-target 2	Non-target 3	Non-target 4	Non-target 5	Non-target 6
Desired	1500							

Conventional	1510.5	2.33	0.11	0	0.06	0.23	0.51	2.55
MI	3010.5	2.17	2.04	0.68	2.04	4.41	3.00	12.9
CLS	69.1	2.82	0	0	0	0	0	0
SBFI	1500.9	2.11	0	0	0	0	0.06	2.15

The results of the computational experiments are in Figure 2.24 and Table 2.10. As mentioned in the previous section, the conventional montage produces a voltage Hessian feature of $1500\ \mathrm{V/m^2}$ at the target region. The mass center of the activated area has a shift of 2.33mm from the desired target region. The Hessian distribution in Figure 2.24 indicates that conventional montage not only activates the desired target segment but also creates the same or even higher hessian intensity at the other six non-target segments. Those non-target segments are located in the thoracic level and conus medullaris. The approximated volume of each segment is shown in Figure 2.24. For the electrode array with different optimization algorithms, the stimulation performances vary a lot. The CLS method is the only method that does not activate any non-target area. However, its Hessian intensity of the target region is also too low to achieve effective stimulation, and the target error is the largest. On the contrary, the MI method produces the highest Hessian intensity in the target region, which is almost two times higher than the conventional montage. In addition, its target error is also smaller compared to the conventional stimulation. The deficiency of the MI method is also apparent that it activates six regions besides the target. Similar to the conventional montage, we can see from Figure 2.24 that all those regions are stimulated with high hessian values. If comparing the area of which hessian intensities are higher than $1500\ \mathrm{V/m^2}$, we could find that the MI method activates an average volume of $4.18mm^3$ been activated in non-target segments. The largest activated non-target segment is conus medullaris (non-target segment 6), the volume of which is about $13mm^3$. Neither CLS nor MI produces better

stimulation performance. The achievement of high intensity is always accompanied by activating too many non-target segments, and reducing the hessian intensities of the target region seems to be the only way that can stimulate fewer non-target segments. According to the quantitative results, the proposed method is the only method that can balance the trade-off well. When parameter λ is 0.0047, the hessian intensity at the target reaches the desired value, which is about the same as the conventional montage. TE of the proposed method is the smallest among all the methods. And compared to the conventional stimulation, smaller areas of the non-target segments have been influenced. The results indicate that the proposed method SBFI maintains the stimulation intensity and affects fewer non-target segments, which achieves a selectively spinal cord stimulation.

2.6.4 Discussion and Conclusion

The computational simulation experiments demonstrate the limitations of the conventional tSCS and the feasibility of using a multi-electrode array for selectively spinal cord stimulation. The comparisons among all the methods also emphasize the importance of choosing a proper optimization algorithm. The performances of these algorithms vary a lot, and some may be even worse than the conventional montage. The failure of the CLS method may be due to the ratio between the number of target voxels and the number of non-target voxels. The ratio is too small, which makes the non-target voxels in a dominant position. The algorithm minimizes the overall error. Thus, it reduces the overall intensity to favor the non-target region. The poor performance of the MI is because it only maximizes the Hessian intensity but has no constraints on the non-target area. The proposed SBFI is the only method that can balance the trade-off well.

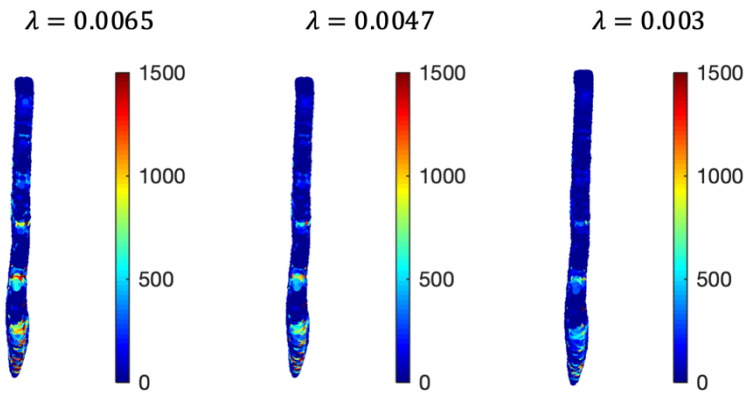

Figure 2.25: Results and comparison of different parameter λ.

As discussed in the tDCS optimization problem, the proposed method uses λ to balance the targeted and non-targeted regions. Scalar λ is used in the study since the single target is tested. Figure 2.25 shows the same effects of λ on the stimulation performance that increasing λ will increase the weight on the target region; producing higher intensity is the first priority. When $\lambda = 0.0065$, the intensity in the target region is almost $2000\ \mathrm{V/m^2}$, but it affects more non-target segments. If λ is increased towards infinity, it becomes the MI method. On the other hand, decreasing λ will increase the weight on the non-target region. It will lower the intensity to avoid activating too many non-target regions. When $\lambda = 0.003$, the intensity is slightly higher than $1000\ \mathrm{V/m^2}$, and little effect in the non-target region. Compared to the $\lambda = 0.0047$, 0.0065 and 0.003 do not perfectly work for the expectation in the scenario ($1500\ \mathrm{V/m^2}$). The choice of λ ($\boldsymbol{\lambda}$) becomes a critical issue for future development.

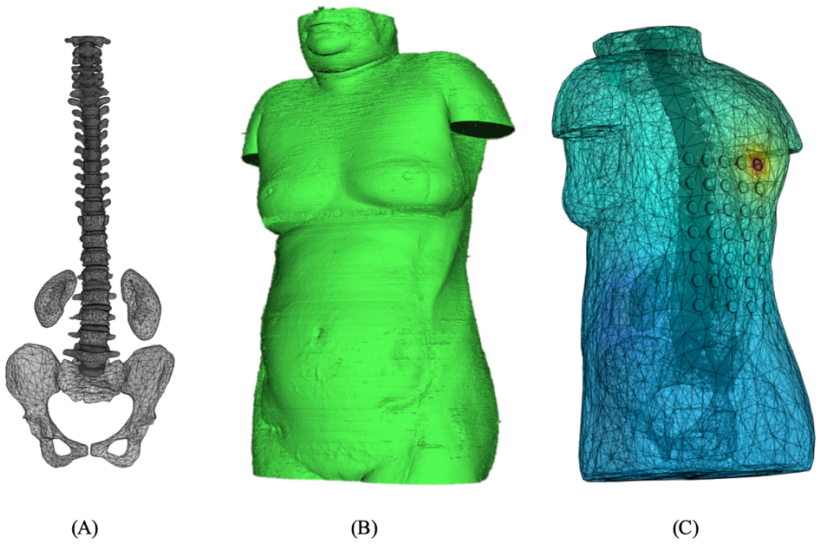

Figure 2.26: A better 3D model with more details and organs. (A) some of the organs in the new spinal cord model. (B) overall view of the new model. (C) a representative simulation result of the electrical stimulation using the new model.

The 3D model tested in the presented study preserves the realistic feature of the most important tissue, i.e., gray matter, white matter, vertebrae, and intervertebral disc. However, we simplified some structures to save the computational cost. For example, the three-layer skin was represented by an elliptic cylinder. In order to fully understand the tSCS effects for the research purpose, we keep developing a better 3D model, including refinements and more organs, as shown in Figure 2.26. The comparison between the simplified model and the sophisticated one may lead to the validation of the current simplified model and also shows the necessity of the sophisticated model.

In this section, we extended our work of the optimization-based multi-electrode array to achieve selectively spinal cord stimulation. We conducted computational experiments and compared the conventional tSCS and several common optimization algorithms. The quantitative

results show that the proposed algorithm SBFI can specify the currents at the electrode array. As a result, it is able to achieve the effective intensity of the stimulation of the spinal cord as the conventional tSCS does but affect fewer non-target segments as well. The choice of λ ($\boldsymbol{\lambda}$) in the algorithm is the key to balancing the intensity and selectivity. The proposed method SBFI has shown great potential in selective stimulation of the transcutaneous spinal cord and can significantly improve the stimulation focality.

CHAPTER 3

Functional Mapping, Modulation, and Monitoring of Mammalian Colon

In the previous chapter, we have developed non-invasive focusing neuromodulation techniques for the brain. In this chapter, we will discuss the functional study and modulation of part of the "second brain" - colon. The colon is considered part of the second brain as the enteric nervous system (ENS) is capable of functioning largely independent of the central nervous system (CNS), and the functional and chemical diversity of the neuron of ENS is similar to the CNS [79]–[83]. The functional mapping of the autonomic innervation of colon regions helps to gain a better understanding of the nerve circuitries and activities. With the knowledge, the neuromodulation technique can be applied to selectively stimulate the neural structures as effective and safe treatments for colon diseases.

In this chapter, we first introduce the background of autonomic nerve-colon functional mapping. A porcine model is a high translational value mammalian model to investigate several human diseases, including the detailed regional specific motility response to electrical stimulations at either colonic tissues or nerves. The use of safe and optimal tools to map colon motility is critical to understand underlying mechanisms of dysmotility and design appropriate treatments, such as neuromodulation. We present a novel technique of bio-impedance characterization to monitor colonic motor activity. The proposed bio-impedance-based method is shown to be viable for monitoring colonic motor patterns at high spatial and temporal resolution.

3.1 Introduction

The colon plays a critical role in the absorption of water, electrolytes and nutrients, storage of digesta as well as fermentation and generation of useful neuroactive molecules, elimination of gas, fluid, and solid waste with remarkable selectivity. Colonic motility is key in these complex functions, and dysmotility is associated with a variety of severe diseases such as gastroparesis adynamic ileus, chronic constipation, and diarrhea [84]–[89]. On the other hand, diseases such as

Hirschsprung's disease, spinal cord injuries, brain trauma and multiple sclerosis cause motility disorders that lead to chronic neurogenic colonic dysfunction with devastating emotional and quality of life impacts [86], [90], [91]. Although prokinetic or inhibitory pharmacological agents influencing motility or dietary interventions provide relief to several of these conditions in some patients, they suffer from low efficiency and side effects, while surgical removal of gut segments can affect the overall gut functions [88], [92].

In light of this therapeutic gap, interest in electroceutical-neuro-modulation is increasing as an alternative to mainstay therapies [93]–[95]. The rationale for the use of neuromodulation to treat refractory gut diseases is further strengthened by the fact that the gut is highly controlled by the electroceutically accessible autonomic nerves that impinge on the enteric nervous system [96]. Electrical stimulation can therefore be applied directly to the organ or to target nerves of the autonomic nervous system, which have specific innervation patterns [93], [97], [98]. While enthusiasm is high for this new therapeutic approach to alleviate colonic disorders, the optimal neuromodulation modalities, effects, and mechanisms are still not well known. Clinical and preclinical neuromodulation studies done thus far, on gut functions, have mainly targeted the stomach [99]–[101]. In past years, however, a number of electrical interventions have been tested

for treating colonic motility disorders both in experimental models and clinical settings, as recently reviewed [93], [97]. These include colonic electrical stimulation, sacral nerve stimulation, transcutaneous, or percutaneous tibial nerve stimulation, transcutaneous electroacupuncture, and transabdominal electrical stimulation [93], [97]. To date, the few clinical studies that have addressed the effect of the different types of neuromodulation on the lower gut function either by direct targeting the organ [102], [103] or by stimulating the autonomic nervous system [97], [104], [105], showed mixed outcomes of success and failures [97]. Reasons for this outcome inconsistency may be multiple, including the following: (a) the diversity of the targeted pathology (fecal incontinence, slow transit constipation, irritable bowel syndrome-constipation predominant, colonic inertia), (b) the gap in knowledge related to the colonic region-specific effects in response to ES of different nerves, (c) the lack of adequate evidence on the optimal stimulation parameters which are, for the most part, adopted from those established to be effective in urinary system dysfunction, (d) the variable and unpredictable motility pattern of the colon [106]–[109], (e) the lack of knowledge about potential colonic pacemakers [110], and (f) the limitations in the translatability of most preclinical models used (rodents, cat, dogs) to the human colon in terms of colon structure innervation, motility patterns, and diet. To address the latter, interest has grown over the past decade in the use of pigs as relevant preclinical models to study the pathophysiology of different organs due to their dietary, anatomical and physiological similarities with humans [111]–[113]. In particular, the pig colon, similar to humans, possesses unique tenia and sacculation [114] (not present in dogs, cats, rats, and mice). Both species are colon fermenters and have similar colonic microbial composition [115], [116]. Thus, the porcine model has both high face and construct validity to gain insight for better electroceutical therapy development. However, the influence of colonic neuromodulation on healthy pigs has been the object of a limited number of

reports so far. Most of these studies involve acute direct electrical stimulation on anesthetized and cleansed descending colon [117]–[120] or cecum [121], [122] using a broad range of stimulation parameters ($5-130\text{Hz}$, $0.03-3\text{ms}$, $7-30\text{mA}$). These protocols induce local contractions (single point of stimulation) [118], [122], propulsive contractions [120]–[122], luminal content movement [119], [122], or acceleration of colonic transit in response to sequential stimulations [119], [120], [123]. These data confirmed or expanded other preclinical studies performed in healthy [124]–[127] or constipation models [128], [129] in rodents, cats, and dogs. A few additional studies in pigs addressed the influence of the autonomic nervous system on the anorectal function and fecal evacuation by assessing the impact of neuromodulation targeting the pelvic nerve, hypogastric nerve, and sacral nerves [130]–[133]. While providing some insight into the potential beneficial effects of neuromodulation, the majority of these studies focused on the distal colon. The response of the different colonic regions, to a direct or selective nerve stimulation, has not been simultaneously studied. This is of importance because there is mounting evidence of clear regional differences in the colon both at structural and functional levels [134]. In addition, while the pelvic nerve, hypogastric nerve, and sacral nerves are well known to innervate the colon, the extent to which other extrinsic nerves, such as the vagus nerve, impinge on the colon is unclear. For instance, in humans, studies reported that vagal innervation extends from the upper gut up to the splenic flexure, while others reported that it continues further to include the rectal ampulae (see [135], [136]). Despite the ubiquity and key role of the vagus nerve in the brain-gut interactions, the neuromodulation of colonic motility by the vagus nerve has received limited interest thus far [137]–[139].

3.2 Functional Mapping

In view of those gaps, it is critical to understand the functional sphere of influence of specific nerves to develop efficient neuromodulation. Therefore, in the current study, we aimed to map the region-specific (proximal/ascending colon, transverse colon, and distal/descending colon) motility response to selective electrical stimulation applied directly on each of the colonic proximal colon, transverse colon, distal colon segments, or the abdominal vagus nerve (specifically the celiac branch), sacral nerves (S1-S4), and thoracolumbar nerves (specifically T12 and L1) in a healthy porcine anesthetized model.

3.2.1 Animals

Yucatan minipigs, male castrated at 7 days of age (~7 months old, 25-36kg), were obtained from S&S Farms and group housed in pens (either bedding or grate floor, depending on housing availabilities – 2 pigs/pen, 42ft^2) in an environmentally controlled room (lights on/off 6 AM/6 PM, $61 - 81°\text{F}$) under specific pathogen-free conditions. All pigs received ad libitum access to diet (5p94 Prolab mini pig diet, PMI nutrition) and filtered tap water. All husbandry practices and procedures were conformed to the NIH Guide for the Care and Use of Laboratory Animals (8^{th} edition) and were reviewed and approved by the UCLA Animal Research Committee (Institutional Animal Care and Use Committee) under protocol #2018-074-01. All efforts were made to minimize any suffering and the number of animals used.

3.2.2 Equipment & Methods

3.2.2.1 Electrodes, leads, and stimulator

The planar electrode arrays were produced on 8μm thick polyimide substrates, providing the mechanical flexibility and durability to withstand the motion of the intestine. The electrodes were fabricated using e-Beam evaporation deposition to create layers with a thickness of 200nm platinum and 10nm titanium [9], [140], [141]. Each electrode had a geometric size of 500μm×200μm, and a surface roughness process was applied to increase the effective surface area and thus increase the charge storage capacity. Each planar electrode array contained six rows of three individual electrodes (18 channels total) that could be potentially used for stimulation and recording [140].

3.2.2.2 Experiment protocol

For all the experiments, pigs were fasted for at least 12 hours prior to surgery with free access to water. On the day of surgery, pigs were premedicated with midazolam (1mg/kg, cat # 067595, Covetrus), ketamine (15mg/kg, cat # 068317, Covetrus), and meloxicam (0.3mg/kg, # 049755, Covetrus) injected intramuscularly. They were then intubated, connected to a respirator for ventilation (13-16 breaths/min) and maintained under general anesthesia with 1%-3% inhaled isoflurane. Maintenance fluids (Lactated Ringers, cat # 059380, Covetrus) were administered at 10mL/kg/h.

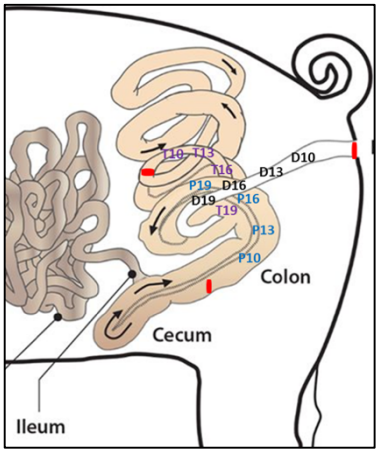

Figure 3.1 Schematic representation of colonic manometry probe positions in overnight fasted and anesthetized adult male castrated Yucatan pigs.

Manometry sensors were positioned at 10, 13, 16, and 19 cm from the ceco-colic junction (P10, P13, P16, P19) from the distal end of the proximal/ascending colon (T10, T13, T16, T19) and from the anal verge (D10, D13, D16, D19).

During the first part of the surgical procedure, pigs were positioned on a heating pad (32°C) in the supine position. ECG electrodes and a femoral arterial line were placed. When needed, the heart line was flushed with sterile saline containing 0.5% heparin. A midline abdominal incision was performed to gain access to the peritoneum. Three colonic regions of interest-proximal/ascending colon, transverse colon, and distal/descending colon-were identified and externalized. Flexible solid-state-manometry probes (MikroCath^{TM} diagnostic pressure catheter, cat # 825-0101, Millar Inc) were inserted into the different segments of the colon via a small incision and maintained in position with a loophole silk ligature. For the proximal colon, 4 manometric probes were inserted about 10cm below the ceco-colic junction, at 10,13,16, and 19cm from the point of entry. For the transverse colon, 4 manometric probes were inserted at the end of

the proximal colon at 10, 13, 16, and 19cm from the point of entry. Distal probes were inserted in the distal colon through the anus with sensors at 10, 13, 16, and 19cm proximal to the anal verge. For each region, four single sensor probes were mounted together in stagger such that the sensors were spaces 3cm apart. An addition sensor was also added in the anal canal (AC) for the sacral or thoracolumbar nerve electrical stimulation study.

Pigs were euthanized at the end of the experiment with an intravenous injection of pentobarbital (100mg/kg cat # 009444; Covetrus).

3.2.2.3 Assessment of colonic motor function

Gastrointestinal motility is critical to digestive health, and its dysfunction contributes to multiple diseases. Gut motility is complex, and its accurate analysis remains a challenge. This is particularly important to assess the effectiveness of emerging therapies, such as neuromodulation, against gut motility disorders. In this study, the colonic motility is monitored by intracolonic pressure. The colonic motility time-domain changes are first quantified. Spectral analysis is then done to uncover important features (frequency pattern and power) of intestinal phasic contractions under different protocols.

Intracolonic pressure (manometry) recording procedure

Each pressure transducer catheter was connected via pressure cables (PEC-10D, cat # 850-5090, Millar Inc) to a transducer (PCU-2000, cat # 880-0129, Millar Inc). The signal was acquired via a Micro1401 analog-to-digital interface (Cambridge Electronic Design, Cambridge, UK) at 100 samples/s and recorded with Spike 2 version 7.10 data acquisition software (Cambridge Electronic Design). The system was calibrated by using know pressure at 0, 20, 40, and 60mmHg at the start of each experiment to convert voltage output to intraluminal pressure. Abdominal

contractions and breathing artifacts were excluded by smoothing the original trace with a time constant of 2s. Recording of motility data began after surgery was completed and continued for at least 30 min for stabilization of baseline motility and then for at least another 30min following completion of the stimulation experiment.

Intracolonic pressure data analysis

Motility Index: Colonic contractile pressure changes were quantified by measuring the area under the curve of the phasic component of the intraluminal pressure trace (pAUC) every minute and reported as motility index. The phasic component of intracolonic pressure was extracted from the original trace as previously reported [107].

Generation of colonic motility pressure maps (colon luminal pressure and contraction frequency power map) and video animation: For visual representation of the strength of pressure changes and their regional distribution across the colon, luminal pressure changes (motility index/min), at basal and in response to electrical stimulation were processed as heat map images using MATLAB code. Likewise, the contraction frequency band power changes are generated using the same software. In addition, the motility index data was used to generate video animation to view the propagative nature of pressure changes.

Spectral analysis of pressure changes: Spectral power analysis of luminal pressure changes in the proximal colon, transverse colon, and distal colon at basal and in response to colonic electrical stimulation and post-stimulation periods were done for each of the pressure sensor probes. After removing the DC component, fast Fourier transform (FFT) was applied to obtain the frequency spectra. The integrated power of the prominent 0-12cpm frequency band and the dominant frequency band (1-6cpm) were then calculated using a lab-written MATLAB code. The pressure wave data have frequency components that can be unveiled using FFT. The conditional

relationship between frequency resolution and time window at low frequency (1-12cpm) was carefully chosen such that accurate FFT analysis was obtained. The power of the frequency component indicates (a) the amplitude of the activity in a specific frequency band and (b) how much activity in that frequency band was present during the period of analysis.

Statistical analysis: Normality, differences in variance and the presence of outliers were determined via the Kolmogorov-Smirnov test, *F* test, and Grubbs' testing, respectively, prior to further statistical analysis. There were no outliers removed. GraphPad Prism v.5.01 (GraphPad Prism) software was used to perform statistical analysis. Time course response of the motility index was analyzed using repeated measure 2-way ANOVA and Bonferroni *post hoc* test. Mean motility index expressed in % baseline data were analyzed using repeated measure one-way ANOVA and Tukey's or Dunn's *post hoc* test. Motility index expressed as mean changes from baseline were analyzed using Wilcoxon paired or Mann-Whitney unpaired t-tests as appropriate. Contraction frequency power changes were analyzed using repeated measure 2-way ANOVA and Sidak's *post hoc* test. Data are presented as mean $\pm$ SEM $P < 0.05$ indicates a significant difference.

3.2.3 Stimulation Protocol

3.2.3.1 Direct colonic tissue electrical stimulation

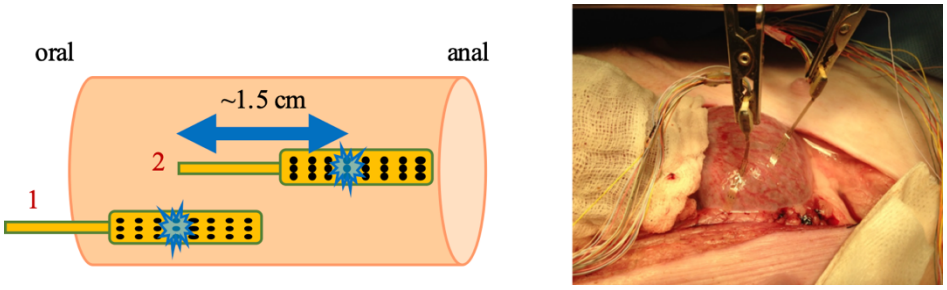

Figure 3.2: Direct colonic tissue electrical stimulation setup.

After the insertion of the sensors, planar electrode arrays were placed onto the serosal surface of the colonic region of interest (proximal colon, transverse colon or distal colon) for stimulation as described in the previous studies (Figure 3.1) [9], [140]. The electrodes were positioned to lie on the serosal side of the first 3 luminally placed pressure sensors (10-16cm). A baseline was established for a period of 10 min, and stimulation was initiated using the customized stimulation device [9], [141]. Two stimulation electrodes, configured as bipolar pair and (1.5cm apart), were stimulated alternatively.

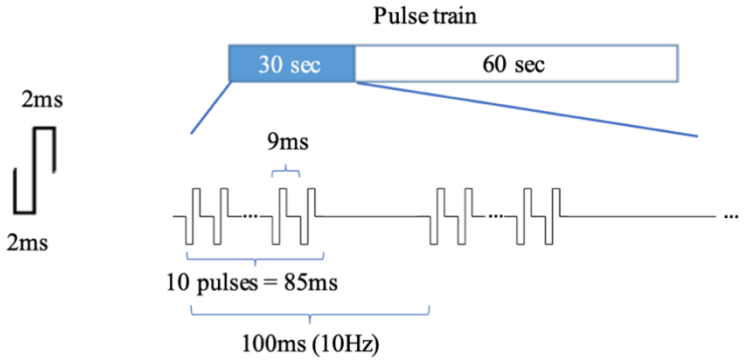

Figure 3.3: Direct colonic tissue electrical stimulation protocol.

The protocol of direct colon stimulation was done with 5 cycles of alternating stimulation of electrodes #1 and #2 (a total of 10 consecutive cycles) at 10 Hz, 2 ms, 15 mA, 30 s ON, 60 s OFF for a total duration of 15min (Figure 3.2). The stimulation parameters were chosen based on sweep trail studies using diverse stimulation parameters performed under our conditions of experimentation (2-100Hz, 2-4ms, 4-15mA) (https://doi.org/10.26275/ajkk-l7xd) and reported in prior studies [9], [140] to cause contractions or stimulate propulsion.

3.2.3.2 Abdominal vagus nerve electrical stimulation

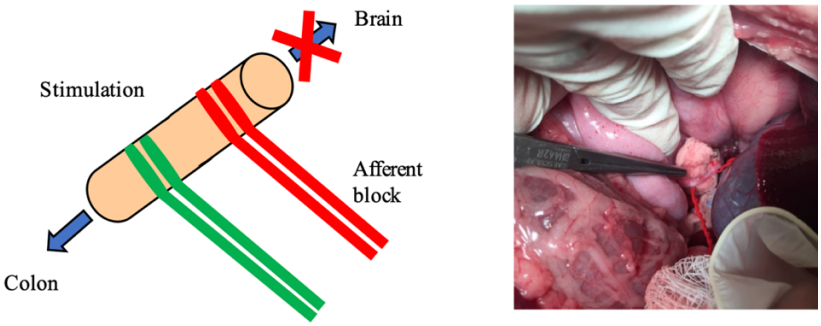

Figure 3.4: Abdominal vagus nerve electrical stimulation setup.

The posterior branch of the abdominal vagus nerve was exposed through a midline abdominal incision. An incision was made starting at the midline above the xyphoid process and moved diagonally to the animal's left. The muscle was blunt dissected along the incision and held open using a retractor. We carefully retract the left liver lobule, cut the hepatoduodenal ligament, and move the right liver lobule aside to reveal the esophagus. After identification of the esophagogastric junction, the lesser omentum and the esophageal hiatus were opened, the right diaphragmatic crus was identified, and the posterior vagus nerve was dissected free from the

esophagus. We then located the celiac branch of the left vagus nerve and placed one hook electrode 5-10mm apart (Figure 3.3) to produce stimulation. Another nerve block hook electrode was placed 1-2cm proximal from the stimulation electrodes (Figure 3.3). Particular care was taken during this procedure to minimize nervous tissue damage, and the vagal trunk was not grasped directly at any time. The posterior branch was chosen since it arises from the right cervical vagus nerve and innervates the small intestine and the colon avoiding the major hepatic branches that leave off the anterior branch of the abdominal vagus [142].

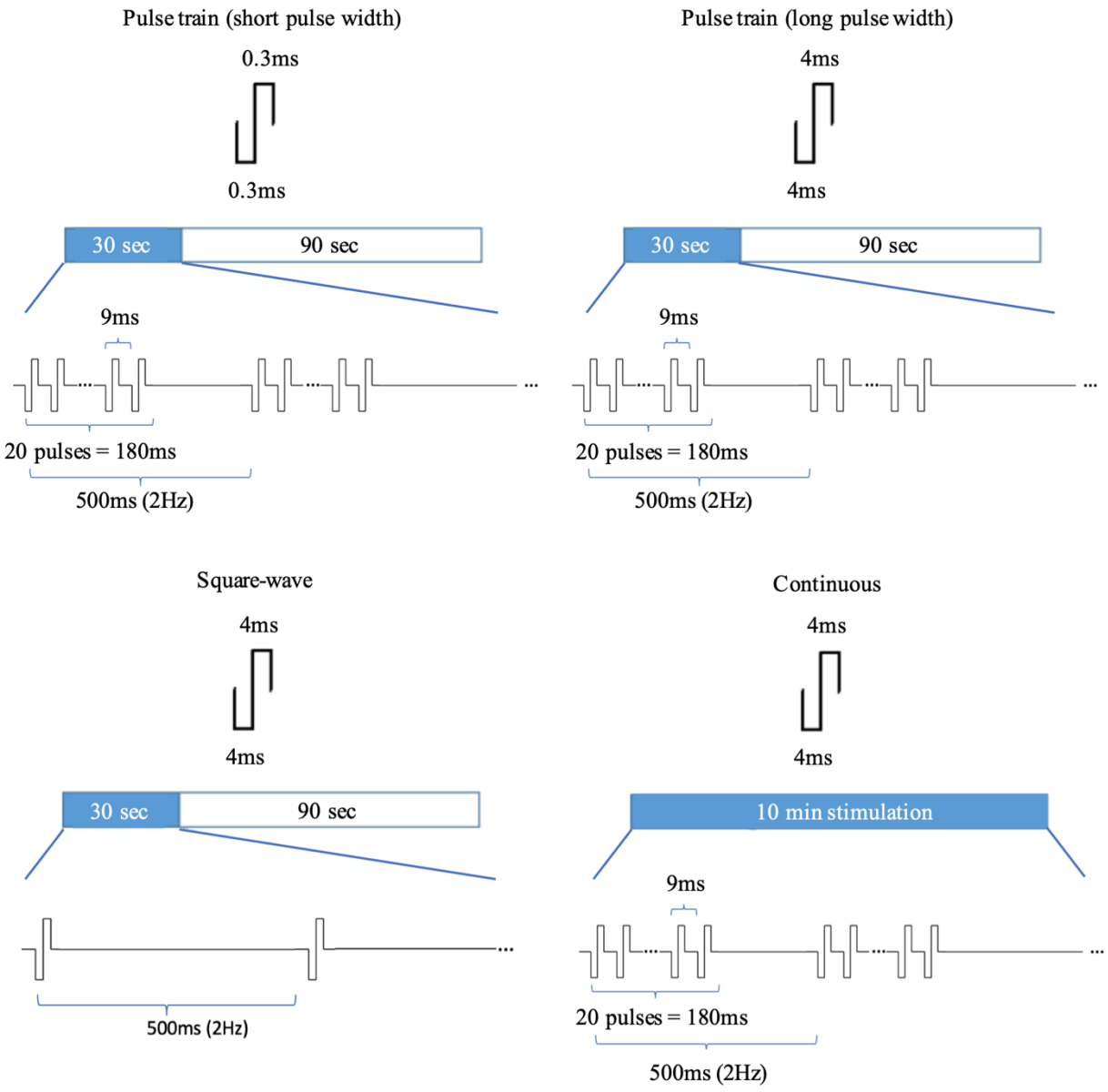

Figure 3.5: The celiac branch of the abdominal vagus nerve electrical stimulation protocols.

The CBVN was stimulated with the following protocols: pulse train, 2Hz, 0.3 or 4ms, 5mA, 5 cycles of 30s ON and 90s OFF for a total duration of 10 min (Figure 3.4). In addition, the effect of different protocols of electrical stimulation, including continuous and square-wave, was

evaluated. For CBVN nerve block, anodal block with 200Hz, 0.1ms, 2mA parameters were determined based on a sweep trail study with different combinations of parameters.

3.2.3.3 Sacral nerve root electrical stimulation

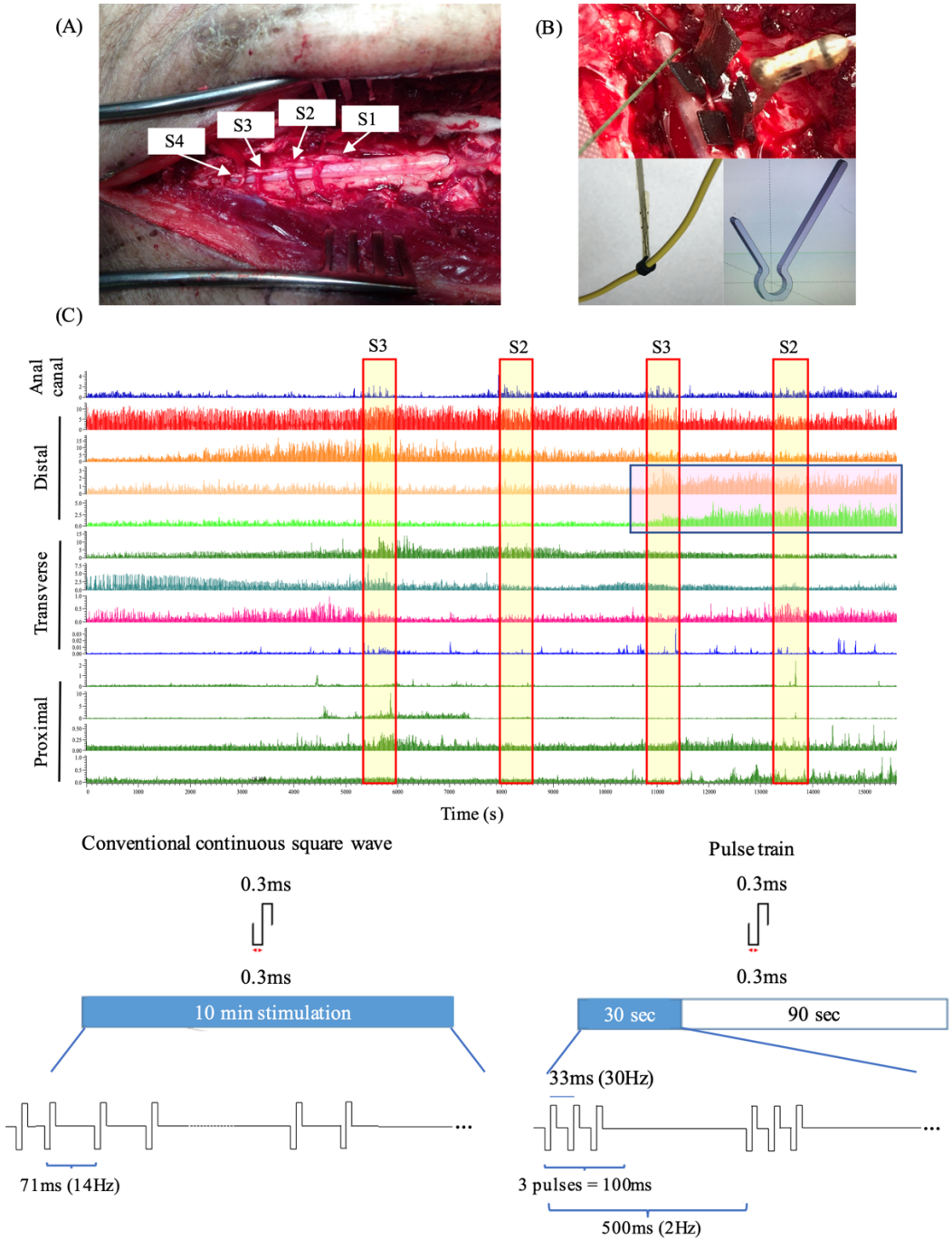

Figure 3.6: Sacral nerve root electrical stimulation setup and protocols.

(A) Picture of the sacral roots (S1, S2, S3 and S4) isolated following laminectomy in an anesthetized male Yucatan pig. (B) A 3D-printed holder was used to ensure the well-contact of the electrode and nerve. (C) Raw traces example of spinal root stimulation in an anesthetized pig using a sweep trial for optimal electrical parameters to stimulate motility of the colon, as well as contractions and motility in the anal canal. The first S2/S3 stimulations were done using conventional continuous 14Hz, 0.3 ms, 0.5 mA, the latter two with 2Hz, 0.3ms, 0.5mA pulse train with 30Hz, 3 pulses per train. Note the increase in anal canal contraction during both frequency stimulation while the distal colon stimulation occurs mainly during and post 30 Hz stimulation (highlighted D16-D19 sites).

After the first part of the surgery to place pressure sensors in the proximal and transverse colon, the abdomen was then closed, and the pig was placed on prone position, leaving access to the back. The S1-S4 sacral spinal nerves (S1/2 vs. S3/4) were accessed via a laminectomy (Figure 3.5 (A)). (surgery time: 30 min-40 min). Laminectomy is a common spine operation and refers to the surgical removal of the vertebral lamina, thereby unroofing the vertebral canal. We followed the following processes similarly as described in this reference [143].

Before surgery, we palpated the lumbar spinous processes along the midline and identified the vertebral levels of interest (S1-S4). A midline incision using a scalpel/electrocautery was then performed, and the subcutaneous tissue and fat were dissected to gain access to the thoracolumbar or lumbosacral fascia. The fascia along the midline was cut to expose the supraspinous ligaments spanning between spinous processes. The supraspinous ligaments were open over a few millimeters. Then using a Freer elevator, the supraspinous ligaments were gently detached from

spinous processes (subperiosteal dissection). The dissection was then extended to the interspinous ligaments up to the facet joints of the spinous processes along the area of interest. After locating the lamina, we opened the lamina using a surgical saw or a Kerrison rongeur to extract bone in a piece-wise fashion over the whole vertebral segment of interest in order to gain access to the ligamentum flavum, periosteum, epidural fat, and dura sac. The spinous processes corresponding to the region of interest were removed, allowing access to the meninges. The epidural fat was gently removed, taking care not to damage the dura sac and allowing identification of the spinal roots.

During the surgical procedure and as the laminectomy was completed, hemostasis was performed with bipolar electrosurgery. Monopolar electrosurgery was not used because of the proximity of neural structures.

Bone wax was placed along with sites of bleeding from exposed bone, and absorbable hemostat dressing was used to obtain hemostasis near soft tissue. We also used cotton to wick serous fluid and blood away from the dissection where necessary.

After surgery, sacral root nerves (S1- S4) were identified and isolated using small pieces of cotton. Cuff electrodes were used to produce stimulation alone or concomitantly with a nerve block, either afferent (to assess the role of efferent fibers) or efferent (to investigate the role of afferent fibers).

In the sacral nerve root stimulation (SNS) study, unilateral (left root) SNS was performed as there is no significant difference between the nerves of the two sides and no demonstrable connection between them [144].

The sacral nerves are thin, delicate and friable; therefore, the flexible planar electrodes were used to wrap and stimulate the nerve in order to avoid nerve damage. An electrode holder was

designed and fabricated with soft 3D printing material to keep the well-contact between electrodes and nerve and ensure the stimulation quality (Figure 3.5 (B)). The sacral nerve root (S1-S4) was stimulated with the following protocols: 2Hz, 0.3ms, 0.5mA pulse train with 30Hz, 3 pulses per train, 5 cycles of 30s ON and 90s OFF for a total duration of 10min. For sacral nerve block, kilohertz frequency blocking (40 kHz, 2 V, sinusoidal wave) was chosen. The effectiveness of stimulation and blocking was determined based on a sweep trail study with different combinations of parameters. Figure 3.5 (C) is a raw trace example of a stimulation effectiveness study. The first S2/S3 stimulations were done using conventional continuous square wave parameters (14Hz, 0.3 ms, 0.5 mA) [105], [145], [146], the latter two with the selected pulse train parameter. The increase in anal canal contraction can be observed during both frequency stimulation, while the distal colon stimulation occurs mainly during and post pulse train stimulation (highlighted D16 and D19 sites). Less colonic activities were overserved in response to the conventional continuous square wave protocol. Therefore, the pulse train stimulation protocol was used for the sacral nerve studies.

3.2.3.4 Thoracolumbar nerve root electrical stimulation

After the first part of the surgery, the abdomen was then closed, and the pig was placed on prone position, leaving access to the back. With a laminectomy, the thoracolumbar (T12 and L1) nerve root was exposed and identified. We followed similar processes as described in the sacral nerve root electrical stimulation section.

In the thoracolumbar nerve root stimulation (TNS) study, unilateral (left root) TNS was performed with a needle electrode placed on the T12 or L1 spinal root proximally to the dorsal root ganglion (targeting afferent fibers only) or distally to the dorsal root ganglion (targeting both afferent and efferent fibers). In this study, The TNS was done with either continuous 10Hz, 0.3ms,

0.5mA square wave stimuli or 2Hz, 0.3ms, 0.5mA pulse train with 30Hz, 3 pulses per train, 5 cycles of 30s ON and 90s OFF for a total duration of 10 min (Figure 3.6).

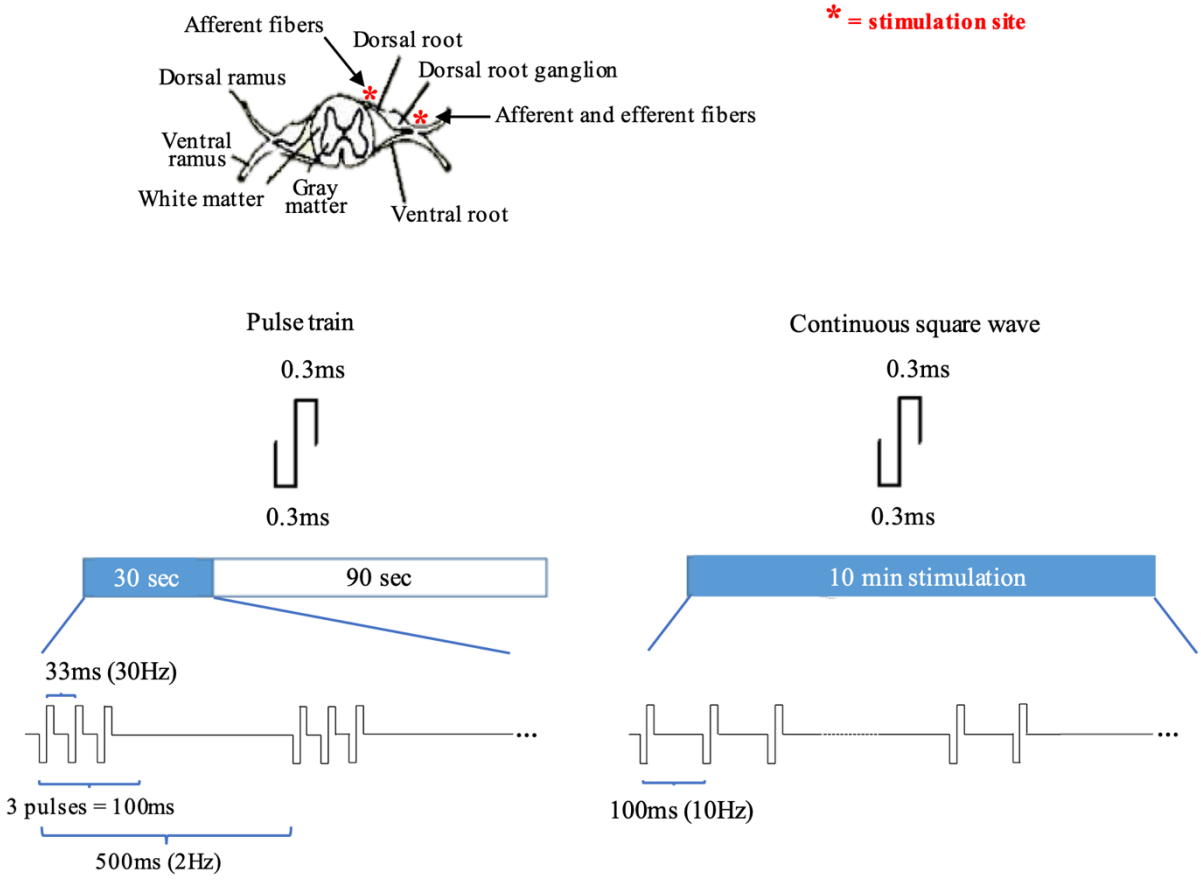

Figure 3.7: The thoracolumbar nerve root T12/L1 electrical stimulation protocols.

In this study, we used a needle electrode instead of the cuff electrode due to the technical challenges. Accessing the distal segments of the thoracolumbar spinal nerve roots for cuff electrode placement is difficult. Bleeding and side effects of systemic responses (increased blood pressure and heart rate) were observed. The vertebral processes limit the anatomical space for root access and placement of cuff electrodes, and bleeding is profuse in this area. We have attempted to use absorbable hemostats (Surgicel) to reduce the bleeding without great success. As an

alternative, we used needle electrode stimulation of the root before and after dorsal root ganglions. So far, nerve blocking using needle electrodes is not feasible. Therefore, we did not include the blocking study here.

3.2.4 Results

3.2.4.1 Direct colonic tissue electrical stimulation

Colon motility was recorded for over 3 hours without any electrical stimulation in a few pigs (n=3). After the initial 30min post-surgery, the colon motility remains stable throughout the experimental recording. Effective delivery of electrical current to the colon was confirmed by the direct measurement of electrode overpotential. Activation of the electrode also corresponded with an immediate local contraction of the colonic segment directly under the electrode. Data associated with this study [147] were collected as part of the Stimulating Peripheral Activity to Relieve Conditions (SPARC; RRID: SCR_017041) project and are available through the SPARC Data Portal (RRID: SCR_017041) under a CC-BY 4.0 license.

Table 3.1: Colonic mean motility index (in % baseline) during stimulation (15 min) and post-stimulation (30 min) in response to direct proximal, transverse, and distal colonic stimulation in anesthetized male Yucatan pigs.

Note: Data are mean ± SEM of n as indicated for each probe/set. Repeated measure one-way ANOVA and Tukey's post hoc test, *P < .05, **P < .01, and ***P < .001 vs baseline (100.0 ± 0.0%), +P < .05, ++P < .01 vs stimulation.

		n	Stimulation	Post-Stimulation
Direct Proximal Colon Stimulation	P10	13	$209.0 \pm 28.1^{***}$	$127.2 \pm 11.8^{++}$
	P13	12	$159.5 \pm 30.9^{*}$	131.4 ± 17.0

	P16	7	186.5 ± 34.1	270.1 ± 71.6*
	P19	7	163.6 ± 31.3	162.0 ± 51.0
	T10	14	118 ± 12.1	125.6 ± 20.5
	T13	13	112.6 ± 16.3	109.8 ± 25.9
	T16	15	102.1 ± 10.5	89.0 ± 12.2
	T19	15	114.5 ± 7.0	108.7 ± 24.9
	D10	14	111.4 ± 10.7	114.7 ± 13.5
	D13	13	111.3 ± 7.0	128.1 ± 17.7
	D16	14	103.5 ± 6.7	121.6 ± 14.5
	D19	12	96.0 ± 10.7	129.7 ± 24.3
Direct Transverse Colon Stimulation	P10	5	95.6 ± 12.7	117.3 ± 26.1
	P13	7	92.2 ± 10.5	131.9 ± 27.1
	P16	7	102.5 ± 14.0	85.2 ± 10.6
	P19	8	125.2 ± 17.9	109.6 ± 28.8
	T10	6	240.2 ± 26.8*	123.2 ± 24.4
	T13	7	124.9 ± 21.7	104.9 ± 18.0
	T16	8	125.2 ± 14.8	105.7 ± 16.7
	T19	8	118.9 ± 14.7	99.81 ± 10.3
	D10	8	125.7 ± 19.7	137.3 ± 24.7
	D13	7	139.5 ± 21.5	171.0 ± 30.9
	D16	8	153.9 ± 26.9	192.8 ± 29.5*
	D19	7	141.8 ± 28.2	119.3 ± 20.2
Direct Distal Colon Stimulation	P10	2	86.4 ± 13.2	73.8 ± 12.7
	P13	6	143.4 ± 9.4*	118.4 ± 16.4
	P16	5	142.9 ± 17.6	131.6 ± 33.1
	P19	5	142.7 ± 28.3	141.0 ± 53.6
	T10	5	92.5 ± 9.8	106.6 ± 3.7
	T13	5	106.0 ± 12.1	97.7 ± 21.1
	T16	6	109.0 ± 12.0	123.5 ± 15.5
	T19	6	135.8 ± 24.4	156.1 ± 21.0
	D10	4	115.5 ± 9.7	152 ± 41.1
	D13	6	131.4 ± 20.2	149.1 ± 40.7
	D16	5	129.5 ± 15.9**	192.8 ± 23.7+
	D19	6	147.3 ± 23.80	193.2 ± 77.69

Proximal colon electrical stimulation

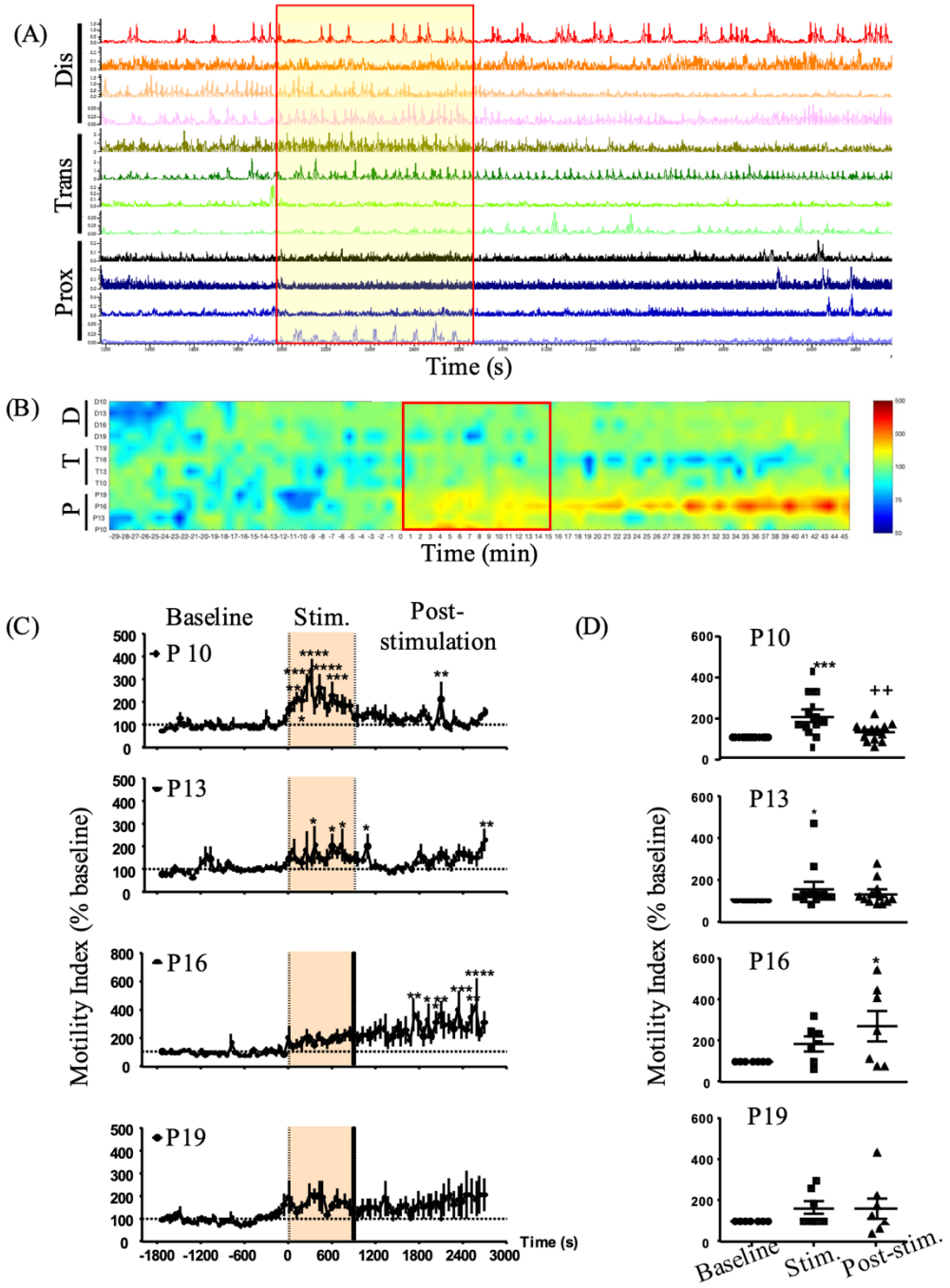

Figure 3.8: Influence of direct proximal colon electrical stimulation as monitored by manometry in anesthetized pigs (n = 7-15 each).

(A) Representative trace of direct proximal colon stimulation; (B) pressure map representation; (C) time course response of the motility response recorded by the different proximal probes (P10, P13, P16, P19) at basal, during and post direct proximal colon electrical stimulation (motility index, % baseline) (n = 7-13). Traces show the baseline response (30 min), stimulation (15 min), and post-stimulation (30 min) periods. Data are mean ± SEM, 2-way ANOVA and Bonferroni's post hoc test, *P < .05, **P < .01, ***P < .001, ****P < .0001 vs baseline. D, Mean motility index change (% baseline) during baseline (30 min), stimulation (15 min), and post-stimulation (30 min) in proximal (n = 7-13 pigs) regions. Data are mean ± SEM, repeated measures one-way ANOVA and Tukey's post hoc test, *P < .05, ***P < .001 vs baseline, $^{++}$P < .01 vs stimulation. Channels represent the position of the different manometry probes in the different colonic parts (P: proximal, T: transverse and D: distal).

Stimulation of the proximal colon induced a very strong circular muscular contraction observed visually (supplementary video 2). This contraction was also detected on manometry recordings (Figure 3.7 (A) and Table 3.1). This was followed by a marked activation of the proximal colon for the next 30min, and an overall trend to decrease the motility in the transverse colon as shown on the pressure map (Figure 3.7 (B)), which did not reach statistical significance (Table 3.1). The distal colon motility remained unchanged throughout the recording period (Figure 3.7 (B) and Table 3.1). Time course response of the motility index of the proximal colon at each of the 4 proximal sensors (Figure 3.7 (C)) showed increased motility index (% change of baseline) during stimulation (P10 and P13) and post-stimulations (P16), suggesting a possible propagation

from P10-P13 sites to the P16 site. Similarly, a comparison of the mean motility index of the basal vs. the stimulation or post-stimulation period showed an increased mean motility index at P10 and P16 (during stimulation) and P16 (during the post-stimulation period) (Figure 3.7 (D)).

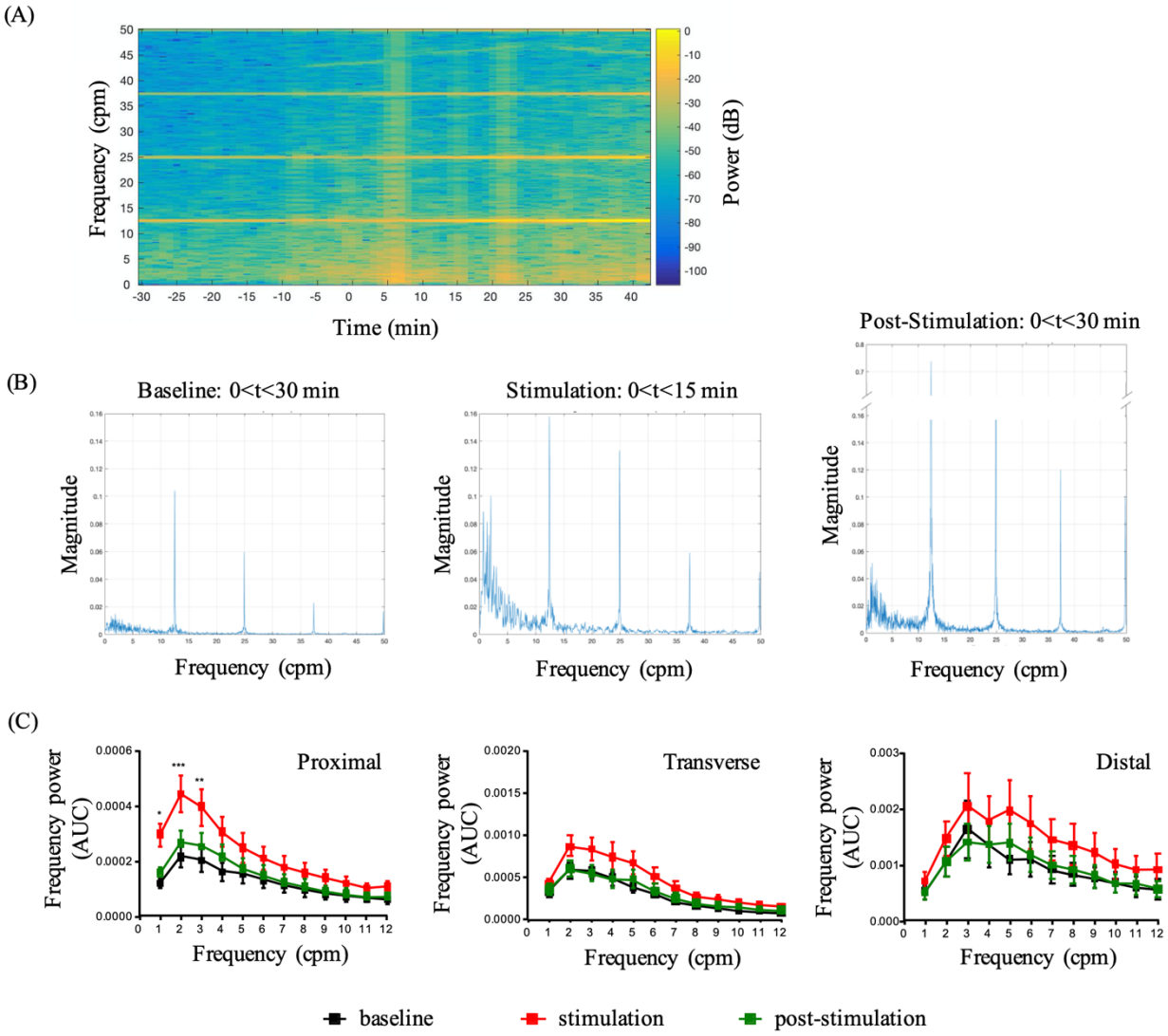

Figure 3.9: Influence of direct proximal colon electrical stimulation on the regional colonic frequency power spectrum.

(A) Representative spectrogram of the proximal colon frequency power spectrum in an anesthetized male Yucatan minipig in response to direct proximal colon electrical stimulation.

Note that most of the frequency power comes from the ~0-12 cpm band. (B) representative periodogram showing dominant frequency band (~1-6 cpm) during baseline, stimulation, and post-stimulation periods. Note that the power of the 1-6 cpm band is increased during stimulation and post-stimulation periods. Note also (in A and B), the breathing artifact and its harmonic waves are straight and stable. The breathing artifact (~12.5 cpm in this example) is the original frequency. The harmonic waves (~25, 37.5, 50 cpm in this example) represent artifact frequency that is a positive integer multiple of the frequency of the original wave (breathing artifact). (C) Aggregated data on frequency power spectrum in the proximal, transverse, and distal colon in response to direct proximal stimulation (cumulative recordings from 4 probes per colonic region in n = 7-15 pigs). Direct ES of the proximal colon increased the power of the 1-12 cpm frequencies in all regions, with a statistical significant difference in the 1-3 cpm frequencies in the proximal colon. Data are mean ± SEM, repeated measures two-way ANOVA and Sidak's post hoc test, *P < .05, **P < .01, ***P < .001, vs baseline in respective groups

Spectral power analysis of contractions at baseline was characterized by prominent frequency power of 0-12 cycles/min (cpm) band in all the colonic regions. The frequency band of 13-17 cpm was overwhelmed by the high power of the ventilator/breathing frequency, while higher frequency bands had too low or negligible power (Figure 3.8 (A) and (B)). The frequency band-to-frequency power (Figure 3.8 (C)) shows a hump (dominant power) in the range of 1-6cpm band. Direct proximal electrical stimulation significantly increased the mean power of the 1-3cpm frequencies and caused an overall increase in the 0-12 cpm frequency band (Figure 3.8 (C), left panel). A trend to increase in the power of frequency spectrum was also observed in the transverse colon (Figure 3.8 (C), middle panel) and distal colon (Figure 3.8 (C), right panel), but these did not reach

statistical significance. The integrated spectra showed a return to baseline levels in all regions within the 30min post-stimulation analysis.

Transverse colon electrical stimulation

Stimulation of the transverse colon also induced a circular muscular contraction observed visually. These contractions are also detected on manometric recordings in anesthetized pigs (Figure 3.9 (A)). As in proximal colon response, stimulation of the transverse colon showed increased luminal pressure heat map primarily occurring in the transverse colon (Figure 3.9 (B)). After the end of the transverse colon stimulation period, the motility index was increased in the distal colon and with a non-significant increased trend in the proximal colon, while transverse colon motility was back to baseline levels (Figure 3.9 (B); Table 3.1).

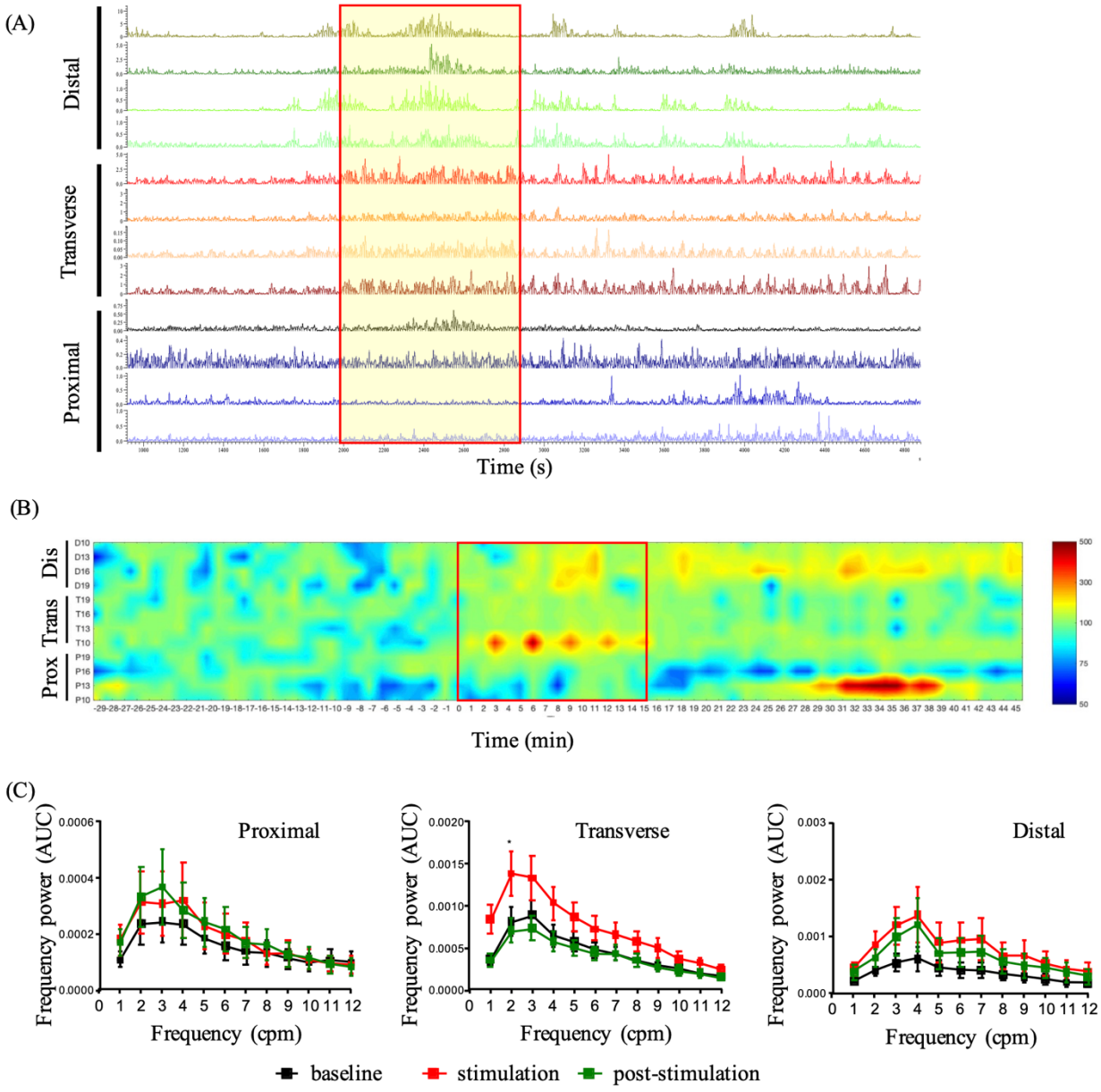

Figure 3.10: Influence of direct transverse colon stimulation as monitored by manometry in anesthetized pigs (n = 5-8 each).

(A) Representative trace of direct transverse colon stimulation; (B) pressure map representation. Channels represent the position of the different manometry probes in the different colonic parts (Prox: proximal, Trans: transverse, and Dis: distal). (C) Frequency power spectrum in the proximal, transverse, and distal colon in response to direct transverse stimulation

(cumulative recordings from 4 probes per colonic region in n = 5-8 pigs). Direct electrical stimulation of the transverse colon increased the power of the 1-12 cpm frequencies in the transverse and distal colon, with a statistically significant difference in the 2 cpm frequencies in the transverse colon. Data are mean ± SEM, repeated measures two-way ANOVA, and Sidak's post hoc test, *P < .05 vs. baseline in respective groups

Spectral analysis showed, like the proximal colon, a prominent 0-12cpm band power with the 1-6cpm being the dominant range as shown in the frequency band-to-frequency power curves (Figure 3.9 (C)). Electrical stimulation of the transverse colon increased the power of the 1-6cpm band in the transverse colon, reaching statistical significance for the 2-3cpm frequencies ($P<0.05$) (Figure 3.9 (C)). The transverse colon post-stimulation response was characterized by the decrease in the power to the level of the corresponding basal time. The responses of the proximal colon and distal colon to the transverse stimulation displayed variable changes, a reflection of the motility index, and pressure map images.

Distal colon electrical stimulation

The distal colon stimulation, unlike the proximal colon and transverse colon, induced a longitudinal contractile response (supplementary video 3) and increased the manometric recording (Figure 3.10 (A)) and motility index (pressure heat map) in the distal colon during the stimulation period (Figure 3.10 (B)). This was followed in the post-stimulation period by a strong activation of contraction in the distal colon. Probes at the proximal colon and transverse colon showed variable activation and inhibition of motility (Figure 3.10 (B) and Table 3.1).

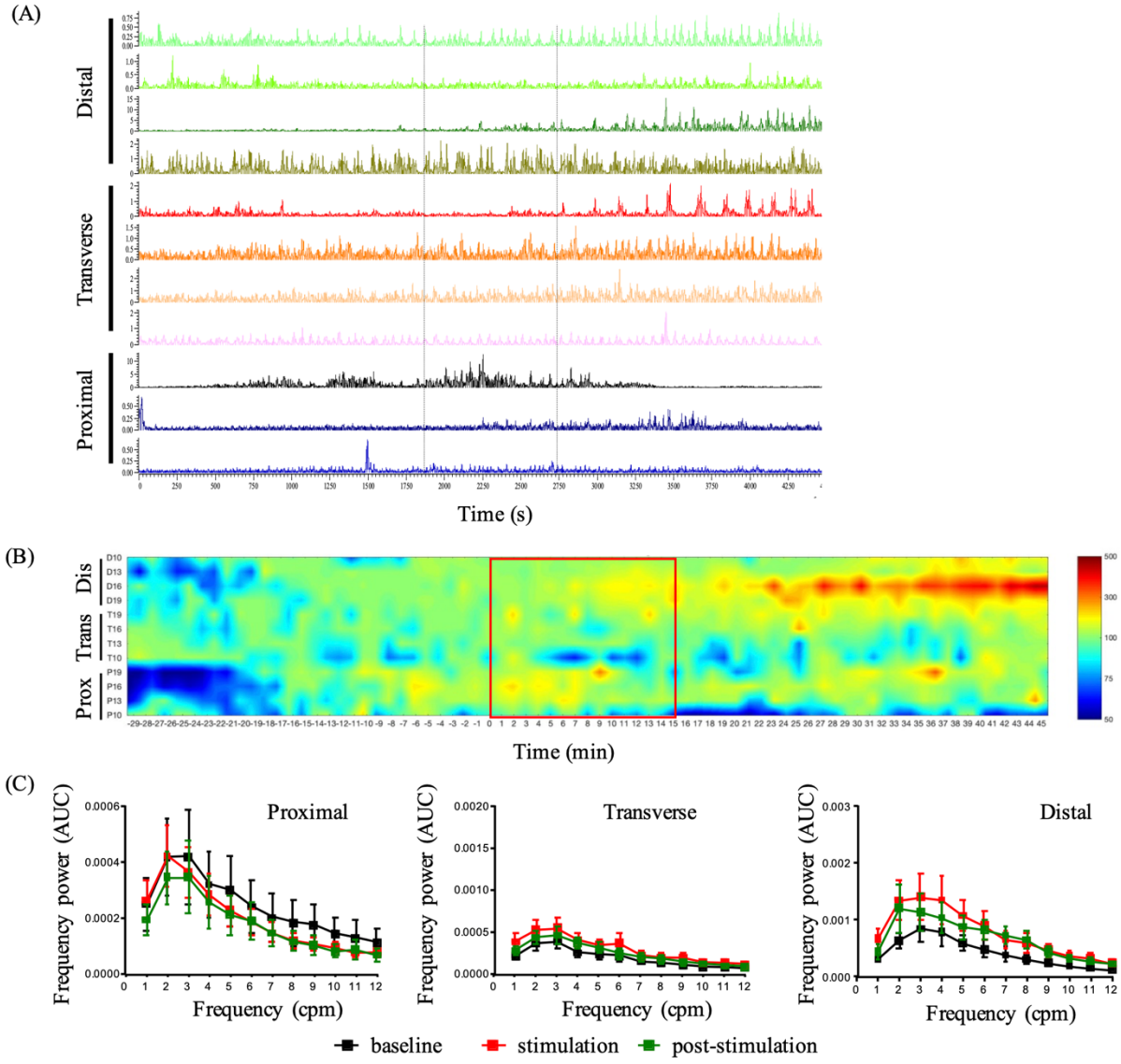

Figure 3.11: Influence of direct distal colon stimulation as monitored by manometry in anesthetized pigs (n = 2-6 each).

(A) Representative trace of direct distal colon stimulation. (B) Pressure map representation. Channels represent the position of the different manometry probes in the different colonic parts. (C) Frequency power spectrum in the proximal, transverse, and distal colon in response to direct distal stimulation (cumulative recordings from 4 probes per colonic region in n = 2-6 pigs). Direct

ES of the distal colon induced a trend for an increase in the power of the 1-12 cpm frequencies in the distal colon exclusively. Data are mean ± SEM

Spectral analysis of the distal colon motility displayed a similar basal frequency band (0-12cpm) as observed in the other colonic regions. Direct electrical stimulation caused only a trend to increase the 1-6cpm power locally during the stimulation, while the other regions remained unaffected. The distal colon response during the post-stimulation period returned to basal power distribution.

In all colonic regions, direct electrical stimulation induced short-distance anterograde and retrograde propagating contractions (see example in supplementary video 4).

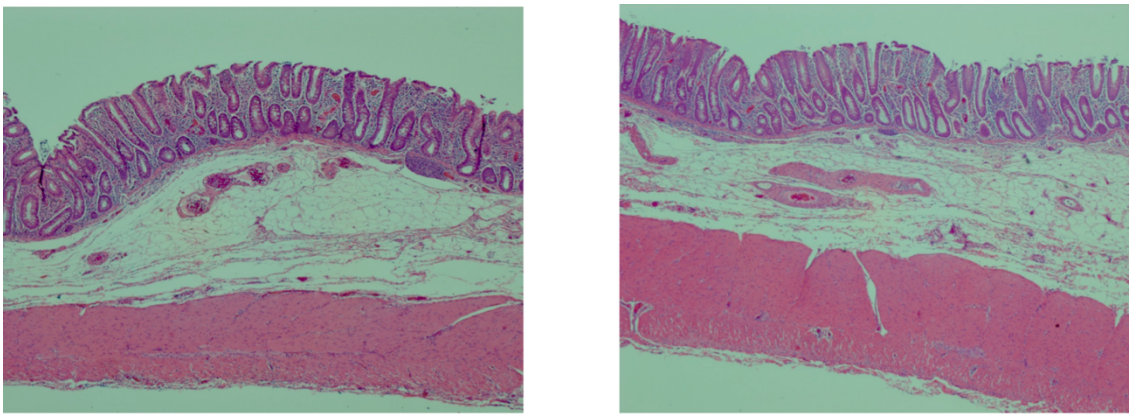

(A) Non-stimulated site (B) Stimulated site

Figure 3.12: Representative samples of micrographs showing H&E stained proximal colon tissues (4X) from direct colon electric stimulation and non-stimulated sites of the same pig.

At the end of the experiment, the proximal colon tissue was examined for damage in 2 pigs. H&E staining of the stimulated (under the electrodes) and the adjacent non-stimulated tissues showed no histological change (see Figure 3.11).

3.2.4.2 Abdominal vagus nerve stimulation: celiac branch

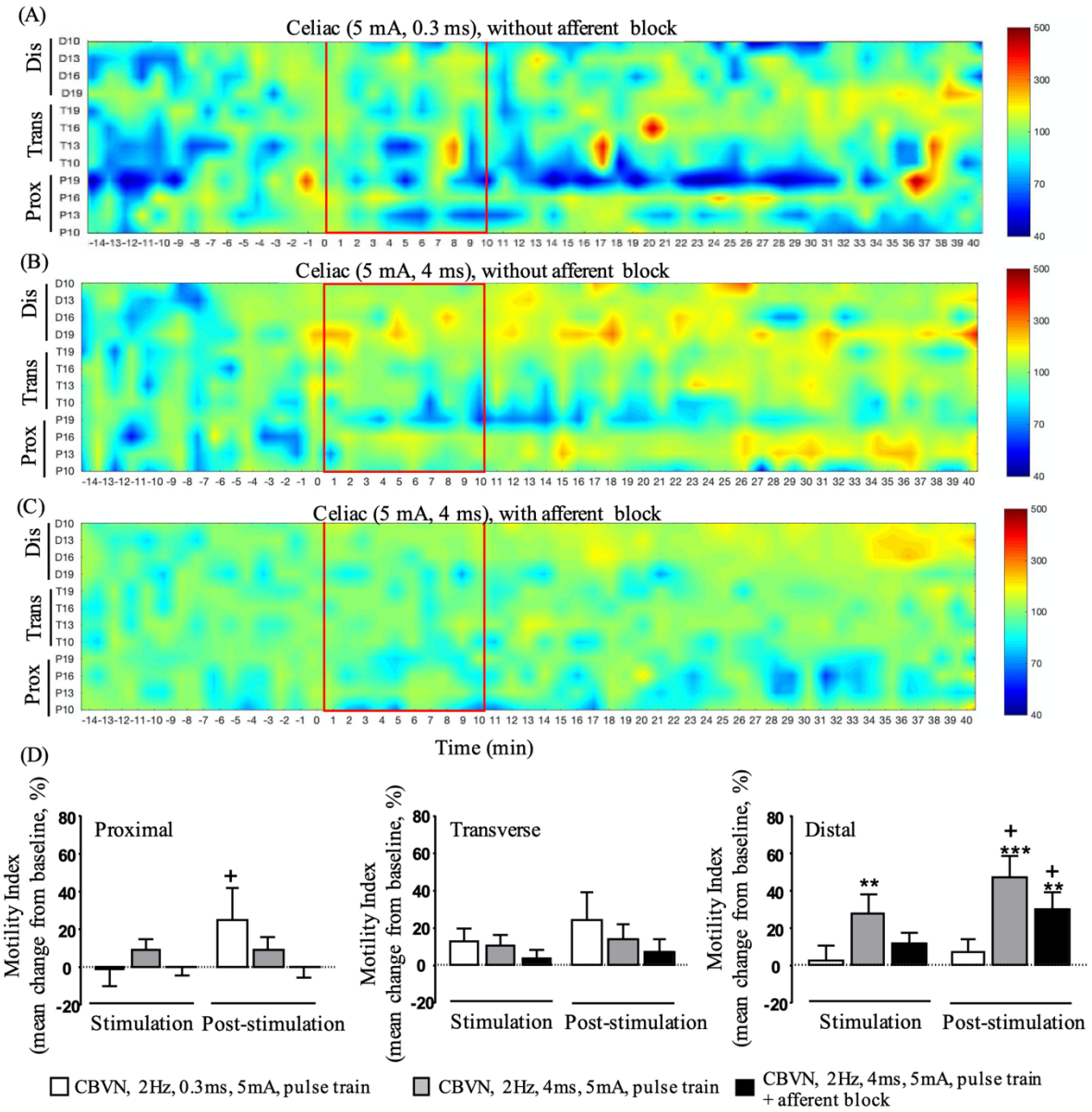

Figure 3.13: Influence of different protocols of electrical stimulation of the abdominal vagus nerve, celiac branch on colonic motility in anesthetized pigs.

Pressure map of (A) pulse train, 2 Hz, 0.3 ms, 5 mA, 10 min, without anodal block; (B) pulse train, 2 Hz, 4 ms, 5 mA, 10 min, without anodal block; (C) pulse train, 2 Hz, 4 ms, 5 mA, 10 min, with afferent anodal block 200 Hz, 0.1 ms, 2 mA. Channels represent the position of the different

manometry probes in the different colonic parts. Traces show the baseline response (15 min), stimulation (15 min), and post-stimulation (30 min) periods. Data are mean ± SEM of recordings from n = 7-14 pigs. (D) Motility index changes (mean change from baseline %) in response to celiac branch vagus nerve stimulation (2 Hz, 5 mA) at a pulse width of 0.3 ms (white bars), 4 ms (gray bars), and 4 ms with the afferent anodal block (black bars), during the stimulation (15 min) and post-stimulation (30 min) in proximal, transverse, and distal (n = 7-14) regions. Data are mean ± SEM, Wilcoxon paired, or Mann-Whitney unpaired t-tests, *P < .05, **P < .01 vs baseline, $^{+}$P < .05, $^{++}$P<0.01 vs stimulation in respective groups

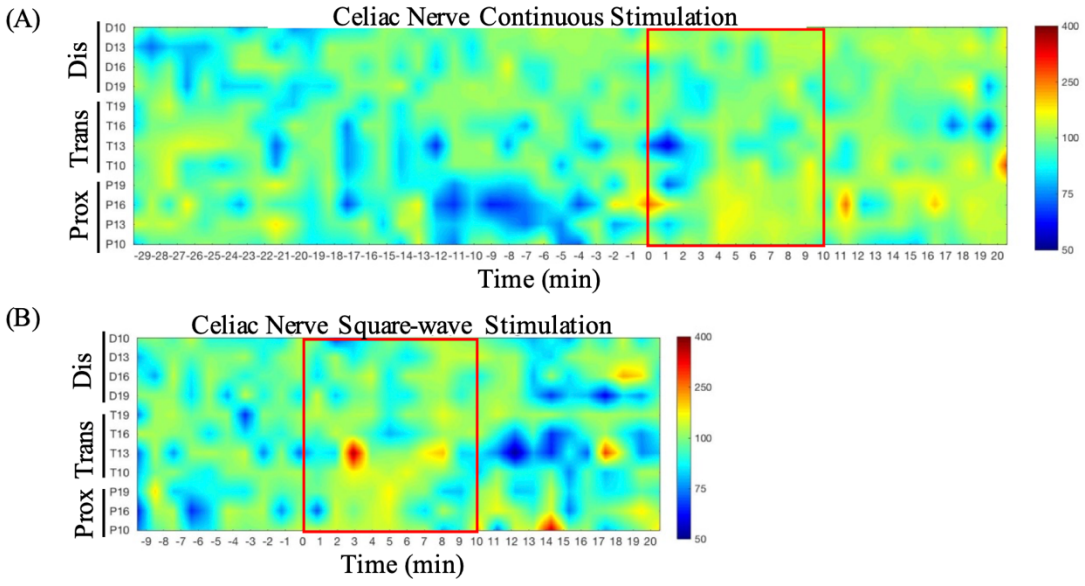

Figure 3.14: Influence of different protocols of electrical stimulation of the abdominal vagus nerve, celiac branch on pig colonic motility.

(A) continuous pulse train stimulation without anodal block; B) square-wave stimulation without anodal block. Data are mean ± SEM of recordings from n=7 pigs.

The stimulation of the CBVN using a pulse train protocol induced a pancolonic motor response in anesthetized pigs that was more intense and widespread with the long pulse width (4ms) (Figure 3.12 (B)) than short pulse width (0.3ms) (Figure 3.12 (A)). The continuous and square-wave protocols were not as efficient as the pulse train protocol in producing motility changes (Figure 3.13). The concomitant blockade of afferent fibers using an anodal afferent block attenuated the pancolonic activation in all regions (Figure 3.12 (C)). The CBVN electrical stimulation induced pancolonic stimulation, and its attenuation in the presence of afferent block is also reflected in the colonic motility index, expressed as AUC, particularly in the proximal and distal colon (Figure 3.12 (D)).

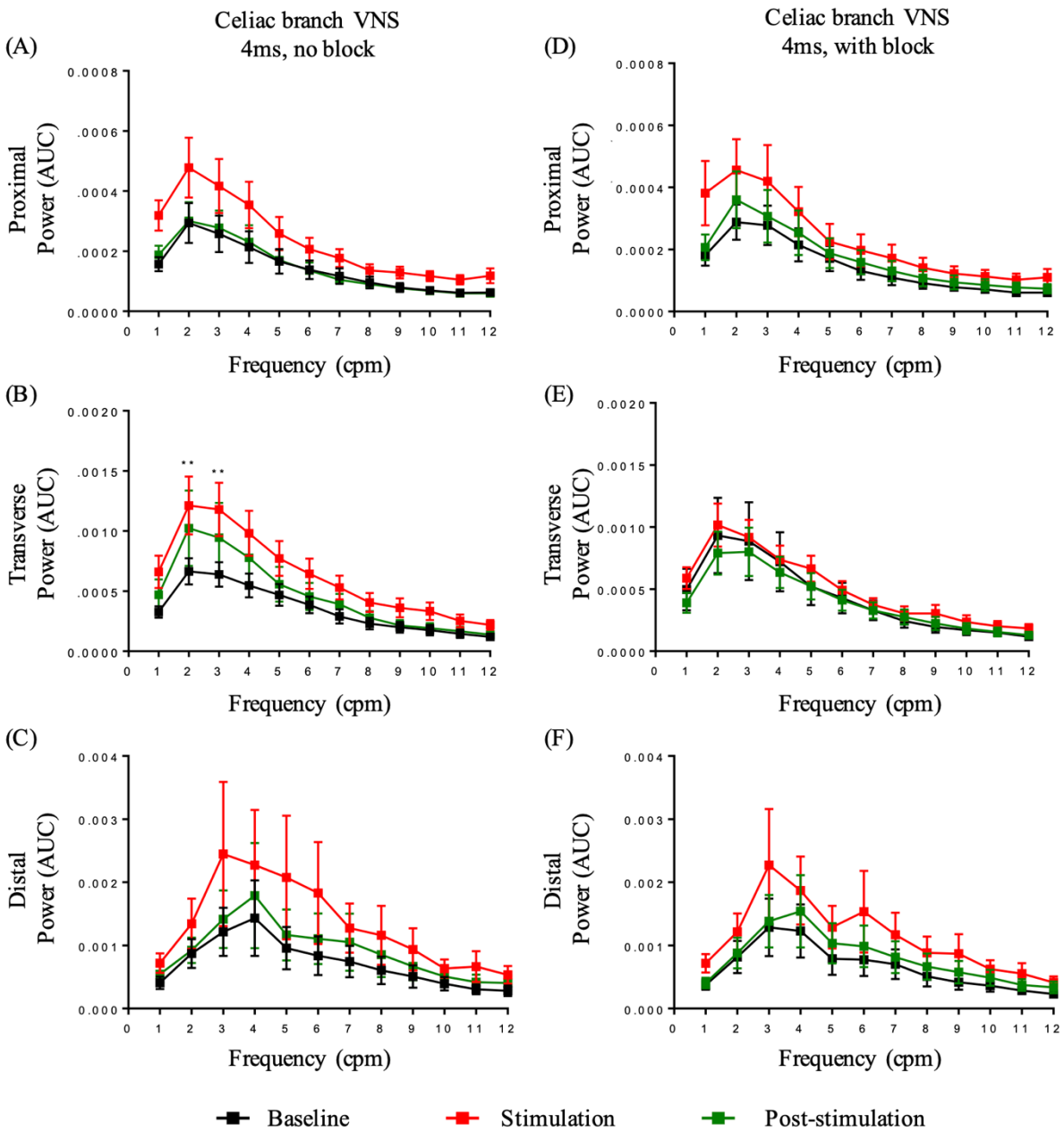

Figure 3.15: Influence of celiac branch abdominal vagus nerve stimulation with or without afferent anodal block on regional colonic frequency power spectrum in anesthetized pigs.

Frequency power spectrum analysis of the colonic motility in response to celiac branch vagus nerve stimulation (2 Hz, 5 mA) at a pulse width of 4 ms alone or with the afferent anodal block at baseline (30 min), during the stimulation (15 min) and post-stimulation (30 min) in proximal,

transverse and distal (n = 7-14) regions. Data are mean ± SEM, Wilcoxon paired or Mann- Whitney unpaired t-tests, **P < .01 vs. baseline in respective groups.

Spectral analysis of the colon response to CBVN electrical stimulation (4ms) showed an increase in the power of the dominant frequency (1-6cpm) across the colon in response to stimulation (Figure 3.14 (A)-(C)), with a statistically significant increase in the 2-3cpm frequencies (power data; P<0.01 vs. baseline) in the transverse colon (Figure 3.14 (B)). Following stimulation, the frequency power returned to baseline in the proximal and distal colon but remained elevated in the transverse colon. In the presence of afferent block, the increased frequency power to CBVN electrical stimulation was attenuated mainly in the transverse colon (Figure 3.14 (D)-(F)), in line with the motility index (AUC) and pressure map response to CBVN electrical stimulation with or without afferent block. Video animation of the pressure changes in response to CBVN electrical stimulation showed no consistent propagation for longer distances (supplementary video 5). Instead, pressure waves appear to move back and forth in a short distance (within 10cm).

3.2.4.3 Sacral nerve root electrical stimulation

Stimulation at sacral nerve sites does not alter systemic responses such as blood pressure and heart rate. S1 or S4 electrical pulse train stimulation had little effect on motility, especially compared to S2 stimulation, as shown in Figure 3.15. Therefore, the study focused more on the effects of S2 and S3 stimulation.

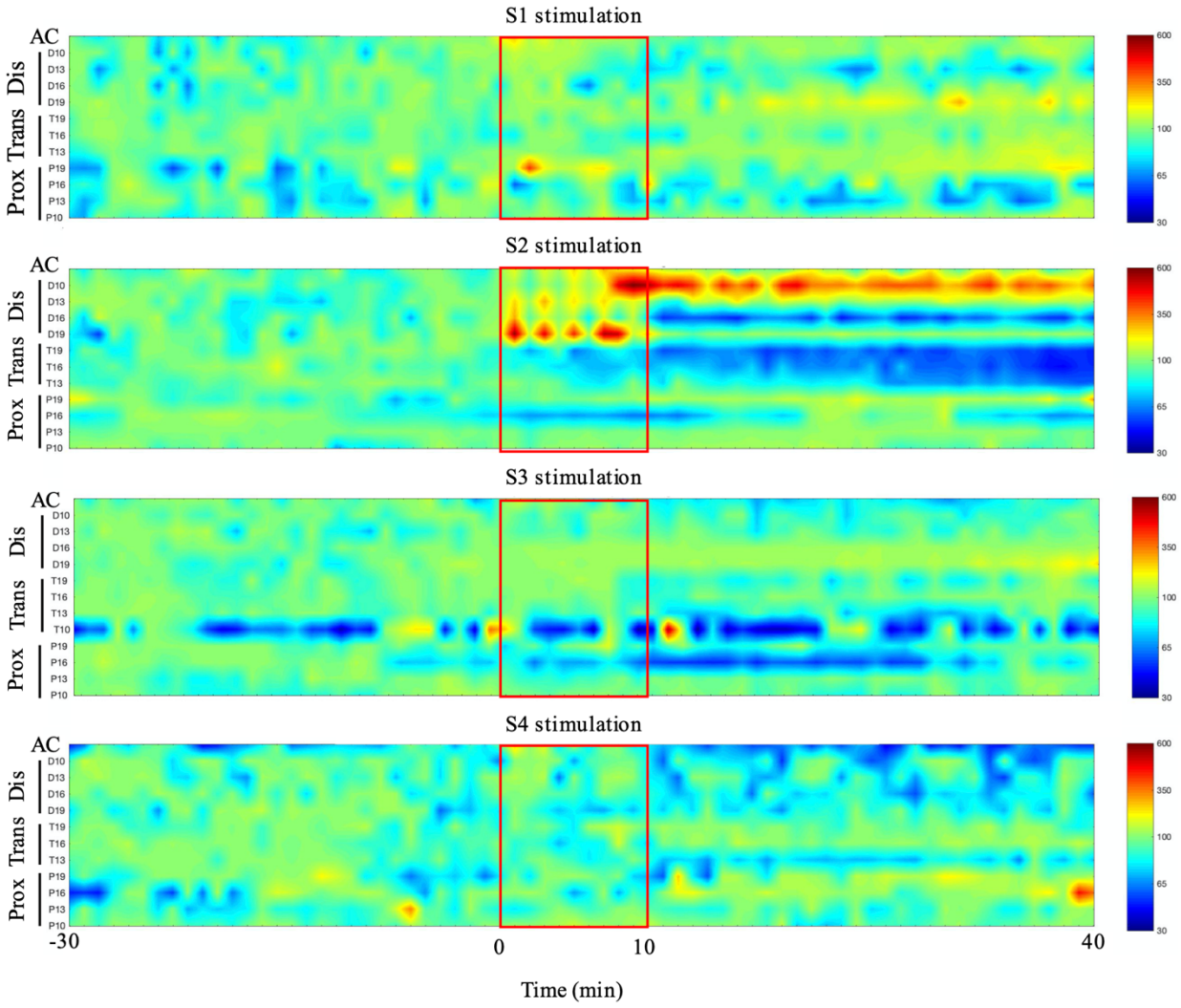

Figure 3.16: Effect of sacral nerve (S1-S4) root pulse train stimulation on the motility of the proximal, transverse and distal colon. Pressure maps representations of recordings before (30 min), during (10 min) and post-stimulation (30 min). (AC = anal canal)

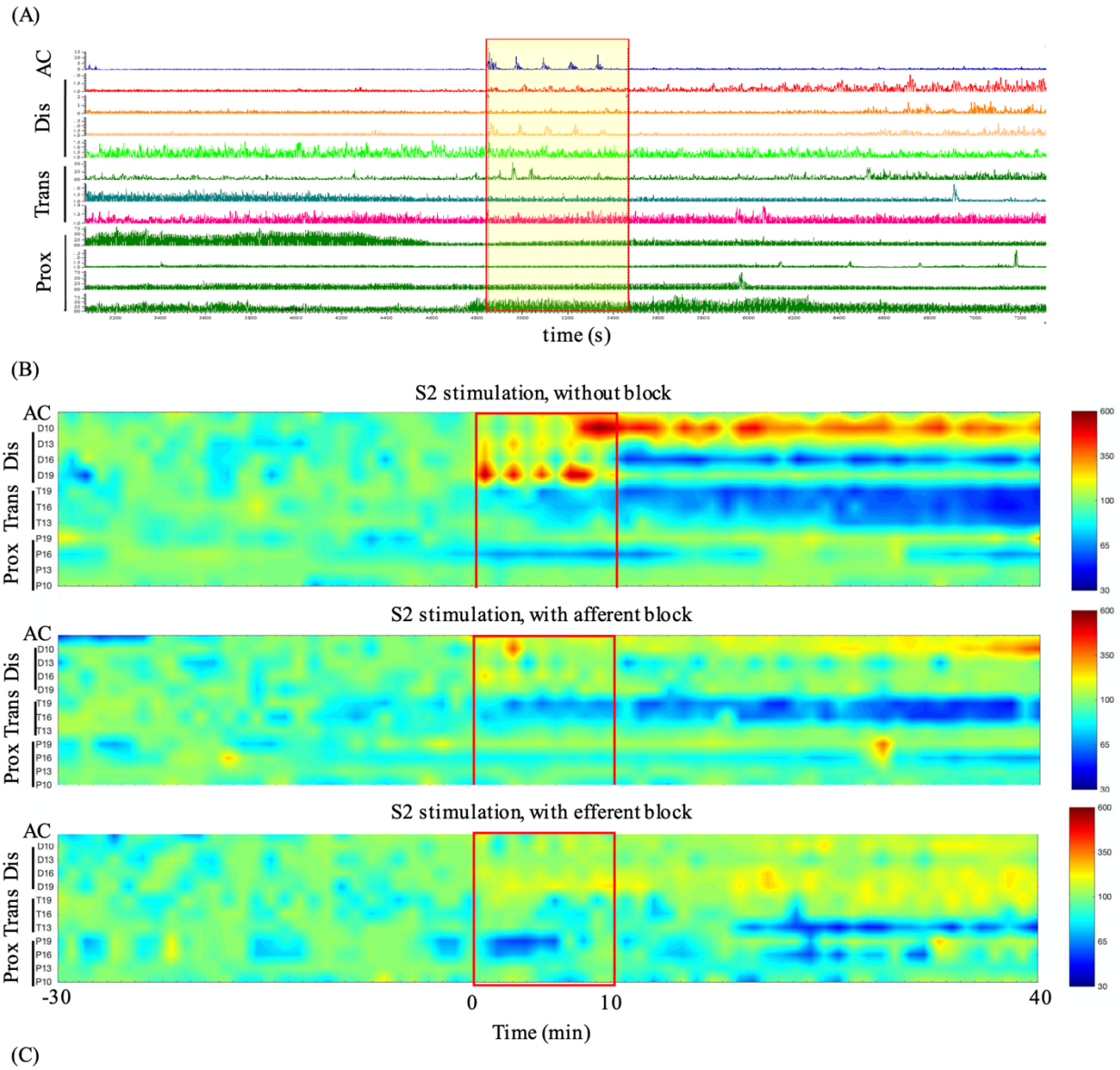
(A)
AC
Dis
Trans
Prox
time (s)
(B)
S2 stimulation, without block
S2 stimulation, with afferent block
S2 stimulation, with efferent block
AC
Dis
Trans
Prox
D10
D13
D16
D19
T19
T16
T13
P19
P16
P13
P10
600
350
100
65
30
-30
0
10
40
Time (min)
(C)
Proximal
Transverse
Distal
AC
AUC/min
400
300
200
100
0
Stim only
AB
EB
Baseline
Stimulation
Post-stimulation
Stim only – S2 stimulation without block
AB – S2 stimulation with afferent block; EB – S2 stimulation with efferent block

Figure 3.17: Effect of sacral nerve (S2) stimulation on the motility of the proximal, transverse and distal colon.

(A) Example of raw trace following sacral spinal root S2 pulse train stimulation, left S2 sacral root, no block. (B) Pressure maps representations of recordings before (30 min), during (10 min) and post-stimulation (30 min). Left sacral spinal root S2 stimulation, 30 Hz, 0.3 ms, 0.5 mA, No block. Left sacral spinal root S2 efferent fibers stimulation, 30 Hz, 0.3 ms, 0.5 mA (i.e., S2 stimulation with a concomitant afferent block, 40kHz, 2V, sinusoidal wave). Left sacral spinal root S2 afferent fibers stimulation, 30 Hz, 0.3 ms, 0.5 mA, (i.e., S2 stimulation with a concomitant efferent block, 40kHz, 2V, sinusoidal wave). Data are mean motility index in % baseline of n=3-4 pigs. AC = anal canal (1 cm from the anus). (C) Quantitative, mean motility index average (% baseline) for the proximal, transverse and distal colon and anal canal response to whole sacral root S2 nerve vs. S2 efferent fiber stimulation (i.e., whole nerve stimulation concomitant with afferent block, 40kHz, 2V, sinusoidal wave) or afferent fiber stimulation (i.e., whole nerve stimulation concomitant with efferent block, 40kHz, 2V, sinusoidal wave). Data are mean ± SEM, n=3-4 probes/colon region recordings from n=3-4 pigs. The baseline is 30 min, stimulation 10 min, and post stimulation 30 min. *$p<0.05$ vs. respective baseline, one-way repeated measure ANOVA and Friedman's post hoc test.

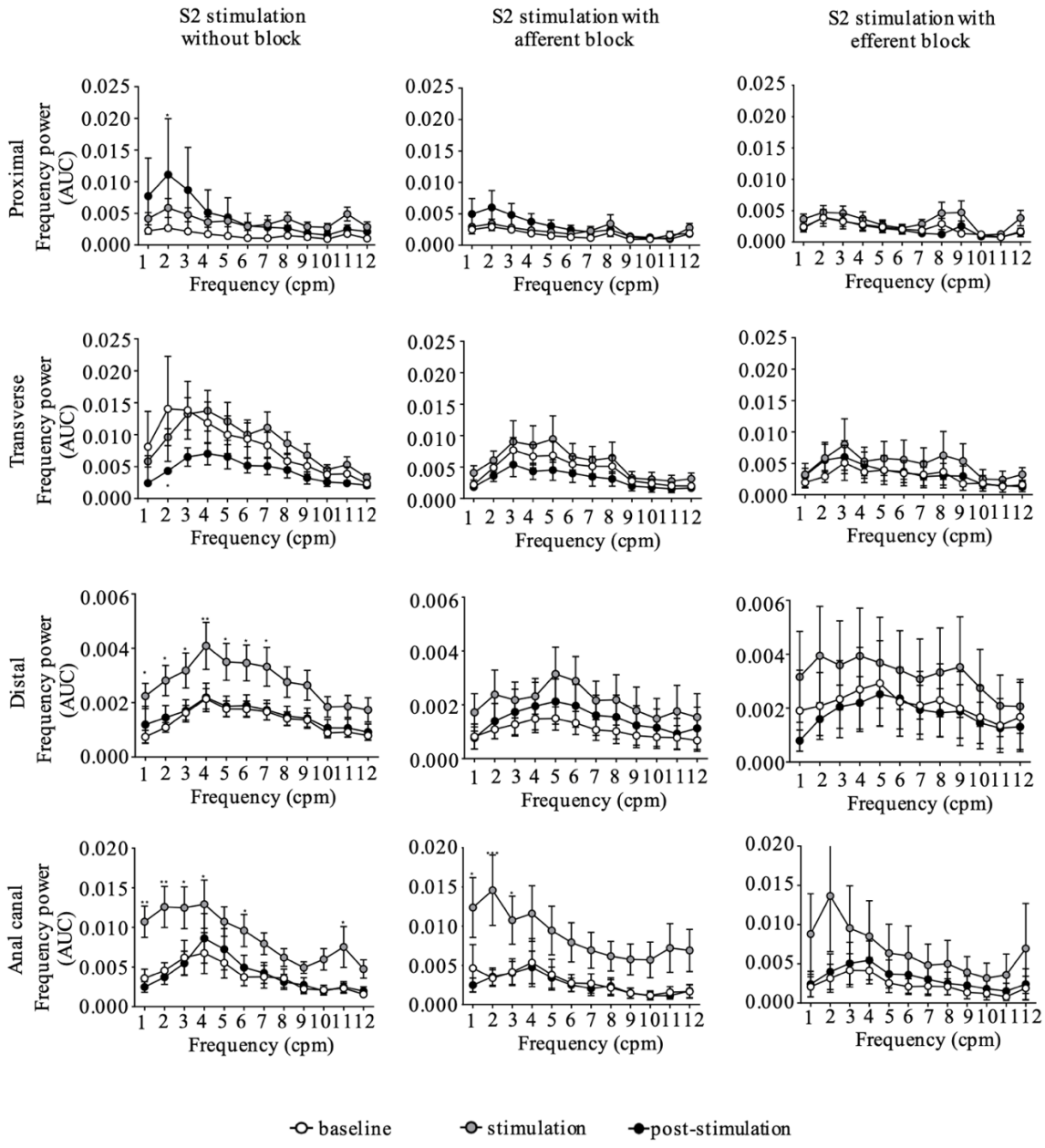

Figure 3.18: Spectral analysis of the colonic motility response to left sacral S2 stimulation with no block, with an afferent or efferent nerve block.

Data show that in the anesthetized pig colon at baseline, the 2-6 cpm frequency band is a dominant power in most of the colon regions monitored. S2 stimulation (30 Hz, 0.3 ms, 0.5 mA) increased power mainly of the dominant frequency at the distal colon and the AC. Afferent block

(40kHz, 2V, sinusoidal wave) reduced the S2-induced increased power of the dominant frequency in the distal colon and the AC. C: Similarly, efferent block (40kHz, 2V, sinusoidal wave) attenuated the S2 stimulation-induced response in the distal colon and the AC. Data are mean ± SEM, average of n=3-4 probes/colon region from 3-10 pigs, *p<0.05, **p<0.01, ***p<0.001 vs respective baseline, RM 2-way ANOVA and Sidak's post hoc test.

S2 electrical stimulation induced a strong and robust activation of motility in the distal colon and anal canal during stimulation and post-stimulation periods while not activating that of the proximal or transverse colon (Figure 3.16). S2 electrical stimulation also increased the power of the whole contraction frequency spectrum in both the distal colon and anal canal during stimulation (Figure 3.17). Video animation (supplementary video 6) shows S2 stimulation caused propagative contractions within the distal 10-19 cm region where the distal sensors are located. In the S2 post-stimulation periods, the transverse colon showed inhibition of motility and a decrease of the frequency power, which did not reach statistical significance. S2 electrical stimulation has little influence on proximal colon motility or contraction frequency spectrum. Afferent block attenuated the distal colon motility index, pressure heat map and the dominant frequency power increase induced by S2 stimulation, which suggests the role of afferent fibers in the S2 stimulation-induced distal colon response. However, the afferent block didn't cause too many changes in the S2 stimulation induced anal canal activation and transverse colon inhibition. On the other hand, the S2 induced increased motility index and increased power of dominant frequency in both the distal colon and anal canal were attenuated by the concomitant efferent block indicating the role of efferent nerve fibers activation in the distal colon and anal canal responses. The S2 induced

inhibition in the transverse colon during the post-stimulation period was also attenuated by the efferent block (Figure 3.16 (B), (C) and Figure 3.17).

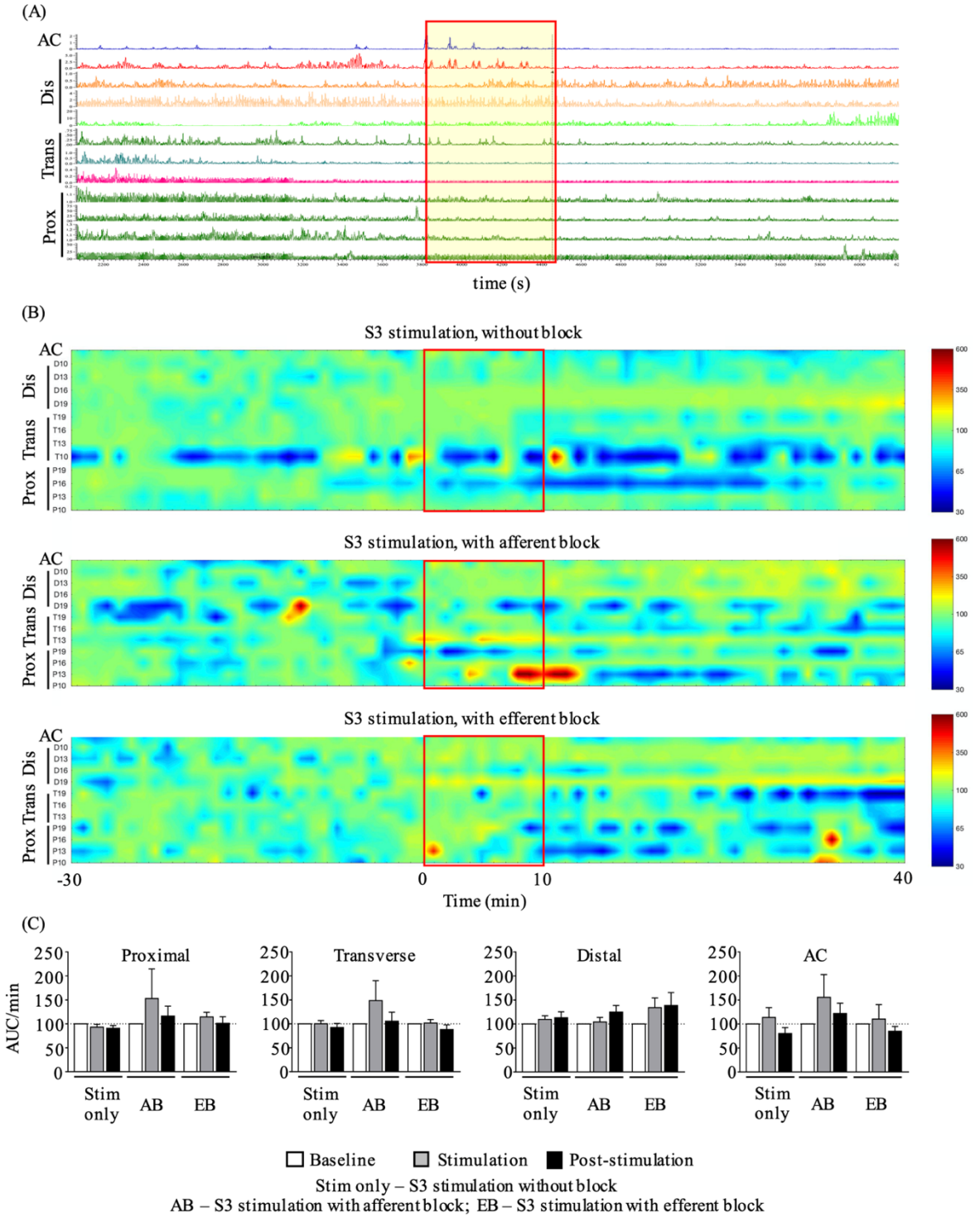

Figure 3.19: Effect of sacral nerve (S3) stimulation on the motility of the proximal, transverse and distal colon.

(A) Example of raw trace following sacral spinal root S3 stimulation short pulse width 30 Hz, 0.3 ms, 0.5 mA, left S3 sacral root, no block. (B) Pressure maps representations of recordings before (30 min), during (10 min) and post-stimulation (30 min). Left sacral spinal S3 nerve root stimulation, 30 Hz, 0.3 ms, 0.5 mA, No block. Left sacral spinal root S3 efferent fibers stimulation, 30 Hz, 0.3 ms, 0.5 mA (S3 stimulation with a concomitant afferent block, 40kHz, 2V, sinusoidal wave). Left sacral spinal root S3 afferent fibers stimulation, 30 Hz, 0.3 ms, 0.5 mA, (S3 stimulation with a concomitant efferent block, 40kHz, 2V, sinusoidal wave). Data are mean motility index in % baseline of n=3-10 pigs. (C) Quantitative, mean motility index average (% baseline) for the proximal, transverse and distal colon and anal canal response to whole sacral root S3 nerve vs. S3 efferent fiber stimulation (i.e., whole nerve stimulation concomitant with afferent block, 40kHz, 2V, sinusoidal wave) or afferent fiber stimulation (i.e., whole nerve stimulation concomitant with efferent block, 40kHz, 2V, sinusoidal wave). Data are mean ± SEM, n=3-4 probes/region recordings from each of n=3-10 pigs. Baseline is 30 min, stimulation 10 min, post stimulation 30 min.

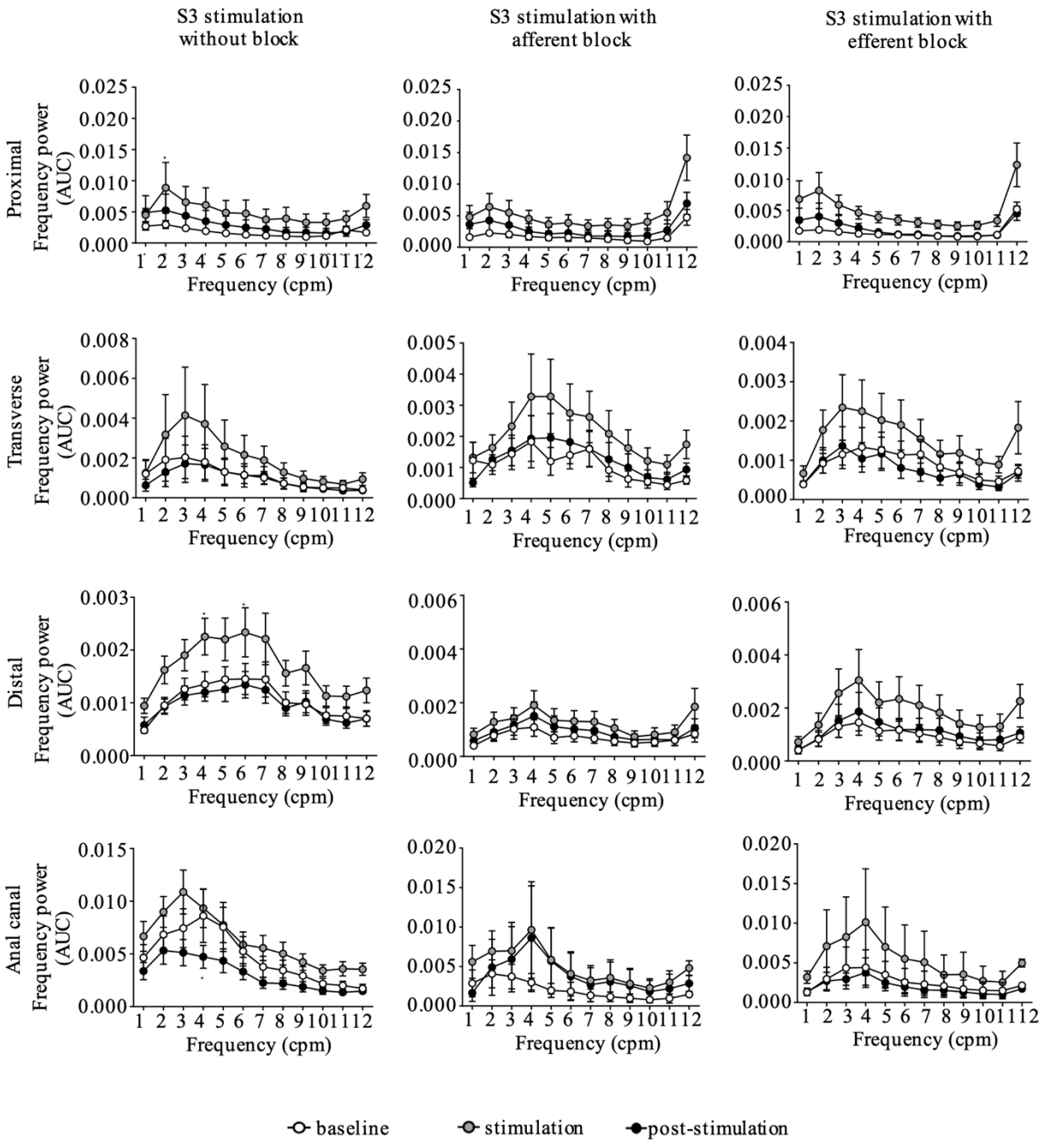

Figure 3.20: Spectral analysis of the colonic motility response to left sacral S3 stimulation with no block, with an afferent or efferent nerve block.

S3 stimulation (30 Hz, 0.3 ms, 0.5 mA) increased power mainly of the dominant frequency at the distal colon. Afferent block (40kHz, 2V, sinusoidal wave) reduced the S3-induced increased

power of the dominant frequency in the distal colon and the AC. Similarly, efferent block (40kHz, 2V, sinusoidal wave) attenuated the S3 stimulation-induced response in the distal colon. Data are mean ± SEM, average of n=3-4 probes/colon region from 3-10 pigs, *$p<0.05$, vs. respective baseline, RM 2-way ANOVA and Sidak's post hoc test.

S3 electrical stimulation, while causing anal canal contraction in about half of the pigs studied, as shown in one example of the raw trace (Figure 3.18(A)), did not cause significant motility index changes (Figure 3.18 (B) and (C)). However, S3 stimulation caused a moderate increase in the power of the dominant frequency domain in the distal colon that was attenuated by afferent and efferent blocks (Figure 3.19). Probes at proximal colon and transverse colon showed variable activation and inhibition of motility in response to the S3 stimulation with or without block. The power of the dominant frequency domain in the transverse colon was increased by the S3 stimulation, which was not attenuated by afferent or efferent block. Those increased powers dropped back to baseline level after the stimulation.

3.2.4.4 Thoracolumbar nerve root electrical stimulation

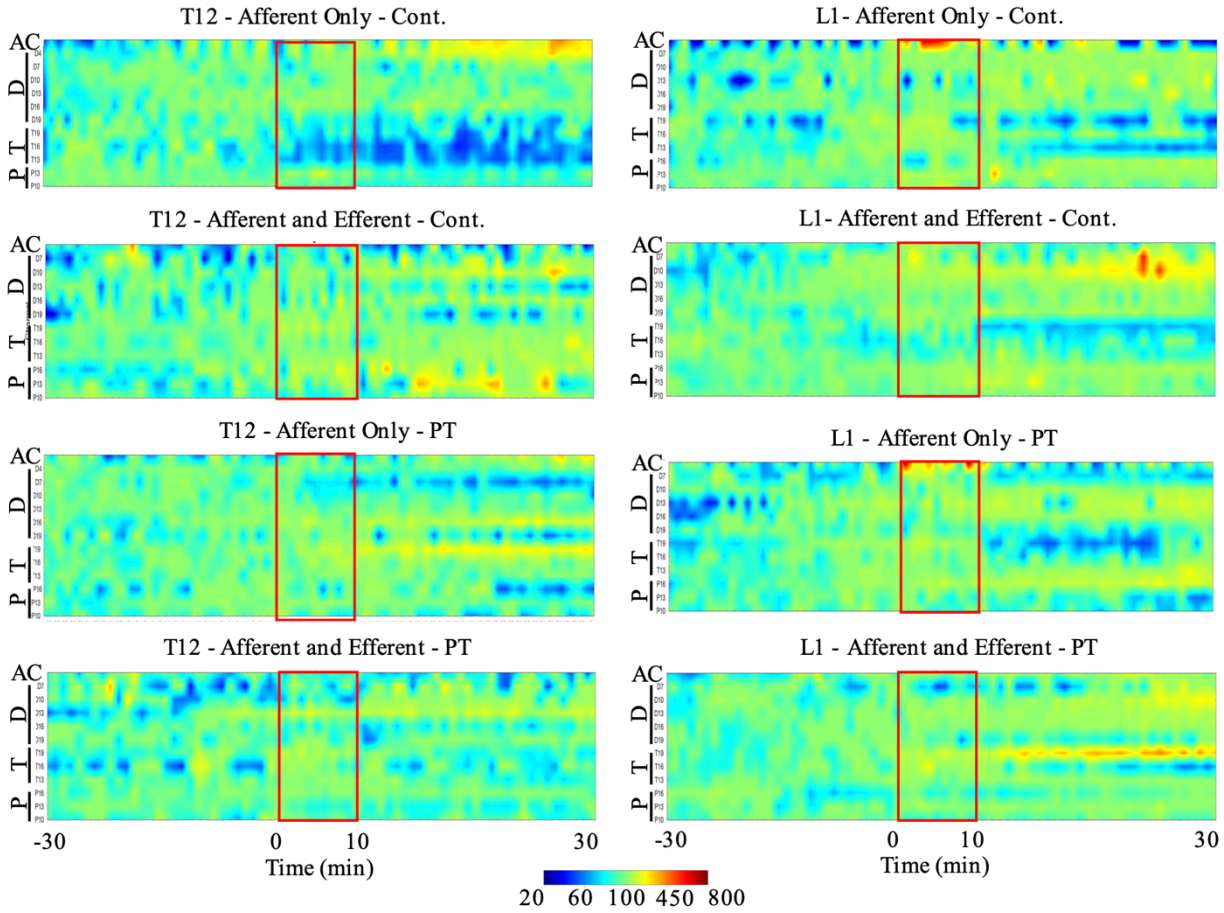

Figure 3.21: Effect of thoracolumbar spinal nerve root stimulation on the motility of proximal, transverse and distal: Pressure maps representations of recordings at baseline (30 min), during (10 min) and post-stimulation (30 min).

The left panels show right T12 spinal nerve stimulation, while the right panels show right L1 spinal nerve root stimulation. Stimulations were made at 10 or 30 Hz (0.3ms, 5mA) with a continuous (cont.) or pulse-train (PT) wave form. The site of stimulation was either at the dorsal root (proximal to the respective dorsal root ganglion), labeled as afferent stimulation or after the dorsal and ventral roots merge (distal to dorsal root ganglion), labeled as afferent and efferent stimulation. Stimulations at 10 vs. 30 Hz and cont. vs. PT waves result is moderate but differential

colon region motility modulation. For instance, afferent stimulation at T12 (10Hz, cont.) causes inhibition of the proximal and transverse colon contractility while moderately increasing contractility at the most distal and anal canal (AC) during and post stimulation periods. Data are mean area under the curve of contraction (AUC) in % baseline of n = 2-4 pigs. AC = anal canal probe, P = proximal probes, T = transverse probes and D = distal probes.

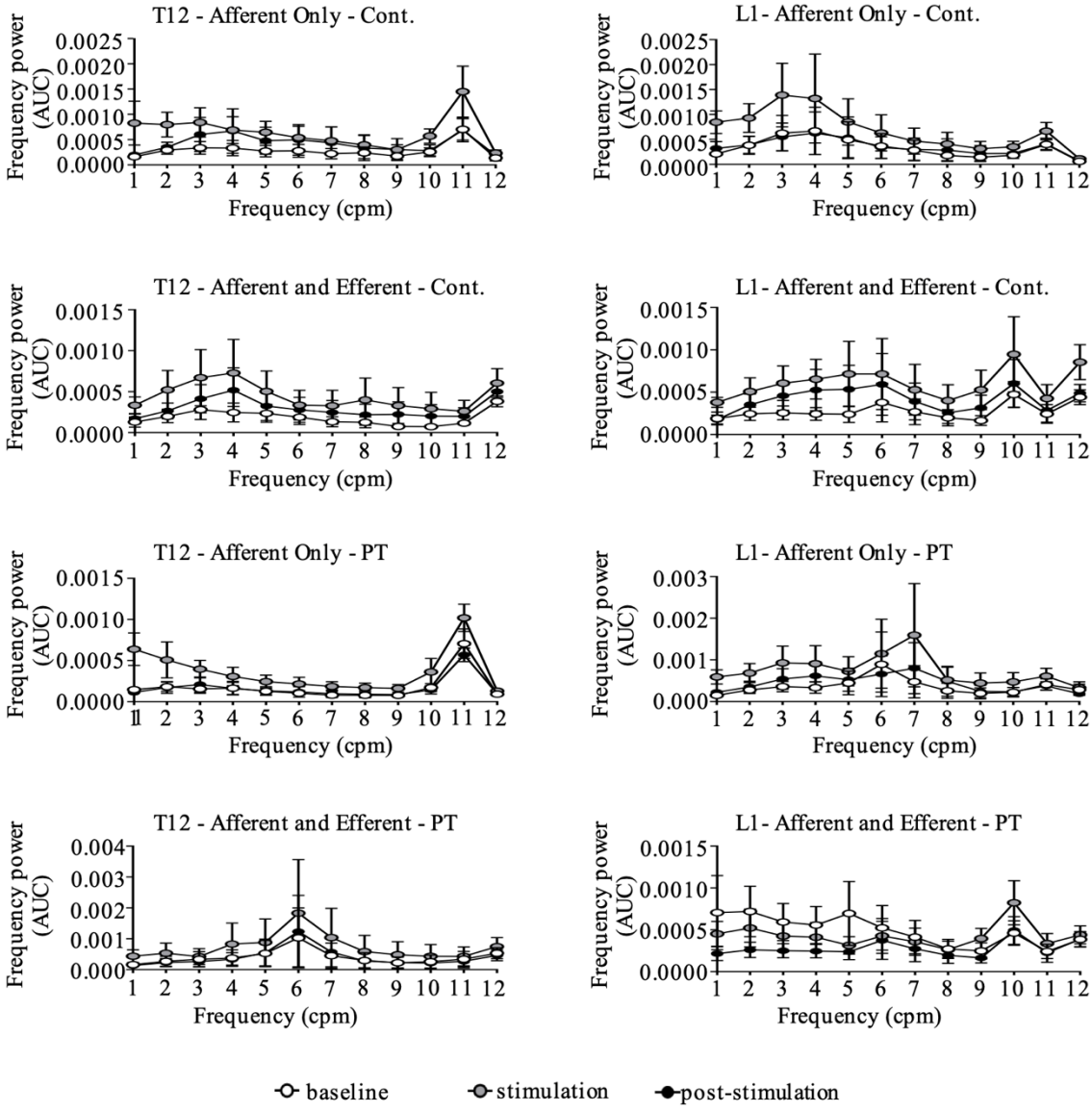

Figure 3.22: Frequency power spectrum analysis of the proximal colonic motility in response T12 (left panels) or L1 (right panels) thoracolumbar spinal roots stimulation (continuous or pulse train wave).

No significant influence of the thoracolumbar nerve roots electrical stimulation with different stimulation parameters on the proximal colon motility frequency band. Data are mean area under the curve of contraction (AUC) in % baseline of n=2-4 pigs.

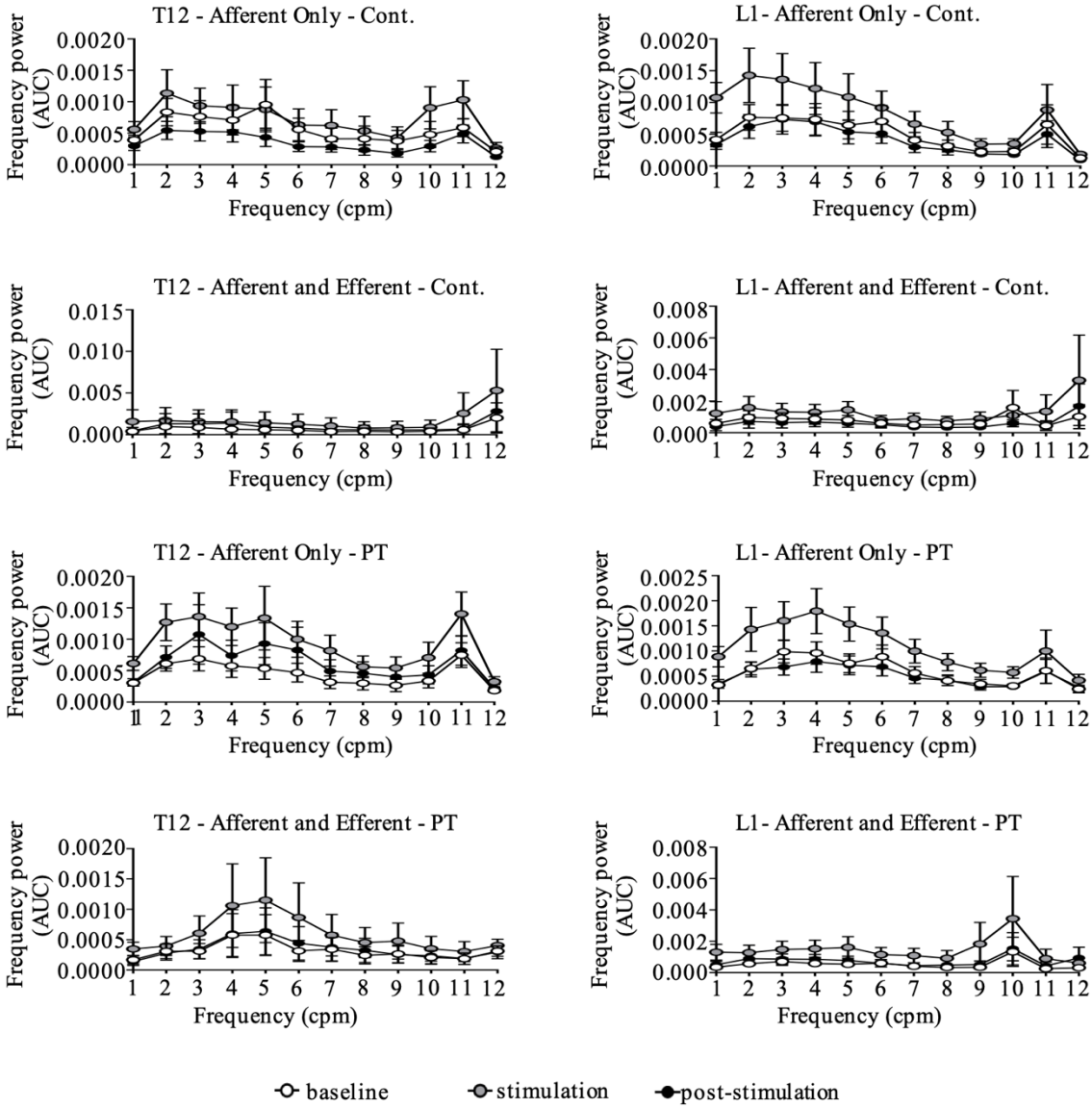

Figure 3.23: Frequency power spectrum analysis of the transverse colonic motility in response T12 (left panels) or L1 (right panels) thoracolumbar spinal roots stimulation (continuous or pulse train wave respectively).

No significant influence of the thoracolumbar nerve roots electrical stimulation with different stimulation parameters on the transverse colon motility frequency band. Data are mean area under the curve of contraction (AUC) in % baseline of n=2-4 pigs.

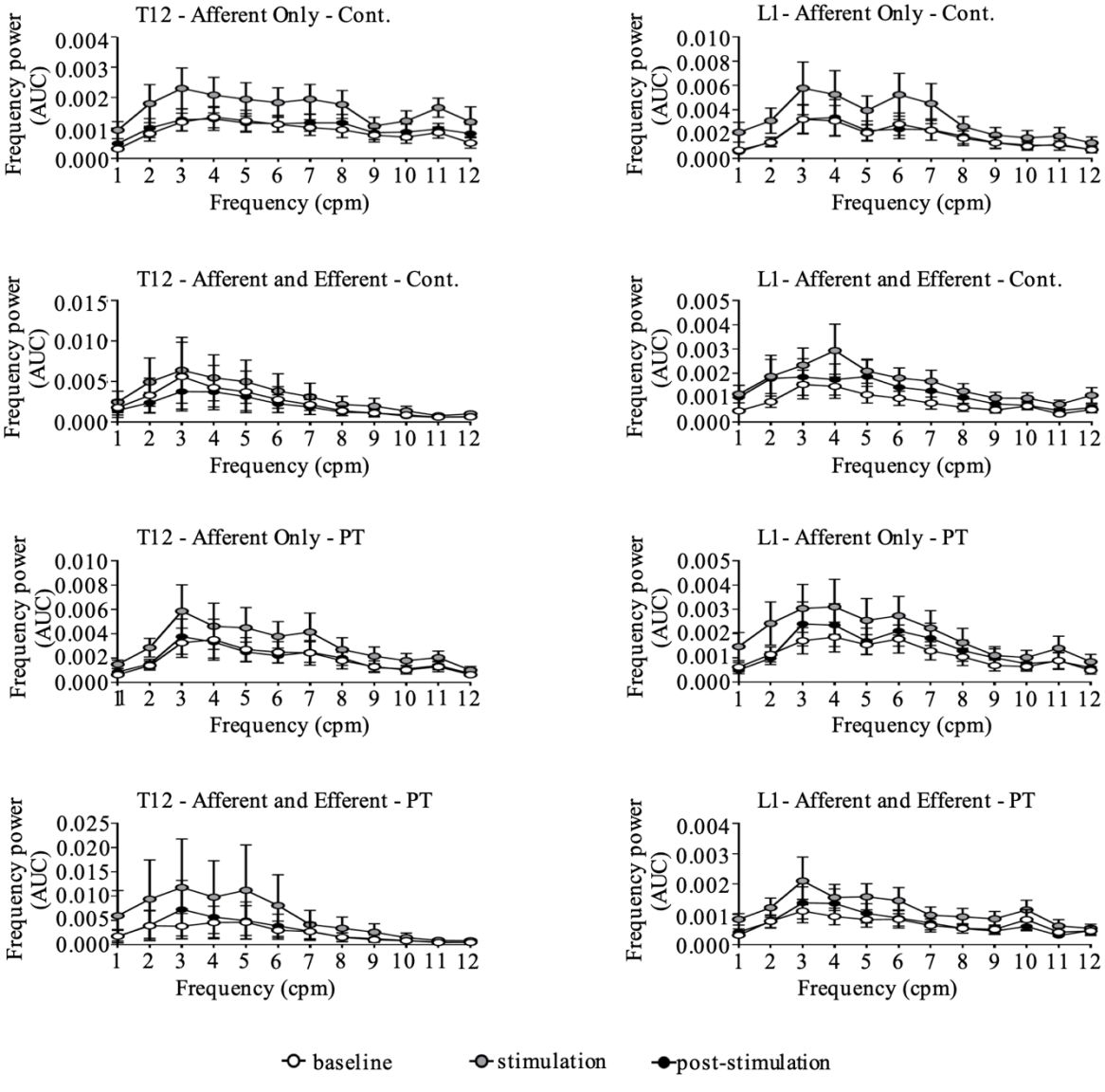

Figure 3.24: Frequency power spectrum analysis of the distal colonic motility in response T12 (left panels) or L1 (right panels) thoracolumbar spinal roots stimulation (continuous or pulse train wave respectively).

No significant influence of the thoracolumbar nerve roots electrical stimulation with different stimulation parameters on the distal colon motility frequency band. Data are mean area under the curve of contraction (AUC) in % baseline of n=2-4 pigs.

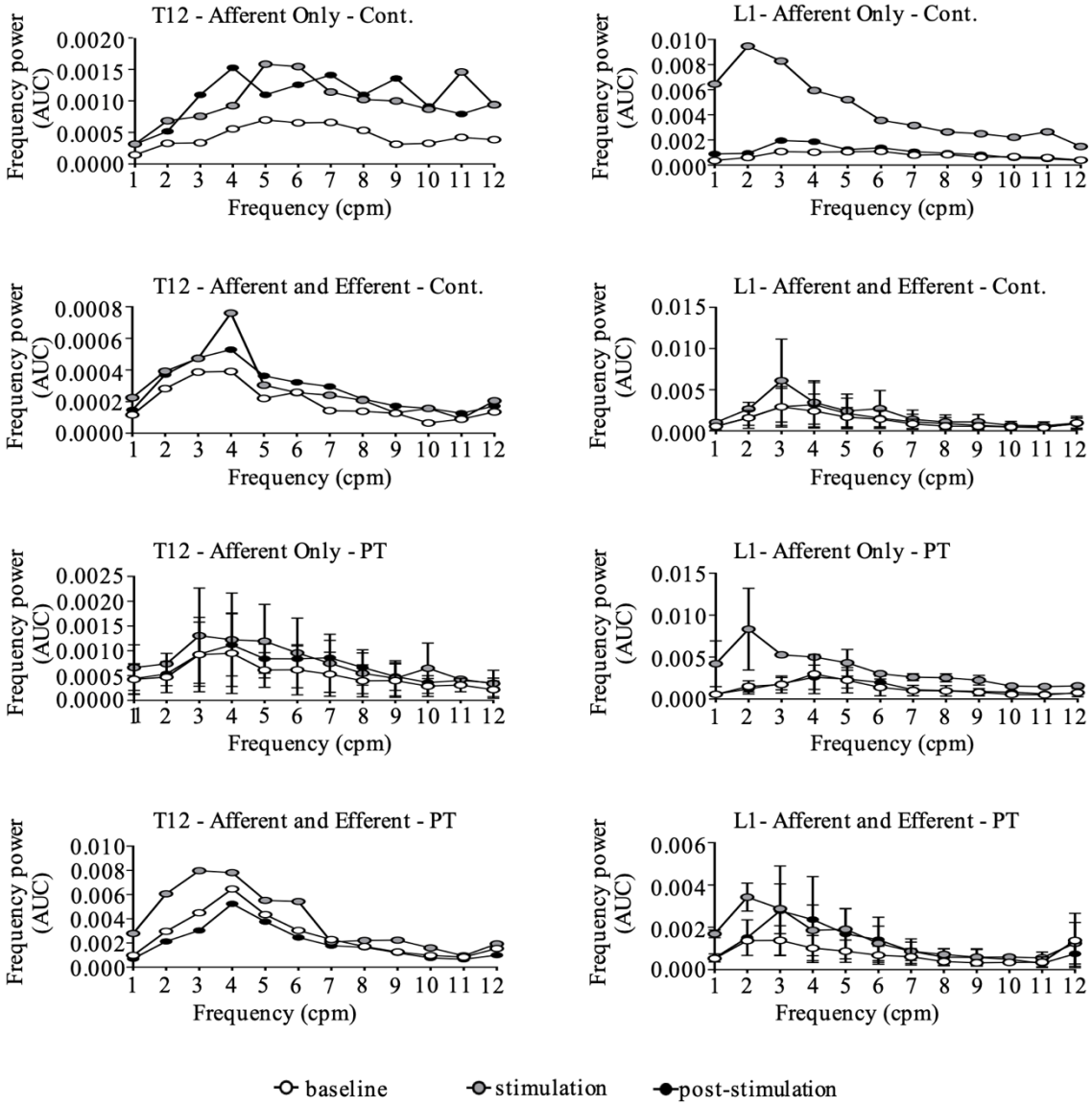

Figure 3.25: Frequency power spectrum analysis of the anal canal motility in response T12 (left panels) or L1 (right panels) thoracolumbar spinal roots stimulation (continuous or pulse train wave respectively).

No significant influence of the thoracolumbar nerve roots electrical stimulation with different stimulation parameters on the anal canal motility frequency band. Data are mean area under the curve of contraction (AUC) in % baseline of n=2-4 pigs.

Thoracolumbar nerve (T12 and L1, afferent only or both afferent and efferent) stimulation (continuous 10Hz, 0.3ms, 0.5mA square wave stimuli or 2Hz, 0.3ms, 0.5mA pulse train with 30Hz, 3 pulses per train) has an only moderate effect on the motility of different colonic regions as shown by pressure heat maps (Figure 3.20). Stimulations at different protocols resulted in differential colon region motility modulation. For instance, afferent stimulation at T12 (10Hz, cont.) causes inhibition of the proximal and transverse colon contractility while moderately increasing contractility at the most distal and anal canal (AC) during and post stimulation periods. The frequency spectral analysis results are in line with the motility changes that there are no significant differences in the power of dominant contraction frequencies (Figure 3.21 - Figure 3.24).

3.2.5 Discussion

In this thesis, the influence of different electrical stimulation modalities applied directly on the colonic tissue or different nerves on colonic motility was mapped in an anesthetized porcine model. The studies provide, for the first time, the functional (motility) sphere of influence of different colon/nerve electrical stimulation on the colonic segments (proximal colon, transverse colon, distal colon) and spectral analysis of colonic motility in the anesthetized pig.

One of the features of the anesthetized pig colon contractile response to local stimulation, when observed visually, is that proximal colon and transverse colon stimulation-induced ring-like circular contraction (supplementary video 2), while distal colon stimulation response was primarily longitudinal and appeared as a shrinking of the colon wall (supplementary video 3). The ring/circular contraction response in the proximal colon and transverse colon is likely to be due to the higher number of gap junctions between circular than longitudinal muscle cells [135], [148] and hence the strong circumferential electrical coupling of intestinal smooth muscle cells [109]. Likewise, the distal colon characteristic longitudinal contraction suggests a stronger electric coupling among the longitudinal than the circular muscle cells and/or the regional heterogeneity of circular vs. longitudinal smooth muscle responsiveness to neurohormonal stimuli as reported in humans [149].

Another salient feature of anesthetized pig colon motility is the occurrence of a wide range of contraction frequency bands (0 - 12cpm) and repetitive phasic pressure events in the 0-12cpm frequency range, with a dominant frequency band of 1-6cpm. The colon is generally considered to have three different types of phasic contractions in various species [106], [108], [109], short duration (0-2s), long duration (10-20s), and high amplitude propagating contractions/giant contractions. Although the relative proportion of short vs. long duration phasic contractions cannot be ascertained in the present study, both short and long duration contractions are observed in the recordings as evidenced in the raw traces. The observed 0-12cpm frequency band corresponds to the reported irregularly appearing short duration phasic contraction frequency in the human colon [109] and to the short duration spike burst frequency (9-12/min) or colonic slow wave frequency in ambulating pigs [106]. On the other hand, the 1-6cpm motor patterns are likely to be analogous to that of the human colon cyclic propagating motor pattern, with a frequency of 2-6cpm, described

in a recent consensus statement on terminology and definitions of colon motility [150]. Similarly, in a preliminary chronically prepared study in pigs, a 2-4cpm frequency band is reported to represent over 50% of all contractile activities [151]. These and the currently observed 1-6cpm dominant band in the colon are likely to be the main feature of colonic motility across species, although the colon, unlike the stomach and small intestine, can have multiple frequency components [152], [153].

Direct electrical pulse train sequential stimulation of two sites (1.5cm apart) of the uncleansed colon at 10Hz, 2ms, 15mA primarily stimulated contraction on and near the stimulated site (12-15cm) but also caused delayed responses (inhibition or stimulation) albeit moderately at distant colonic regions (proximal colon, transverse colon, and distal colon) as evidenced by luminal pressure changes. The relatively longer pulse width stimulation used in the present study (2ms) is in line with the long time constant of intrinsic myoelectric activity of smooth muscle cells [93]. The lack of clear and long-distance propagative contractions in response to direct proximal colon electrical stimulation may be due to the surgical and anesthesia-related ileus. The long luminal distance between the different colonic regions makes it also less likely to capture propagative contractions to such distant regions under the experimental conditions used. On the other hand, the presently observed motility response at distant colonic regions to direct colon electrical stimulation could be due to colo-colic reflex involving the enteric nervous system. In addition, the proximal stimulation site may be devoid of colon pacemakers/hot-spots, described in the human colon as sites responsive to electrical stimulation with propagative contractions [154]. Similar to our observations, however, a recent report on cats indicates that direct proximal colon stimulation is mainly affecting proximal motility [155]. It is to note that no histological damage was observed in either colonic region in response to this electrical stimulation protocol (Figure 3.11).

The anesthetized pig colon displayed also anterograde and retrograde short duration propagation (see example in supplementary video 4). A similar back and forth propagation is reported in the human cyclic motor patterns in the colon [156] and the cecum-proximal colon of pigs [157]. However, it is possible that random contractions and relaxations occur proximal and distal to different sensors' positions that give the impression of short-distance propagation. Further studies on the actual distance and direction of propagation are needed. High amplitude propagating contractions were not recorded in the present study, which is likely due to the general anesthesia [109] and the surgical manipulation [158], both known to cause ileus. The propulsive contraction observed in prior pig distal colon studies could be the result of the combination of multiple sequential stimulations (8 sites at 2cm intervals) and the colon cleansing preparation, itself known to affect colon motility [159]–[161].

Interestingly, the spectral analysis of colonic contractile response to direct colon tissue stimulation causes a general increase in the power of the 0-12cpm frequency band bust, especially of the 1-6cpm frequency band. These data point to the possible differential modulation of power by neuromodulation. There is evidence that patients with bowel dysfunction such as slow transit constipation lack meal-induced cyclic motor pattern (1-6cpm) in the colon [156]. The present data showing the modulation of dominant frequency band motor pattern by electrical stimulation may have relevance in treating some motility-related bowel dysfunctions. However, additional characterization of the differential modulation of frequency band will be critical to understanding the complex functions of the colon, including the possible mechanisms behind the ability of the colon to differentially expel gas, liquid, and solid luminal contents.

In contrast to the direct colon tissue stimulation, which produced an immediate response restricted locally to the segment being stimulated, stimulation of the CBVN (2Hz, 0.3ms or 4ms

and 5mA, pulse train) caused a pancolonic increase in the motility index across the colonic regions. The motility response to short pulse width stimulation was weaker than the one observed width the longer pulse width. This indicates that the use of the long pulse width with the current parameter used (2Hz, 5mA) produces a stronger stimulation. In addition, vagal nerve stimulation caused an overall increase in the power of the 0-12cpm frequency band across the colon but especially of the 1-6cpm band in the transverse colon. In view of the inconsistent report on the extent of colonic innervation by the vagus nerve [162]–[164], the pancolonic motility response observed in the present study is of significance. This shows that the functional sphere of influence of the vagus on the pig colon is larger (extending to the distal colon) than the reported structural evidence of vagal innervation in other species, mainly limited to the cecum and proximal colon [106]–[109], [135], [165]. Interestingly, the effect of CBVN electrical stimulation on motility index as well as the increased power of the 1-6cpm band is reduced when CBVN afferents are blocked using concurrent afferent nerve block. CBVN stimulation in the current study is done unilaterally (the posterior abdominal vagus). Thus, stimulation of the CBVN activates both afferent and efferent fibers, the former modulating central circuits that feedback to the target organ through both dorsal and ventral vagi. These data suggest that the CBVN electrical stimulation recruited the central vagal network regulating colonic motility [166] and that vagal afferents contribute to the pancolonic response to vagal stimulation. In line with this assumption, vagal stimulation frequencies as low as 1Hz are reported to activate the central vagal network and reduce seizures [141], supporting that our stimulation parameters can indeed recruit central vagal circuits.

The vagal nerve stimulation frequency used in the current study is in the lower frequency range than that used to reduce epileptic seizures in humans (20-30Hz) [167], [168]. However, vagal stimulation at wider ranges (2-300Hz) is shown to induce electroencephalogic desynchronization

[169]. Studies show that different electrical vagal stimulation patterns have different effects. For instance, chorda tympani in cats or vagus nerve stimulation in ferrets, using a burst pattern compared to a continuous stimulation pattern, causes higher magnitude of saliva and vasoactive intestinal peptide secretion by the salivary gland in cats and of higher gastric acid secretion and contraction response in ferrets, for the same total number of stimuli [170], [171]. In line with this, we show that pulse train vagal nerve stimulation causes a more robust pancolonic motility than a continuous or square-wave stimulation pattern (with the same pulse width and amplitude). This is likely to be due to the pulse train stimulation pattern inducing temporal summation at the colonic plexi to release more excitatory neurotransmitters, as shown in cats [172]. Thus, although the frequency of stimulation used in the current study is low, the combination of the pulse train stimulation pattern with the relatively longer pulse width (0.3-4ms) and higher intensity (5mA) stimulation used is likely to account for the recruitment of both afferent and efferent vagal fibers.

Spinal sacral nerves represent one of the parasympathetic arms of the extrinsic innervation of the colon. It is shown to modulate bladder and anal functions both in humans and non-human animals[145], [146], [173]–[175]. In our work, we have mapped the functional response (colon motility) to a wide range of acute sacral nerves stimulation parameters in anesthetized and surgically prepared pigs. Specifically, we demonstrated that S2 electrical stimulation induced strong activation in the distal colon and anal canal with smaller current intensity compared to the direct colon stimulation and vagus nerve stimulation. The similar increase in rectum pressure, with a weak correlation to the symptomatic changes, has been observed in other sacral nerve stimulation for the treatment of both fecal incontinence and rectal constipation [104], [176], [177]. The comparison between stimulation only, stimulation with afferent block or efferent block indicates that S2 electrical stimulation involves the participation of the central neural network for the distal

colon and efferent fibers in the anal canal, which may be a possible explanation for the efficacy of the sacral nerve stimulation on both fecal incontinence and rectal constipation [178].

The difficulties in accessing the thoracolumbar nerves (T12 and L1) and the high risk of damaging the nerves limited the number of pigs that were studied with thoracolumbar electrical stimulation protocols (n = 2-4). Therefore, we can only show a very preliminary result regarding the effects of thoracolumbar nerves on colon motility. In addition, we would like to point out that the peaks at the 10-11 cpm band shown in the T12 afferent continuous square wave stimulation and pulse train stimulation may not be the real colonic activity since it was overwhelmed by the high power of the ventilator/breathing frequency as explained previously. Overall the fact that we do not see many activations as in the sacral or the vagus stimulation is because most of the nerve fibers from the thoracolumbar are said to be sympathetic and hence more of inhibitory to the gut especially affecting the transverse colon [179]–[181], which is indicated in our results. However, it is premature to make any conclusive idea based on the limited number of pigs (n=2-4). In general, the lack of clear effects on the colon, coupled with the relatively high risk of hemorrhage in accessing these nerves compared to the vagus nerve or sacral nerves, suggest that the T12 or L1 spinal nerves may not be the best targets to modulate colonic motility, although the effect of stimulating these nerves in the awake state and on transit has not yet been determined.

The larger functional response to electrical stimulation of CBVN than the direct colon or sacral nerve stimulation suggests that while the latter two simulations might be used for region-specific modulation, CBVN electrical stimulation can be considered to target most of the colon.

Two different blocking techniques, high frequency blocking and anodal blocking were used in our study regarding the nerve types. High frequency (> 100 Hz, but < 1kHz) electrical stimulation and the less understood kilohertz (>1kHz) stimulation have been both shown to block nerve

activities by depleting neurotransmitters and/or inducing axonal fatigue [182], [183]. In the sacral nerve study, kilohertz (40kHz) sine wave was tested to be most effective for the blocking effects. As for the CBVN study, we evaluated and then adopted the stimuli with a firing frequency of 200Hz and a short stimulus pulse width of 0.1ms (i.e., 10kHz) to block the vagus nerve, which is composed of 80% afferent fibers and 20% efferent fibers. Mathematically the Power Spectrum Density (PSD) of the blocking pulse train at 0.1ms at 200Hz is proportional to a $Sinc$ function, i.e., $Sinc(\pi \times f \times 0.1\text{ms})$ at the frequency resolution of 200Hz. Thus, it covers the frequency spectrum from DC to the first null frequency $= (1/0.1)\text{ms} = 10\text{kHz}$, second null one at 20kHz, etc., at the frequency resolution of 200Hz, which includes multiple frequency components in the kHz range. Previous work also shows that nerve stimulation with 100 to 500Hz and 0.1ms is able to induce fatigue at nerve fiber. As a result, the blocking effect is achieved [184]. We would also like to emphasize that our technique is based on anodal blocking, whose operation theory basis differs from the kilohertz blocking. Nerve membranes show opposite responses to the cathodic and anodic currents. Cathodic stimulation causes depolarization while anodic does hyperpolarization. During the stimulation, if sufficient hyperpolarization is induced by the anodic current, it can block the action potential [182], [184]. We believe it is an afferent block because the pancolonic response caused by CBVN electrical stimulation is reduced when the afferent block is done concurrently with stimulation. In addition, as a clear and immediate test on the effect of 200 Hz as a nerve block, we have tested the effect of 200Hz efferent block on cervical vagus stimulation-induced heart rate change on the same pig. We show that cervical vagus stimulation-induced heart rate decrease was blocked by the efferent nerve block, suggesting that the 200Hz block protocol used on the afferent CBVN electrical stimulation indeed interrupts nerve transmission.

3.2.6 Conclusion

In summary, the study provides the first functional/motility-response-map of the colon to electrical neuromodulation by simultaneous monitoring of the proximal colon, transverse colon, and distal colon regions to direct tissue and different nerve stimulation in the anesthetized pig. The data show that: (a) direct electrical stimulation primarily causes local contraction but also moderately modulates distant colon regions contraction; (b) CBVN electrical stimulation increases contractions across the colon through the recruitment of vagal circuits including afferent mediated central circuitry; (c) the dominant contraction frequency band in basal states in the anesthetized pig colon is 1-6cpm in all colonic regions whose power/magnitude is increased during colon or vagal electrical stimulation; (d) the thoracolumbar (T12 and L1) stimulation has only moderate effect on motility and dominant contraction frequency band of different colonic regions; (e) sacral nerve S2 stimulation induced a strong and robust activation of motility in distal colon and anal canal during stimulation and post-stimulation periods, while causing transverse colon inhibition; (f) sacral nerve S1, S3, or S4 electrical stimulation has little effects on the colonic motility and contraction frequency spectrum in contrast to the S2 electrical stimulation; and (g) spectral analysis of colon motility in health and diseases could have the potential to guide therapies against gut motility disorders. Mapping the motility response of the colon to electroceutical interventions, through simultaneous monitoring of the different regions of the colon, in a model that bears several similarities to humans, provides critical data that can guide translational studies and applications to human patients. The study has limitations in that data are generated in anesthetized pigs that underwent acute abdominal surgery. Thus, animals were under conditions of suppressed colonic motor activity and the actual colonic motility responses to an acute short duration (10-15min)

electrical stimulation of colon tissue or different nerves. It is likely that chronic and longer stimulation may exert different responses and, as such, further investigation in chronic conscious models is warranted. Lastly, given that the studies were performed in male castrated pigs, additional studies taking into account the possible effects of sex differences and the influences of sex hormones on colonic motility and on the colonic responses to neuromodulation are needed.

Taken together, the functional mapping data and the characterization of colonic motility analysis in the anesthetized porcine model reported provides a useful frame of reference that will help guide: (a) future mapping studies in the awake and behaving model and (b) neuromodulation interventions while patients are still under anesthesia (for instance to decrease surgery-induced ileus). As such, the study provides a foundational basis on which to develop safe and effective neuromodulation for patients suffering from intractable colonic motility disorders. Selective stimulation of fascicles within a nerve, such as the vagus, could allow targeting specific functions and avoid off-target effects [185].

3.3 Bio-impedance Method to Monitor Colon Motility

In most of the current gastrointestinal studies, the effectiveness of the technique was assessed mainly via colonic motility evaluation. The conventional way to assess the colonic motility uses a force/pressure transducer. However, there are limitations for a manometry approach, especially in colonic-related studies [186], [187]. The insertion of the probes may cause uncomfortable sensations. Motion artifacts may also interfere with the signals. Also, careful interpretation of the manometry data is required when contractions cause undetectable or very low luminal pressure changes. New techniques have been investigated to overcome these obstacles. For example, a

proof-of-concept flexible piezoelectric device has been proposed for gastrointestinal (GI) motility sensing [188], yet it still faces the challenges of motion artifact. Impedance measurement, with broad categories, is another strategy to monitor GI motility. One of the bio-impedance techniques, placing electrodes on the abdomen and back, is based on the characteristic that impedance variation mainly depends on the changes in gastric volume due to food filling [189]–[193]. By measuring the bio-impedance in the gastric region, gastric motility and gastric emptying can be identified. However, it is more similar to general GI motility monitoring which consists of information from the whole GI sensitive region. Considering the complexity of colonic motility, it is difficult for this method to provide region-specific colonic activity in detail. Another bio-impedance method is based on the tissue impedance variation due to the tissue deformation [7], [194], [195], where a circuit system calculates the tissue impedance by applying a carefully filtered PWM (at 50KHz) voltage to the tissue. The main constraint is to apply a voltage less than 200mV to the tissue in order to prevent the undesired contraction. The impedance is deduced based on the current response extracted via a rectifier. This method involves a tedious computation.

Consequently, in this section, we proposed a novel method to monitor the colonic motility in the porcine model by measuring its bio-impedance. It is an efficient impedance analysis method developed on the Randles Cell Model that has been validated in our prior studies on gastric motility measurements [6], [9], [140].

3.3.1 Bio-impedance measurement

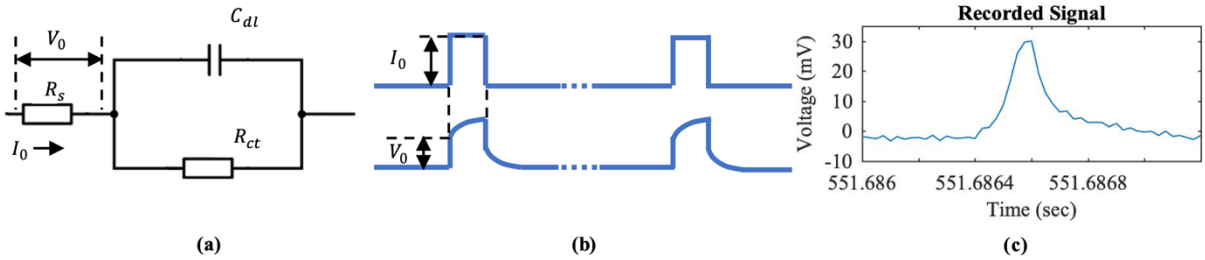

Figure 3.26: (A) Randles Cell Model. (B) Electrode overpotential resulted from a stimulus with small intensity. (C) Representative recorded signals.

The colonic wall bio-impedance changes reflect colonic motility since the tissue impedance changes with the smooth muscle deformation. With the basis of the Randles Cell electrode model (RC-model) [196]–[198], a hardware-efficient bio-impedance method is proposed to monitor GI motility. The Randles cell model of an electrode, as shown in Figure 3.25 (A), includes a tissue solution resistance R_s, a double layer capacitance C_{dl}, and a charge transfer resistance R_{CT}. Note that R_s reflects the colonic muscle deformation measured in our case. By applying electrical stimuli of a series of short square pulses with small intensity into the colon, the response in terms of the RC-model can be obtained from the resulting electrode overpotential (Figure 3.25 (B) and (C)). Therefore, the electrode-tissue impedance can be concurrently extracted by V_0/I_0. The applied stimuli in our study were 200Hz, 0.1ms, 3uA, which had a fundamental tone at 200Hz and harmonics more than 10kHz (1/0.1ms). The RC-model responses were modulated by these high-frequency stimuli; as a result, the low-frequency (<<200Hz) motion artifacts can be filtered through a high-pass filter. It is important to note that the narrow and low intensity pulse must be well below the stimulation threshold charge of the colon according to the strength-duration curve. In our study, the current intensity is low enough (3uA in our case) so that it avoids activating the

colon and directly interferes with the colonic motility. Without involving sophisticated computations, this method provides the bio-impedance information in a broad frequency spectrum. A similar technique has been validated in previous studies [6], [9], [140].

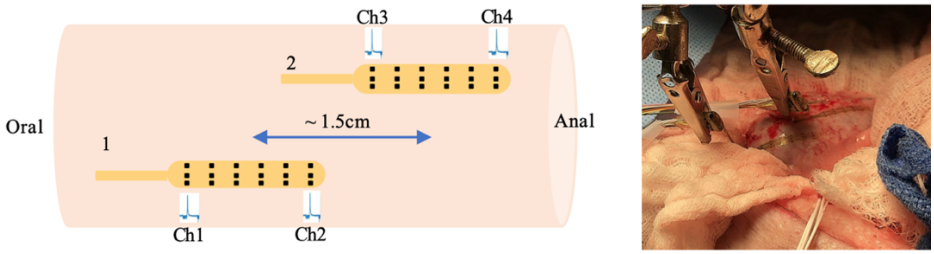

Figure 3.27: Bio-impedance measurement setup.

Each colonic region has two recording electrodes, each containing four recording sites Ch1, Ch2, Ch3, and Ch4. The distance between the first two channels (Ch1-Ch2) and the last two channels (Ch3-Ch4) is 1.5cm, while Ch2 and Ch3 have a distance of 3mm.

The bio-impedance method was tested on direct distal colon stimulation as described in the previous section. To avoid any confusion, "stimulation" in the rest of this section refers to the burst stimulation protocol to activate the direct distal colon. Each colonic region has two planar electrode arrays, each containing four recording sites along the longitudinal axis of the colon (Figure 3.26). In each region, the distance between the first two channels (Ch1-Ch2) and the last two channels (Ch3-Ch4) is 15mm, while Ch2 and Ch3 have a distance of 3mm. The impedance data were recorded with a Plexon system (Plexon Inc., TX) at a sampling frequency of 40kHz for the whole experiment, including three separated intervals - namely baseline, stimulation, and post-stimulation intervals. The bio-impedance analysis is carried out at each interval. Both time-domain analysis and dominant frequency components of the bio-impedance data were done by customized MATLAB codes. Time-domain analysis of the bio-impedance induced by the colonic phasic

activity was first performed. By quantifying the area under the curve of the bio-impedance change per minute, the colonic contractile-induced impedance changes (zAUC) were monitored. Correlation tests were then conducted between zAUC and the aforementioned manometry motility index (pAUC). Then the heatmap image is used to visualize the strength of average zAUC changes and their regional distribution across the colon. Frequency domain components were then compared between "baseline" and "post-stimulation" intervals. It should be noted that during "stimulation" interval, the bio-impedance analysis is intentionally done at the window of 60s OFF time at each protocol cycle in order to avoid the complication of stimulation artifact. However, considering the fact that the frequency resolution ($\Delta f = 1/60sec$) corresponding to the short duration (60s OFF time) is not fine enough for reliably analyzing the responses during "stimulation" interval, accordingly, in this paper, our impedance analysis in frequency domain excludes the data extracted at the "stimulation" intervals.

Considering the data properties and its complexity, the Generalized Estimating Equation (GEE) was used for statistical analysis [199]–[202] on 1) changes of one-minute average impedance, expressed in percentage of baseline data, induced by stimulation; and 2) dominant frequency changes of impedance induced by stimulation. A $P<0.05$ indicates a significant change.

3.3.2 Results

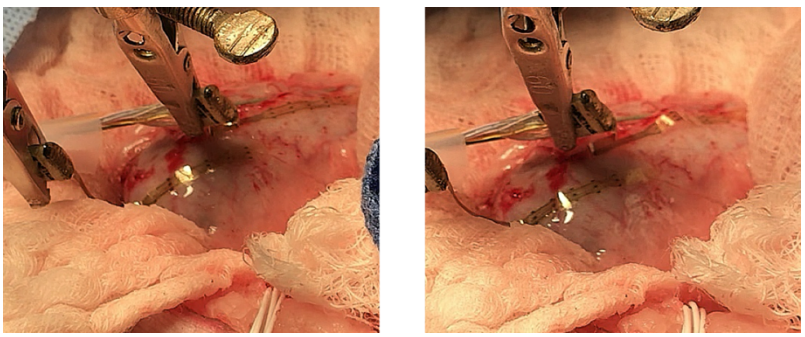

Figure 3.28: Longitudinal contraction of the distal colonic tissue in responses to direct distal colon stimulation. Left: Before stimulation. Right: During stimulation.

As reported in the previous section, Direct colon stimulation did not cause hemodynamic changes. Direct distal colon stimulation resulted in an immediate local longitudinal contraction of the colonic tissue under the stimulation point (Figure 3.27). The manometry results reported that it increased the distal colonic motility during and after the stimulation, while it caused fewer effects on proximal and transverse probes.

3.3.2.1 Bio-impedance changes in the time domain

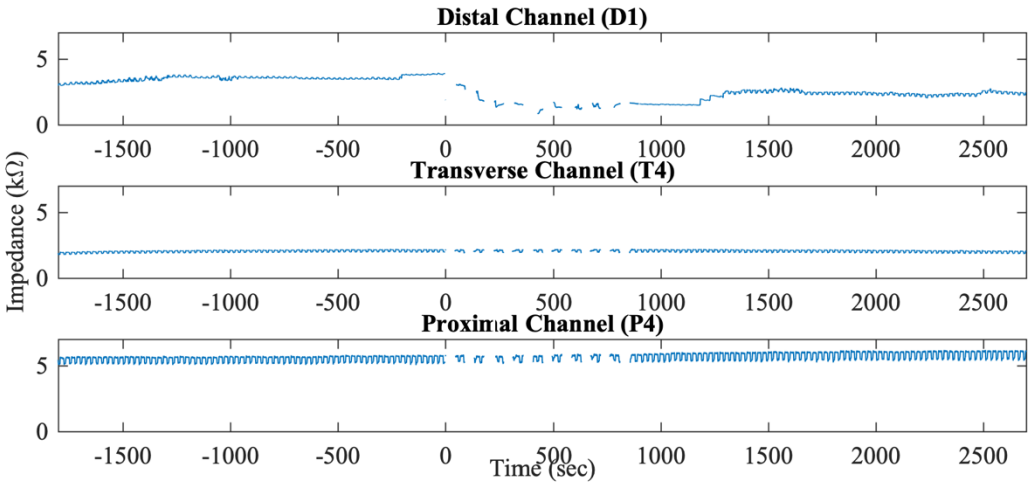

Figure 3.29: Example of different bio-impedance responses in the time domain in proximal (P4), transverse (T4), and distal colon (D1).

Stimulation starts at 0s and ends at 900s. Little or no DC changes in the proximal and transverse colon while large impedance drops in the distal colon during the stimulation and gradually raises after the stimulation.

Table 3.2: Colonic bio-impedance (in % baseline) during direct distal colon stimulation (15 minutes) and post-direct distal colon stimulation (30 minutes) in response to direct distal colon stimulation in anesthetized male Yucatan pigs.

Note: Data are mean ± SD of n as indicated for each channel. Significant changes (*P < 0.05 and **P < 0.01) were observed with respect to baseline impedance (100.00±0.00%).

	n	Stimulation (in % baseline)	Post-stimulation (in %
P1	6	88.49 ± 19.69	93.04 ± 29.11
P2	6	95.18 ± 14.82	92.03 ± 31.06
P3	7	103.47 ± 13.54	103.58 ± 26.62
P4	5	$112.62 \pm 12.44^{**}$	108.10 ± 39.47
T1	6	91.07 ± 10.98	97.13 ± 23.33
T2	6	105.07 ± 9.68	115.41 ± 21.74
T3	4	111.21 ± 48.47	102.21 ± 65.33
T4	4	133.08 ± 35.75	127.96 ± 47.70
D1	6	83.69 ± 22.45	94.90 ± 23.50
D2	5	$61.62 \pm 23.63^{*}$	$57.68 \pm 24.98^{*}$
D3	4	$59.17 \pm 52.66^{*}$	$86.44 \pm 29.86^{**}$
D4	6	97.90 ± 19.91	106.57 ± 18.84

Figure 3.28 show representative bio-impedance responses of distal, transverse, and proximal channels in the time domain. The bio-impedance generally oscillated at around 2-3cpm with additional DC shifts sometimes, of which the DC changes reflect the tonic contractile status. During the baseline periods from -1800s to 0s, the colonic bio-impedance remained stable for all three colonic regions. Corresponding with the activation of the electrodes on the distal colon at 0s, the local contraction occurred underneath the distal channels. The bio-impedance of the distal colonic tissue monitored by those channels decreased significantly. A large impedance drop was observed in most of the distal channels during the 15min stimulation period. Table 3.2 shows the

decreased bio-impedance (percentage of baseline) in all four distal channels, where the changes compared to baseline in both D2 and D3 channels reach statistical significance. After the stimulation, the bio-impedance gradually rises and becomes stable again in the majority of the distal channels. It is of interest that the bio-impedance of the D2 channel kept decreasing during the post-stimulation time. However, unlike the distal channels, the transverse and proximal channels showed variable increase and decrease during and after the stimulation, except for the significant increase in P4 during the stimulation and T2 after the stimulation. The change of DC component in the bio-impedance as a function of time reflected the colonic tissue activity. The colonic tissue contraction causes the decrease of bio-impedance, while the relaxation, on the contrary, causes the increase. This finding is consistent with previous studies [7], [9], [140], [194]. An explanation for this phenomenon is based on the resistance formula such that the contraction shortens the current path and therefore decreases the impedance, while the tissue relaxation actually prolongs the pathway and increases the impedance.

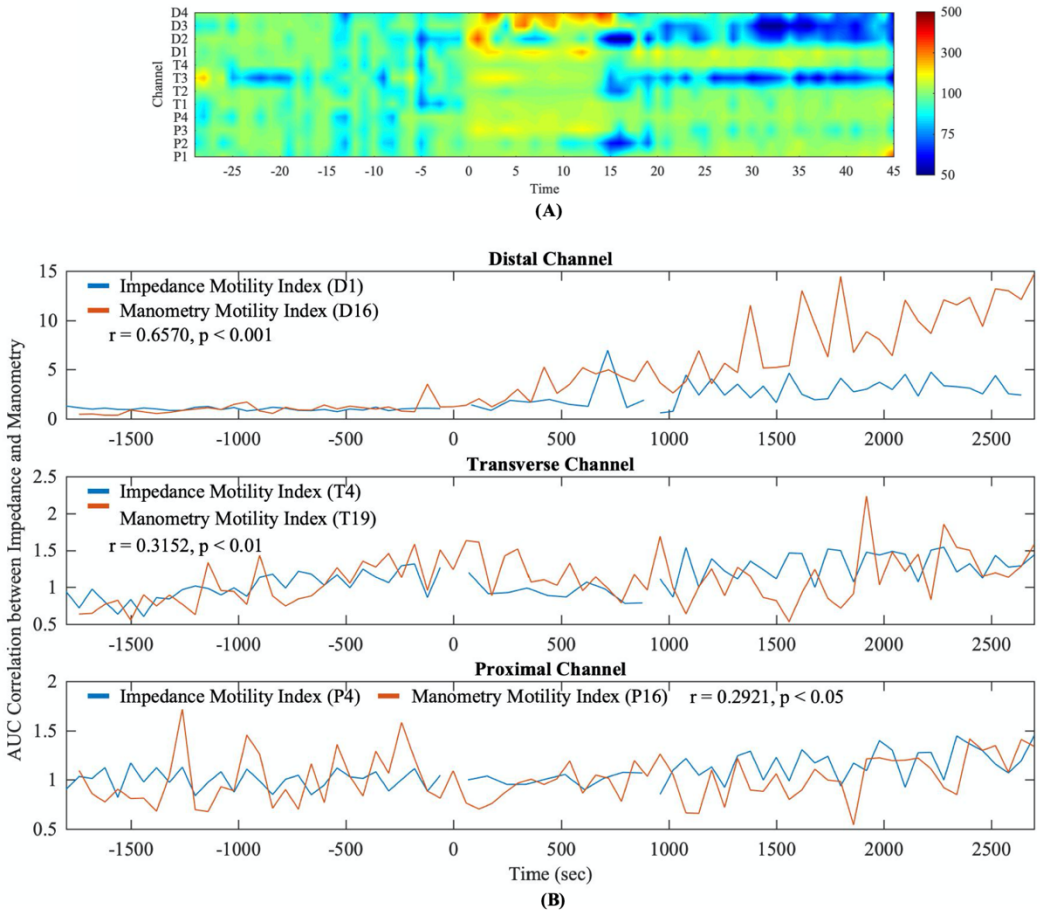

Figure 3.30: (A) Motility heatmap plot of bio-impedance. (B) Representative results of AUC correlation between impedance channel and manometry probe in proximal (P4 & P16), transverse (T4 & T19), and distal colon (D1 & D16). Stimulation starts at 0s and ends at 900s.

As proposed in the previous method section, zAUC reveals the colonic phasic activity-induced bio-impedance. The overall trend, shown in the bio-impedance heatmap (Figure 3.29 (A)), is that the stimulation of the distal colon induced marked impedance changes of the distal colon, followed by fewer impedance changes for the next 30min post-stimulation period. The impedance changes of the proximal and transverse regions were mostly less affected. To further test the correlation between the bio-impedance and manometry, the zAUC and pAUC of each channel/probe were

compared. The results show that there exist high correlations between the manometry probes (P16, T19, D16) and impedance channels (P4, T4, D1) if their deployed positions are physically overlapped, as shown in Figure 3.29 (B), which indicates the bio-impedance method potentially contains the manometry information. However, we are aware of the existence of uncorrelated channels and probes. It is important to note that manometry probes and bio-impedance recording channels employed different spatial resolutions. Consequently, there exist locations where manometry probes and bio-impedance recording channels are not aligned and overlapped in our experiments. As a result, the non-overlapping nature contributes to the un-correlations. These different spatial locations can also explain the differences between the zAUC heatmap and the heatmap in the previously reported manometry. The stimuli caused strong local activation of the recording region, which corresponded to the significant impedance changes. After the stimulation, the recording region gradually relaxed and became less active, while the contractile activity started a short propagation and caused colonic activation in the surrounding area. Therefore, the spatial resolutions with two different modalities may contribute to the differences between current bio-impedance and manometry data.

3.3.2.2 Bio-impedance changes in the frequency domain

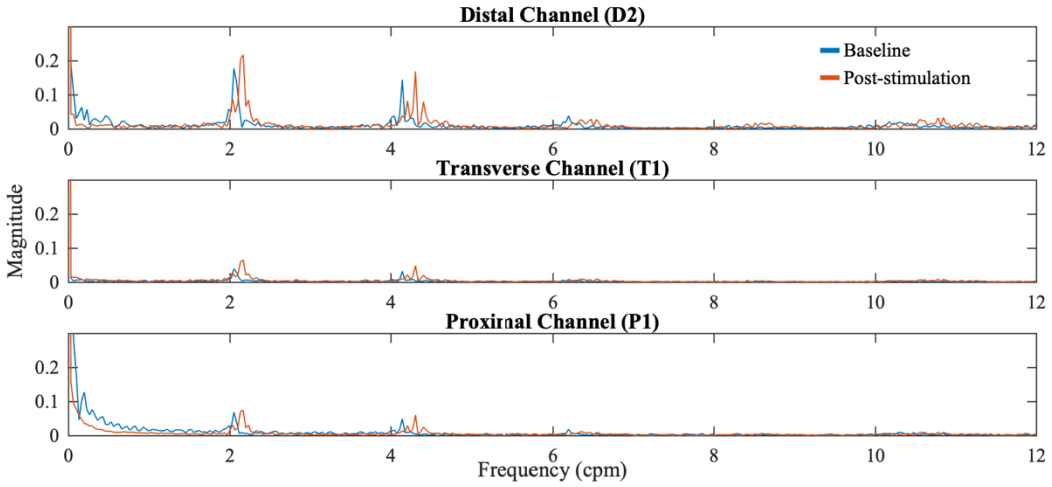

Figure 3.31: Peak frequencies are observed in the majority of the channels. Examples of different bio-impedance responses in the frequency domain in proximal (P1), transverse (T1), and distal colon (D2).

The dominant frequency is in the range of 2-4cpm. Dominant frequency increase significantly ($P<0.05$) after the 15min stimulation is observed in most channels.

Table 3.3: Colonic bio-impedance dominant frequency during baseline and post-direct distal colon stimulation in anesthetized male Yucatan pigs.

Note: Data are mean ± SD of n as indicated for each channel. *P < 0.05, **P < 0.01 and ***P < 0.001 vs baseline.

	Baseline (cpm)	**Post-stimulation (cpm)**
P1	2.2867 ± 0.2921	2.4232 ± 0.2967
P2	2.3054 ± 0.2624	$2.325 \pm 0.1705^{**}$
P3	2.3153 ± 0.2869	$2.3472 \pm 0.1675^{*}$
P4	2.2108 ± 0.2370	$2.3206 \pm 0.1885^{**}$
T1	2.4142 ± 0.2751	$2.3758 \pm 0.1788^{***}$
T2	2.3249 ± 0.2652	2.3272 ± 0.1891

T3	2.5158 ± 0.2353	2.403 ± 0.2871
T4	2.4108 ± 0.2717	2.5224 ± 0.4084
D1	2.31 ± 0.2765	$2.3365 \pm 0.1423^{**}$
D2	2.3151 ± 0.2722	$2.3755 \pm 0.1719^{*}$
D3	2.2462 ± 0.2069	$2.4093 \pm 0.2132^{***}$
D4	2.3071 ± 0.2582	2.3446 ± 0.1604

As described in previously reported manometry results, the frequency band of interest to show the phasic contraction lies in the range of 0-12cpm. The ventilator/breathing frequency band is 13-17cpm, and the power of the higher frequency band is negligible. Manometry data has a dominant frequency band of 1-6cpm. However, the predominant frequency is difficult to be identified in the manometry data because of the densely peaks in 1-6cpm. On the other hand, frequency spectrum analysis of the bio-impedance appears to be a better indicator of phasic activity. Clear predominant frequencies of bio-impedance exist in the majority of the proximal, transverse, and distal channels during both baseline and post-stimulation periods. Our results further narrowed down the range of predominant frequency to 2-3cpm, which corresponded to the oscillation frequency that appeared in the aforementioned bio-impedance trace in the time domain. The high-resolution change of bio-impedance frequency can further reveal the colonic activity level. Figure 3.20 shows an example of the bio-impedance spectrum during baseline (blue) and post-stimulation (red) from one single experiment. The predominant peaks at around 2cpm shifted to the right along the frequency axis after the stimulation, which is a sign of the activation effects of the stimulation as the higher frequency suggests stronger activities of the corresponding colonic region. In our study, the 15-minute stimulation caused an average predominant frequency increase of 0.295cpm with the highest value of 1.639cpm. The predominant frequency increase reaches a statistical significance in 7 out of 12 impedance channels (Table 3.3).

3.3.3 Discussion

In this thesis, we used a novel bio-impedance measuring approach to monitor colonic activity and found strong local effects of the direct distal colon stimulation in both the time and frequency domain. We noted that the colonic bio-impedance drop of the distal channels correlated highly with the longitudinal contraction of the distal colon in response to the stimulation, which is intuitive as the longitudinal contraction, primarily the shrinking of the colon wall, shortens the current pathway and therefore reduces the bio-impedance. After the stimulation, the bio-impedance gradually increased, which matched with the colonic tissue recovery from the contraction status. The colonic bio-impedance of proximal and transverse channels presented divergent behaviors but were mainly inconspicuous compared to the distal colon.

In the statistical analysis, we are aware of the limited pigs/channels with many consecutive measurements collected at different time separations in this study. Therefore, instead of the repeated measure ANOVA, we applied GEE to make full use of the data and overcome the data collection problems mentioned above. The results showed that the bio-impedance changes reached statistical significance in D2 and D3 channels while most of the majority proximal and transverse channels did not. It is interesting to point out in our experiments that the statistical significance of each channel depends on the degree of colocalization between the positions of stimulation sites and recording channels. As shown in Figure 3.26, stim site 1 was between D1 and D2, and stim site 2 was between D3 and D4. Two stim sites were stimulated alternatively. When stim site 1 was on, the strongest effects were at D1 and D2, while D3 had stronger effects than D4 since D3 was closer to the stim site 1. This was true when stim site 2 was on. Therefore, D2 and D3 had more variations than D1 and D4 in general.

The heatmap derived from zAUC further highlighted the direct distal stimulation effects on the colonic phasic activities. Similar to the previously reported manometry findings, the bio-impedance method showed that the stimulation induced increased motility index in the distal colon but varying fewer responses in the proximal and transverse colon. However, there is a different interpretation for the distal channel reaction in post-stimulation duration. Manometry data showed strong activation while bio-impedance indicated inhibition. The key reason for the contrast is the positions of the manometry probes and impedance electrodes in both modalities. Due to unequal spatial resolution, there was no consistent one-to-one correspondence between the bio-impedance channel and manometry probe, which is indeed due to the limitation of the manometry resolution in our study. The bio-impedance nodes had finer spatial resolution. Four bio-impedance channels in all the experiments were placed close to the stimulation electrodes, mainly monitoring the stimulation zone, while manometry probes covered larger areas away from the stimulation sites. The Bio-impedance provided more information about the colonic activities around the stimulation site, and manometry provided more information about several centimeters away from the stimulation sites. Therefore, the two results are complementary instead of the opposite. Combining the results of the two heatmaps, it is found that the stimulation site relaxed after the strong contraction, and there might be a short propagation from the stimulation site to the nearby region after the stimulation. Moreover, consistencies were found between zAUC and pAUC in some channel-probe pairs (such as D1-D16 and T4-T19 shown in Figure 5b) for each subject from the correlation studies. When bio-impedance and pressure sensors were placed close to each other, high correlations can be observed, while the correlation decreased when the separation distance increased because of the high spatial variations in colonic activity. Our results further support the previous studies that the bio-impedance decreases when the contraction happens [7], [9], [140],

[194] and show the capability of the bio-impedance approach to indicate the luminal pressure changes. Given that direct colon stimulation, using similar parameters as the current study, did not cause any histological damage, the observed impedance change is unlikely to be confounded by tissue inflammatory response reported in the ischemic small intestine [203].

The bio-impedance responses in the time domain indicate its potential to detect colonic contraction/expansion and, as a result, to monitor the colonic motility changes. This proposed technique has several advantages. For example, its higher temporal and spatial resolution can support more precise motility monitoring. The use of customized high density stretchable planar electrodes can cover a specific area and provide more accurate spatial activity information, which makes it a better way to capture and analyze the activity propagation in specific directions. The impedance monitoring system can not only provide the colonic activity information but also provide other information, such as whether the electrode overpotential is within its water window and whether the electrode is well connected, to track the stimulation safety and effectiveness [204]–[207]. In addition, it allows simultaneous neuron signal recording and neuron stimulation if proper artifact removal is employed, which is essential to implement a real-time, close-loop control over stimulation signals.

At baseline, the dominant distal colon contraction frequency is in the range of 2-3cpm. Following stimulation, the dominant frequency shifted to the right, suggesting that stimulation leads to a higher activity level of the colon. Compared to the traditional manometry methods, the bio-impedance method can record the full frequency spectrum of the colonic activity without abandoning the DC/low-frequency components because of the noise and artifacts. While recording the evoked electrode overpotential at the interface of electrodes and colonic tissue, all frequency components of the tissue bio-impedance were modulated by the main tone at 200Hz when the

stimuli (200Hz, 0.1ms, 3uA) were applied. Consequently, low-frequency components are preserved at the sidebands, and cleaner signals can be obtained via signal processing. Besides the dominant frequency in the range of 2-3cpm, we also observed spikes beyond that range, as ~4cpm and ~6cpm, shown in Figure 3.30. However, we suspect them to be the 2^{nd} and 3^{rd} harmonic waves of the dominant frequency (~2cpm). Currently, the frequency analysis of the bio-impedance during stimulation is not provided; nevertheless, the analysis is possible in the duration of stimulation if stimulation parameters such as pulse width, frequency, and amplitude are selected carefully, as well as employing sophisticated techniques for stimulation artifact removal [208].

3.3.4 Conclusion

A novel bio-impedance method based on the Randles Cell model is proposed to monitor the colonic responses to direct distal colon stimulation. It shows that the distal colon contraction regulates the tissue's bio-impedance. The predominant frequencies of the contraction have also been detected, which increased after the stimulation in most impedance recording channels. The increase in frequencies indicates an increase in colonic activities. Moreover, statistical analysis shows correlations between the colon motility monitoring modalities used bio-impedance and manometry. This is evidenced by the data when both the impedance electrodes and manometry probes are carefully aligned. In summary, the results of the study demonstrate the potential of the bio-impedance method as a viable alternative to monitoring colonic motility.

CHAPTER 4

Conclusion and Future Directions

4.1 Conclusions

In this dissertation, we put efforts into improving the stimulation performances of the high-density transcranial direct current stimulation (tDCS). A computational model of high-density transcranial direct current stimulation (tDCS) is first established. We investigate the influence of different electrode-related factors on stimulation performances. The results indicate that a higher number of electrodes can provide better stimulation intensity and focality with the same optimization algorithm. Further, we developed an optimization algorithm Simulation with Balanced Focality and Intensity (SBFI) to guide the multi-electrode system. SBFI, by adjusting the regularization matrix $\boldsymbol{\lambda}$, can provide a balance not only between the stimulation intensity and focality but also among different target regions when applied to multi-site stimulation cases. A series of simulation experiments present its potential for different clinical applications.

We first establish a computational model of high density transcutaneous direct current stimulation (tDCS) and systematically study the influence of different electrode-related factors on the stimulation performances. To fill the gap between the simulation study and clinical application, a robustness analysis of the computation model is conducted. The results indicate that the simulation results with the computational model are stable within the ranges of the scalp and Cerebrospinal Fluid (CSF) conductivities, while the skull conductivity is most sensitive and should be carefully considered in real clinical applications. The same strategies have been demonstrated to be equally applicable to the transcutaneous spinal cord stimulation (tSCS).

In addition to the central nervous system electrical stimulation, we also explore the peripheral nervous system stimulation targeting an organ endowed with a second brain, ENS, the mammalian colon. We investigate the regional colonic motility response in both the time and frequency domain to electrical stimulation of the colonic tissue and nerves in an anesthetized porcine model. Mapping the motility response of the colon to electroceutical interventions, through simultaneous monitoring of the different regions of the colon, in a model that bears several similarities to humans, provides critical data that can guide translational studies and applications to human patients. In addition, we propose a novel bio-impedance method based on the Randles Cell model to monitor colonic motor activity. It can detect the colon contractions and the predominant frequencies with higher spatial and temporal resolutions. Positive correlations have been found between bio-impedance signals and manometry data. The results indicate that the proposed bio-impedance-based method can be a viable candidate for monitoring colonic motor patterns. The presented technique has the potential to be integrated into a closed-loop therapeutic device in order to optimize its stimulation protocol in real-time.

4.2 Future Improvements and Directions

4.2.1 Multi-electrode Non-invasive Stimulation

We develop a computational model for the multi-electrode stimulation system. The computational model is based on a template head model with standard conductivities. As discussed, the robustness tests have identified the important roles of the tissue conductivities in the optimal stimulation. Therefore, it would be interesting to develop other template models for different populations, such as children, adults, or populations with certain disease statuses in the future.

In addition, the optimization matrix $\boldsymbol{\lambda}$ is the key to balancing the stimulation distribution, which is tuned manually in the current study. It would be necessary to automate the process in the future. The Bilevel optimization [209], [210] can be one of the potential solutions in which $\boldsymbol{\lambda}$ is considered as unknown variable. Cross validation method can be another choice if a large number of datasets can be obtained and trained [211], [212].

So far, the research on the high-density tDCS and tSCS are mainly the methodology developments. Real experiments are essential to further validate the proposed computational model. For example, the simulation experiment has shown that SBFI can target multiple seizure sources simultaneously. It would be interesting to incorporate the EEG-based brain imaging technique and apply the focalized stimulation to stop the seizure or enhance cognitions. Further, the multi-electrode tSCS can be designed to target the sacral nerve roots such that it can achieve the noninvasive modulation of the colonic function, mainly in the distal colon.

4.2.2 Colonic Motility

Currently, the presented colonic functional mapping study has limitations in that data are generated in anesthetized pigs that underwent acute abdominal surgery. Hence, animals were under conditions of suppressed colonic motor activity. The results reveal the actual colonic motility responses to an acute short duration (10-15min) electrical stimulation of colon tissue or different nerves. While our studies have provided foundational functional maps of the colon's response to neuromodulation, the translational value of the stimulations on colon function requires improvement by measurements in awake pigs and under chronic neuromodulation, with no acute invasive surgery that inhibits motility. The conditions of being under anesthesia and involving invasive surgery are known to alter enteric neurotransmission and cause ileus. These factors

confound the interpretability of data into a more physiological awake pig colon motility state. Thus, the effect of neuromodulation on colon motility in awake states remains unknown. Therefore, it is important to 1) identify chronic stimulation parameters that stimulate chronic motility, transit and defecation. 2) fill the above gap in both fronts of knowledge and technology on the impact specific of chronic electrical stimulations in pigs.

With the preceding chronic and planned awake neuromodulation model, greater physiological fidelity to colon motility and a greater potential for translational research will be possessed. Hence, we can further explore colonic electrical stimulation as a potential neuromodulation target for colonic diseases such as chronic constipation. Chronic constipation is a common problem for all ages. It affects about 15% of the adult population, with a higher prevalence among the elderly. One of the common causes of chronic constipation is opioid-induced constipation (OIC). OIC occurs in up to 40-90% of non-cancer patients receiving opioids. We can first develop a model of OIC in pigs. Then, the effectiveness of the colonic stimulation can be tested with the OIC model.

Lastly, the proposed bio-impedance-based method is hard-ware efficient and requires no tedious computation. It would be interesting to integrate this technique into a closed-loop therapeutic device. With the colonic feedback provided by the bio-impedance, the system will be able to optimize its stimulation protocol in real-time.

Reference

[1] S.-H. Lee and Y. Dan, "Neuromodulation of Brain States," *Neuron*, vol. 76, no. 1, pp. 209–222, Oct. 2012, doi: 10.1016/j.neuron.2012.09.012.

[2] E. Santarnecchi, A.-K. Brem, E. Levenbaum, T. Thompson, R. C. Kadosh, and A. Pascual-Leone, "Enhancing cognition using transcranial electrical stimulation," *Current Opinion in Behavioral Sciences*, vol. 4, pp. 171–178, Aug. 2015, doi: 10.1016/j.cobeha.2015.06.003.

[3] A. Biasiucci *et al.*, "Brain-actuated functional electrical stimulation elicits lasting arm motor recovery after stroke," *Nat Commun*, vol. 9, no. 1, p. 2421, Dec. 2018, doi: 10.1038/s41467-018-04673-z.

[4] S. Shahdoost *et al.*, "A miniaturized brain-machine-spinal cord interface (BMSI) for closed-loop intraspinal microstimulation," in *2016 IEEE Biomedical Circuits and Systems Conference (BioCAS)*, Shanghai, China, Oct. 2016, pp. 364–367. doi: 10.1109/BioCAS.2016.7833807.

[5] W. Liu, P.-M. Wang, and Y.-K. Lo, "Towards closed-loop neuromodulation: a wireless miniaturized neural implant SoC," Anaheim, California, United States, May 2017, p. 1019414. doi: 10.1117/12.2263566.

[6] Y.-K. Lo *et al.*, "A Fully Integrated Wireless SoC for Motor Function Recovery After Spinal Cord Injury," *IEEE Trans. Biomed. Circuits Syst.*, vol. 11, no. 3, pp. 497–509, Jun. 2017, doi: 10.1109/TBCAS.2017.2679441.

[7] A. J. Arriagada, A. S. Jurkov, E. Neshev, G. Muench, C. N. Andrews, and M. P. Mintchev, "Design, implementation and testing of an implantable impedance-based feedback-controlled

neural gastric stimulator," *Physiol. Meas.*, vol. 32, no. 8, pp. 1103–1115, Aug. 2011, doi: 10.1088/0967-3334/32/8/007.

[8] S. Deb *et al.*, "Development of innovative techniques for the endoscopic implantation and securing of a novel, wireless, miniature gastrostimulator (with videos)," *Gastrointestinal Endoscopy*, vol. 76, no. 1, pp. 179–184, Jul. 2012, doi: 10.1016/j.gie.2012.03.177.

[9] Y.-K. Lo *et al.*, "A Wireless Implant for Gastrointestinal Motility Disorders," *Micromachines*, vol. 9, no. 1, p. 17, Jan. 2018, doi: 10.3390/mi9010017.

[10] Yi-Kai Lo, Kuanfu Chen, P. Gad, and Wentai Liu, "A Fully-Integrated High-Compliance Voltage SoC for Epi-Retinal and Neural Prostheses," *IEEE Trans. Biomed. Circuits Syst.*, vol. 7, no. 6, pp. 761–772, Dec. 2013, doi: 10.1109/TBCAS.2013.2297695.

[11] M. A. Nitsche, P. S. Boggio, F. Fregni, and A. Pascual-Leone, "Treatment of depression with transcranial direct current stimulation (tDCS): A Review," *Experimental Neurology*, vol. 219, no. 1, pp. 14–19, Sep. 2009, doi: 10.1016/j.expneurol.2009.03.038.

[12] R. Ferrucci *et al.*, "Transcranial direct current stimulation in severe, drug-resistant major depression," *Journal of Affective Disorders*, vol. 118, no. 1–3, pp. 215–219, Nov. 2009, doi: 10.1016/j.jad.2009.02.015.

[13] P. Shiozawa *et al.*, "Transcranial direct current stimulation for major depression: an updated systematic review and meta-analysis," *Int. J. Neuropsychopharm.*, vol. 17, no. 09, pp. 1443–1452, Sep. 2014, doi: 10.1017/S1461145714000418.

[14] D. Liebetanz *et al.*, "Anticonvulsant Effects of Transcranial Direct-current Stimulation (tDCS) in the Rat Cortical Ramp Model of Focal Epilepsy," *Epilepsia*, vol. 47, no. 7, pp. 1216–1224, Jul. 2006, doi: 10.1111/j.1528-1167.2006.00539.x.

[15] N. Auvichayapat *et al.*, "Transcranial Direct Current Stimulation for Treatment of Refractory Childhood Focal Epilepsy," *Brain Stimulation*, vol. 6, no. 4, pp. 696–700, Jul. 2013, doi: 10.1016/j.brs.2013.01.009.

[16] D. San-juan *et al.*, "Transcranial Direct Current Stimulation in Epilepsy," *Brain Stimulation*, vol. 8, no. 3, pp. 455–464, May 2015, doi: 10.1016/j.brs.2015.01.001.

[17] P. S. Boggio *et al.*, "Effects of transcranial direct current stimulation on working memory in patients with Parkinson's disease," *Journal of the Neurological Sciences*, vol. 249, no. 1, pp. 31–38, Nov. 2006, doi: 10.1016/j.jns.2006.05.062.

[18] D. H. Benninger *et al.*, "Transcranial direct current stimulation for the treatment of Parkinson's disease," *Journal of Neurology, Neurosurgery & Psychiatry*, vol. 81, no. 10, pp. 1105–1111, Oct. 2010, doi: 10.1136/jnnp.2009.202556.

[19] M. Dagan *et al.*, "Multitarget transcranial direct current stimulation for freezing of gait in Parkinson's disease: Multitarget tDCS for freezing of gait in PD," *Mov Disord.*, vol. 33, no. 4, pp. 642–646, Apr. 2018, doi: 10.1002/mds.27300.

[20] B. W. Vines, C. Cerruti, and G. Schlaug, "Dual-hemisphere tDCS facilitates greater improvements for healthy subjects' non-dominant hand compared to uni-hemisphere stimulation," *BMC Neurosci*, vol. 9, no. 1, p. 103, 2008, doi: 10.1186/1471-2202-9-103.

[21] R. Sparing, M. Dafotakis, I. G. Meister, N. Thirugnanasambandam, and G. R. Fink, "Enhancing language performance with non-invasive brain stimulation—A transcranial direct current stimulation study in healthy humans," *Neuropsychologia*, vol. 46, no. 1, pp. 261–268, Jan. 2008, doi: 10.1016/j.neuropsychologia.2007.07.009.

[22] Z. Cattaneo, A. Pisoni, and C. Papagno, "Transcranial direct current stimulation over Broca's region improves phonemic and semantic fluency in healthy individuals," *Neuroscience*, vol. 183, pp. 64–70, Jun. 2011, doi: 10.1016/j.neuroscience.2011.03.058.

[23] B. A. Coffman, V. P. Clark, and R. Parasuraman, "Battery powered thought: Enhancement of attention, learning, and memory in healthy adults using transcranial direct current stimulation," *NeuroImage*, vol. 85, pp. 895–908, Jan. 2014, doi: 10.1016/j.neuroimage.2013.07.083.

[24] Y. Li, J. Qin, S. Osher, and W. Liu, "Graph fractional-order total variation EEG source reconstruction," in *2016 38th Annual International Conference of the IEEE Engineering in Medicine and Biology Society (EMBC)*, Orlando, FL, USA, Aug. 2016, pp. 101–104. doi: 10.1109/EMBC.2016.7590650.

[25] Y. Li, J. Qin, Y.-L. Hsin, S. Osher, and W. Liu, "s-SMOOTH: Sparsity and Smoothness Enhanced EEG Brain Tomography," *Front. Neurosci.*, vol. 10, Nov. 2016, doi: 10.3389/fnins.2016.00543.

[26] M. Fernández-Corazza, S. Turovets, P. Luu, E. Anderson, and D. Tucker, "Transcranial Electrical Neuromodulation Based on the Reciprocity Principle," *Frontiers in Psychiatry*, vol. 7, May 2016, doi: 10.3389/fpsyt.2016.00087.

[27] S. Guler *et al.*, "Optimization of focality and direction in dense electrode array transcranial direct current stimulation (tDCS)," *Journal of Neural Engineering*, vol. 13, no. 3, p. 036020, Jun. 2016, doi: 10.1088/1741-2560/13/3/036020.

[28] Y. Wang, H. Zhou, Y. Li, and W. Liu, "Impact of Electrode Number on the Performance of High-Definition Transcranial Direct Current Stimulation (HD-tDCS)," in *2018 40th Annual International Conference of the IEEE Engineering in Medicine and Biology Society (EMBC)*, Honolulu, HI, Jul. 2018, pp. 4182–4185. doi: 10.1109/EMBC.2018.8513379.

[29] J. Qin, T. Wu, Y. Li, W. Yin, S. Osher, and W. Liu, "Accelerated High-Resolution EEG Source Imaging," p. 4.

[30] J. P. Dmochowski, A. Datta, M. Bikson, Y. Su, and L. C. Parra, "Optimized multi-electrode stimulation increases focality and intensity at target," *Journal of Neural Engineering*, vol. 8, no. 4, p. 046011, Aug. 2011, doi: 10.1088/1741-2560/8/4/046011.

[31] G. Ruffini, M. D. Fox, O. Ripolles, P. C. Miranda, and A. Pascual-Leone, "Optimization of multifocal transcranial current stimulation for weighted cortical pattern targeting from realistic modeling of electric fields," *NeuroImage*, vol. 89, pp. 216–225, Apr. 2014, doi: 10.1016/j.neuroimage.2013.12.002.

[32] J. P. Dmochowski, M. Bikson, A. Datta, J. Richardson, J. Fridriksson, and L. C. Parra, "On the role of electric field orientation in optimal design of transcranial current stimulation," in *2012 Annual International Conference of the IEEE Engineering in Medicine and Biology Society*, San Diego, CA, Aug. 2012, pp. 6426–6429. doi: 10.1109/EMBC.2012.6347465.

[33] R. J. Sadleir, T. D. Vannorsdall, D. J. Schretlen, and B. Gordon, "Target Optimization in Transcranial Direct Current Stimulation," *Frontiers in Psychiatry*, vol. 3, 2012, doi: 10.3389/fpsyt.2012.00090.

[34] G. B. Saturnino, H. R. Siebner, A. Thielscher, and K. H. Madsen, "Accessibility of cortical regions to focal TES: Dependence on spatial position, safety, and practical constraints," *NeuroImage*, vol. 203, p. 116183, Dec. 2019, doi: 10.1016/j.neuroimage.2019.116183.

[35] M. Bikson *et al.*, "Safety of Transcranial Direct Current Stimulation: Evidence Based Update 2016," *Brain Stimulation*, vol. 9, no. 5, pp. 641–661, Sep. 2016, doi: 10.1016/j.brs.2016.06.004.

[36] M. A. Nitsche and M. Bikson, "Extending the parameter range for tDCS: Safety and tolerability of 4 mA stimulation," *Brain Stimulation*, vol. 10, no. 3, pp. 541–542, May 2017, doi: 10.1016/j.brs.2017.03.002.

[37] N. Khadka *et al.*, "Adaptive current tDCS up to 4 mA," *Brain Stimulation*, vol. 13, no. 1, pp. 69–79, Jan. 2020, doi: 10.1016/j.brs.2019.07.027.

[38] D. Edwards, M. Cortes, A. Datta, P. Minhas, E. M. Wassermann, and M. Bikson, "Physiological and modeling evidence for focal transcranial electrical brain stimulation in humans: A basis for high-definition tDCS," *NeuroImage*, vol. 74, pp. 266–275, Jul. 2013, doi: 10.1016/j.neuroimage.2013.01.042.

[39] Z. Esmaeilpour *et al.*, "Proceedings #21. Intracranial voltage recording during transcranial direct current stimulation (tDCS) in human subjects with validation of a standard model," *Brain Stimulation*, vol. 10, no. 4, pp. e72–e75, Jul. 2017, doi: 10.1016/j.brs.2017.04.114.

[40] R. Oostenveld, P. Fries, E. Maris, and J.-M. Schoffelen, "FieldTrip: Open Source Software for Advanced Analysis of MEG, EEG, and Invasive Electrophysiological Data," *Computational Intelligence and Neuroscience*, vol. 2011, pp. 1–9, 2011, doi: 10.1155/2011/156869.

[41] P. Faria, M. Hallett, and P. C. Miranda, "A finite element analysis of the effect of electrode area and inter-electrode distance on the spatial distribution of the current density in tDCS," *J. Neural Eng.*, vol. 8, no. 6, p. 066017, Dec. 2011, doi: 10.1088/1741-2560/8/6/066017.

[42] M. A. Nitsche *et al.*, "Shaping the Effects of Transcranial Direct Current Stimulation of the Human Motor Cortex," *Journal of Neurophysiology*, vol. 97, no. 4, pp. 3109–3117, Apr. 2007, doi: 10.1152/jn.01312.2006.

[43] R. Oostenveld and P. Praamstra, "The five percent electrode system for high-resolution EEG and ERP measurements," *Clinical Neurophysiology*, p. 7, 2001.

[44] V. Jurcak, D. Tsuzuki, and I. Dan, "10/20, 10/10, and 10/5 systems revisited: Their validity as relative head-surface-based positioning systems," *NeuroImage*, vol. 34, no. 4, pp. 1600–1611, Feb. 2007, doi: 10.1016/j.neuroimage.2006.09.024.

[45] L. Golestanirad *et al.*, "Analysis of fractal electrodes for efficient neural stimulation," *Front. Neuroeng.*, vol. 6, 2013, doi: 10.3389/fneng.2013.00003.

[46] S. Mahdavi, F. Towhidkhah, and N. Fatouraee, "Efficacy of fractal electrodes in transcranial direct current stimulation: A computational modeling study," in *2015 23rd Iranian Conference on Electrical Engineering*, Tehran, Iran, May 2015, pp. 99–103. doi: 10.1109/IranianCEE.2015.7146190.

[47] “Implantable Electrode Design – The Cleveland FES Center.” https://fescenter.org/research/technology-programs/implantable-electrode-design/ (accessed Nov. 09, 2021).

[48] Y. Li, *Neural Signal Processing: Electrode-based Brain Imaging, Focalized Neural Stimulation, and Neural Dynamics Study*. University of California, Los Angeles, 2017.

[49] S. Kühn and J. Gallinat, “A Quantitative Meta-Analysis on Cue-Induced Male Sexual Arousal,” *The Journal of Sexual Medicine*, vol. 8, no. 8, pp. 2269–2275, Aug. 2011, doi: 10.1111/j.1743-6109.2011.02322.x.

[50] S. Stoléru, V. Fonteille, C. Cornélis, C. Joyal, and V. Moulier, “Functional neuroimaging studies of sexual arousal and orgasm in healthy men and women: A review and meta-analysis,” *Neuroscience & Biobehavioral Reviews*, vol. 36, no. 6, pp. 1481–1509, Jul. 2012, doi: 10.1016/j.neubiorev.2012.03.006.

[51] L. Zhao *et al.*, “Aberrant Topological Patterns of Structural Cortical Networks in Psychogenic Erectile Dysfunction,” *Front. Hum. Neurosci.*, vol. 9, Dec. 2015, doi: 10.3389/fnhum.2015.00675.

[52] L. Mencarelli *et al.*, “Impact of network-targeted multichannel transcranial direct current stimulation on intrinsic and network-to-network functional connectivity,” *J Neurosci Res*, vol. 98, no. 10, pp. 1843–1856, Oct. 2020, doi: 10.1002/jnr.24690.

[53] J. P. Dmochowski, L. Koessler, A. M. Norcia, M. Bikson, and L. C. Parra, “Optimal use of EEG recordings to target active brain areas with transcranial electrical stimulation,” *NeuroImage*, vol. 157, pp. 69–80, Aug. 2017, doi: 10.1016/j.neuroimage.2017.05.059.

[54] Y. Zheng *et al.*, "Acute Seizure Control Efficacy of Multi-Site Closed-Loop Stimulation in a Temporal Lobe Seizure Model," *IEEE Trans. Neural Syst. Rehabil. Eng.*, vol. 27, no. 3, pp. 419–428, Mar. 2019, doi: 10.1109/TNSRE.2019.2894746.

[55] C. Schmidt, S. Wagner, M. Burger, U. van Rienen, and C. H. Wolters, "Impact of uncertain head tissue conductivity in the optimization of transcranial direct current stimulation for an auditory target," *J. Neural Eng.*, vol. 12, no. 4, p. 046028, Aug. 2015, doi: 10.1088/1741-2560/12/4/046028.

[56] G. B. Saturnino, A. Thielscher, K. H. Madsen, T. R. Knösche, and K. Weise, "A principled approach to conductivity uncertainty analysis in electric field calculations," *NeuroImage*, vol. 188, pp. 821–834, Mar. 2019, doi: 10.1016/j.neuroimage.2018.12.053.

[57] H. McCann, G. Pisano, and L. Beltrachini, "Variation in Reported Human Head Tissue Electrical Conductivity Values," *Brain Topogr*, vol. 32, no. 5, pp. 825–858, Sep. 2019, doi: 10.1007/s10548-019-00710-2.

[58] R. Hoekema, G. H. Wieneke, F. S. S. Leijten, J. Ansems, and A. C. van Huffelen, "Measurement of the Conductivity of Skull, Temporarily Removed During Epilepsy Surgery," p. 10.

[59] K. Wendel, J. Väisänen, G. Seemann, J. Hyttinen, and J. Malmivuo, "The Influence of Age and Skull Conductivity on Surface and Subdermal Bipolar EEG Leads," *Computational Intelligence and Neuroscience*, vol. 2010, pp. 1–7, 2010, doi: 10.1155/2010/397272.

[60] M. Antonakakis *et al.*, "Inter-Subject Variability of Skull Conductivity and Thickness in Calibrated Realistic Head Models," *NeuroImage*, vol. 223, p. 117353, Dec. 2020, doi: 10.1016/j.neuroimage.2020.117353.

[61] D. E. Bullard and T. T. Makachinas, “Measurement of tissue impedence in conjunction with computed tomography-guided stereotaxic biopsies.,” *Journal of Neurology, Neurosurgery & Psychiatry*, vol. 50, no. 1, pp. 43–51, Jan. 1987, doi: 10.1136/jnnp.50.1.43.

[62] F. Vatta, P. Bruno, and P. Inchingolo, “Improving Lesion Conductivity Estimate by Means of EEG Source Localization Sensitivity to Model Parameter:,” *Journal of Clinical Neurophysiology*, vol. 19, no. 1, pp. 1–15, Jan. 2002, doi: 10.1097/00004691-200201000-00001.

[63] L. Yang *et al.*, “Ex-Vivo Characterization of Bioimpedance Spectroscopy of Normal, Ischemic and Hemorrhagic Rabbit Brain Tissue at Frequencies from 10 Hz to 1 MHz,” *Sensors*, vol. 16, no. 11, p. 1942, Nov. 2016, doi: 10.3390/s16111942.

[64] J. Ladenbauer, K. Minassian, U. S. Hofstoetter, M. R. Dimitrijevic, and F. Rattay, “Stimulation of the Human Lumbar Spinal Cord With Implanted and Surface Electrodes: A Computer Simulation Study,” *IEEE Trans. Neural Syst. Rehabil. Eng.*, vol. 18, no. 6, pp. 637–645, Dec. 2010, doi: 10.1109/TNSRE.2010.2054112.

[65] S. M. Danner, U. S. Hofstoetter, J. Ladenbauer, F. Rattay, and K. Minassian, “Can the Human Lumbar Posterior Columns Be Stimulated by Transcutaneous Spinal Cord Stimulation? A Modeling Study: MODELING TRANSCUTANEOUS POSTERIOR COLUMNS STIMULATION,” *Artificial Organs*, vol. 35, no. 3, pp. 257–262, Mar. 2011, doi: 10.1111/j.1525-1594.2011.01213.x.

[66] C. A. Angeli, V. R. Edgerton, Y. P. Gerasimenko, and S. J. Harkema, “Altering spinal cord excitability enables voluntary movements after chronic complete paralysis in humans,” *Brain*, vol. 137, no. 5, pp. 1394–1409, May 2014, doi: 10.1093/brain/awu038.

[67] R. B. North, M. G. Ewend, M. T. Lawton, and S. Piantadosi, “Spinal cord stimulation for chronic, intractable pain: Superiority of ‘multi-channel’ devices,” *Pain*, vol. 44, no. 2, pp. 119–130, Feb. 1991, doi: 10.1016/0304-3959(91)90125-H.

[68] R. B. North, D. H. Kidd, M. Zahurak, C. S. James, and D. M. Long, “Spinal Cord Stimulation for Chronic, Intractable Pain: Experience over Two Decades,” *Neurosurgery*, vol. 32, no. 3, pp. 384–395, Mar. 1993, doi: 10.1227/00006123-199303000-00008.

[69] T. Cameron, “Safety and efficacy of spinal cord stimulation for the treatment of chronic pain: a 20-year literature review,” *Journal of Neurosurgery: Spine*, vol. 100, no. 3, pp. 254–267, Mar. 2004, doi: 10.3171/spi.2004.100.3.0254.

[70] J. J. Song, “Present and Potential Use of Spinal CordStimulation to Control Chronic Pain,” *Pain Phys*, vol. 3;17, no. 3;5, pp. 234–246, May 2014, doi: 10.36076/ppj.2014/17/234.

[71] U. S. Hofstoetter, W. B. McKay, K. E. Tansey, W. Mayr, H. Kern, and K. Minassian, “Modification of spasticity by transcutaneous spinal cord stimulation in individuals with incomplete spinal cord injury,” *The Journal of Spinal Cord Medicine*, vol. 37, no. 2, pp. 202–211, Mar. 2014, doi: 10.1179/2045772313Y.0000000149.

[72] U. S. Hofstoetter *et al.*, “Transcutaneous Spinal Cord Stimulation Induces Temporary Attenuation of Spasticity in Individuals with Spinal Cord Injury,” *Journal of Neurotrauma*, vol. 37, no. 3, pp. 481–493, Feb. 2020, doi: 10.1089/neu.2019.6588.

[73] M. Krenn, U. S. Hofstoetter, S. M. Danner, K. Minassian, and W. Mayr, “Multi-Electrode Array for Transcutaneous Lumbar Posterior Root Stimulation: Multi-Electrode Array,” *Artificial Organs*, vol. 39, no. 10, pp. 834–840, Oct. 2015, doi: 10.1111/aor.12616.

[74] Kuanfu Chen, Yi-Kai Lo, and Wentai Liu, "A 37.6mm^2 1024-channel high-compliance-voltage SoC for epiretinal prostheses," in *2013 IEEE International Solid-State Circuits Conference Digest of Technical Papers*, San Francisco, CA, Feb. 2013, pp. 294–295. doi: 10.1109/ISSCC.2013.6487741.

[75] "The National Library of Medicines Visible Human Project." https://www.nlm.nih.gov/research/visible/visible_human.html (accessed Mar. 19, 2022).

[76] E. R. Feldman and J. W. Burdick, "Modeling motor responses of paraplegics under epidural spinal cord stimulation," in *2017 8th International IEEE/EMBS Conference on Neural Engineering (NER)*, Shanghai, China, May 2017, pp. 354–357. doi: 10.1109/NER.2017.8008363.

[77] Y. Gerasimenko, R. Gorodnichev, T. Moshonkina, D. Sayenko, P. Gad, and V. Reggie Edgerton, "Transcutaneous electrical spinal-cord stimulation in humans," *Annals of Physical and Rehabilitation Medicine*, vol. 58, no. 4, pp. 225–231, Sep. 2015, doi: 10.1016/j.rehab.2015.05.003.

[78] U. S. Hofstoetter, B. Freundl, H. Binder, and K. Minassian, "Common neural structures activated by epidural and transcutaneous lumbar spinal cord stimulation: Elicitation of posterior root-muscle reflexes," *PLoS ONE*, vol. 13, no. 1, p. e0192013, Jan. 2018, doi: 10.1371/journal.pone.0192013.

[79] M. D. Gershon, A. L. Kirchgessner, and P. R. Wade, "Functional anatomy of the enteric nervous system," *Physiology of the gastrointestinal tract*, vol. 1, pp. 381–422, 1994.

[80] R. K. Goyal, "The Enteric Nervous System," *THE NEW ENGLAND JOURNAL OF MEDICINE*, vol. 334, no. 17, p. 10, 1996.

[81] M. D. Gershon, “The Enteric Nervous System: A Second Brain,” *Hospital Practice*, vol. 34, no. 7, pp. 31–52, Jul. 1999, doi: 10.3810/hp.1999.07.153.

[82] E. E. Benarroch, “Enteric nervous system,” *Neurology*, vol. 69, no. 20, p. 1953, Nov. 2007, doi: 10.1212/01.wnl.0000281999.56102.b5.

[83] J. B. Furness, “The enteric nervous system and neurogastroenterology,” *Nature Reviews Gastroenterology & Hepatology*, vol. 9, no. 5, pp. 286–294, May 2012, doi: 10.1038/nrgastro.2012.32.

[84] L. Chang *et al.*, “Functional Bowel Disorders: A Roadmap to Guide the Next Generation of Research,” *Gastroenterology*, vol. 154, no. 3, pp. 723–735, Feb. 2018, doi: 10.1053/j.gastro.2017.12.010.

[85] S. Fukudo *et al.*, “Exaggerated motility of the descending colon with repetitive distention of the sigmoid colon in patients with irritable bowel syndrome,” *J Gastroenterol*, vol. 37, no. S14, pp. 145–150, Jan. 2002, doi: 10.1007/BF03326434.

[86] P. D. R. Higgins and J. F. Johanson, “Epidemiology of constipation in North America: a systematic review.,” *Am J Gastroenterol*, vol. 99, no. 4, pp. 750–759, Apr. 2004, doi: 10.1111/j.1572-0241.2004.04114.x.

[87] Knowles and Martin, “Slow transit constipation: a model of human gut dysmotility. Review of possible aetiologies,” *Neurogastroenterol Motil*, vol. 12, no. 2, pp. 181–196, Apr. 2000, doi: 10.1046/j.1365-2982.2000.00198.x.

[88] J. C. Rabine and J. L. Barnett, “Management of the Patient with Gastroparesis:,” *Journal of Clinical Gastroenterology*, vol. 32, no. 1, pp. 11–18, Jan. 2001, doi: 10.1097/00004836-200101000-00005.

[89] J. W. Wiley and L. Chang, “Functional Bowel Disorders,” *Gastroenterology*, vol. 155, no. 1, pp. 1–4, Jul. 2018, doi: 10.1053/j.gastro.2018.02.014.

[90] C. Liu, C. Huang, Y. Yang, S. Chen, M. Weng, and M. Huang, “Relationship between neurogenic bowel dysfunction and health-related quality of life in persons with spinal cord injury,” *J Rehabil Med*, vol. 41, no. 1, pp. 35–40, 2009, doi: 10.2340/16501977-0277.

[91] Z. Qi, J. W. Middleton, and A. Malcolm, “Bowel Dysfunction in Spinal Cord Injury,” *Curr Gastroenterol Rep*, vol. 20, no. 10, p. 47, Oct. 2018, doi: 10.1007/s11894-018-0655-4.

[92] J. S. Scolapio, “Current update of short-bowel syndrome:,” *Current Opinion in Gastroenterology*, vol. 20, no. 2, pp. 143–145, Mar. 2004, doi: 10.1097/00001574-200403000-00016.

[93] J. D. Z. Chen, J. Yin, and W. Wei, “Electrical therapies for gastrointestinal motility disorders,” *Expert Review of Gastroenterology & Hepatology*, vol. 11, no. 5, pp. 407–418, May 2017, doi: 10.1080/17474124.2017.1298441.

[94] C. C. Horn, J. L. Ardell, and L. E. Fisher, “Electroceutical Targeting of the Autonomic Nervous System,” *Physiology*, vol. 34, no. 2, pp. 150–162, Mar. 2019, doi: 10.1152/physiol.00030.2018.

[95] C. Sevcencu, “A Review of Electrical Stimulation to Treat Motility Dysfunctions in the Digestive Tract: Effects and Stimulation Patterns,” *Neuromodulation: Technology at the*

Neural Interface, vol. 10, no. 2, pp. 85–99, Apr. 2007, doi: 10.1111/j.1525-1403.2007.00097.x.

[96] J. B. Furness, "Integrated Neural and Endocrine Control of Gastrointestinal Function," in *The Enteric Nervous System: 30 Years Later*, S. Brierley and M. Costa, Eds. Cham: Springer International Publishing, 2016, pp. 159–173. doi: 10.1007/978-3-319-27592-5_16.

[97] B. R. Southwell, "Electro-Neuromodulation for Colonic Disorders—Review of Meta-Analyses, Systematic Reviews, and RCTs," *Neuromodulation: Technology at the Neural Interface*, vol. 23, no. 8, pp. 1061–1081, Dec. 2020, doi: 10.1111/ner.13099.

[98] S. C. Payne, J. B. Furness, and M. J. Stebbing, "Bioelectric neuromodulation for gastrointestinal disorders: effectiveness and mechanisms," *Nat Rev Gastroenterol Hepatol*, vol. 16, no. 2, pp. 89–105, Feb. 2019, doi: 10.1038/s41575-018-0078-6.

[99] M. Camilleri *et al.*, "Intra-abdominal vagal blocking (VBLOC therapy): Clinical results with a new implantable medical device," *Surgery*, vol. 143, no. 6, pp. 723–731, Jun. 2008, doi: 10.1016/j.surg.2008.03.015.

[100] R. W. McCallum *et al.*, "Gastric electrical stimulation with Enterra therapy improves symptoms of idiopathic gastroparesis," *Neurogastroenterol. Motil.*, vol. 25, no. 10, p. 815, Oct. 2013, doi: 10.1111/nmo.12185.

[101] P. Ducrotte *et al.*, "Gastric Electrical Stimulation Reduces Refractory Vomiting in a Randomized Crossover Trial," *Gastroenterology*, vol. 158, no. 3, pp. 506-514.e2, Feb. 2020, doi: 10.1053/j.gastro.2019.10.018.

[102] J. Martellucci and A. Valeri, “Colonic electrical stimulation for the treatment of slow-transit constipation: a preliminary pilot study,” *Surg Endosc*, vol. 28, no. 2, pp. 691–697, Feb. 2014, doi: 10.1007/s00464-013-3192-0.

[103] A. Shafik, “Colonic Pacing: A Therapeutic Option for the Treatment of Constipation Due to Total Colonic Inertia,” *Arch Surg*, vol. 139, no. 7, p. 775, Jul. 2004, doi: 10.1001/archsurg.139.7.775.

[104] A.-M. Leroi *et al.*, “Efficacy of Sacral Nerve Stimulation for Fecal Incontinence: Results of a Multicenter Double-Blind Crossover Study,” *Annals of Surgery*, vol. 242, no. 5, pp. 662–669, Nov. 2005, doi: 10.1097/01.sla.0000186281.09475.db.

[105] P. G. Dinning, S. E. Fuentealba, M. L. Kennedy, D. Z. Lubowski, and I. J. Cook, “Sacral nerve stimulation induces pan-colonic propagating pressure waves and increases defecation frequency in patients with slow-transit constipation,” *Colorect Dis*, vol. 9, no. 2, pp. 123–132, Feb. 2007, doi: 10.1111/j.1463-1318.2006.01096.x.

[106] J. Fioramonti and L. Bueno, “Motor activity in the large intestine of the pig related to dietary fibre and retention time,” *Br J Nutr*, vol. 43, no. 1, pp. 155–162, Jan. 1980, doi: 10.1079/BJN19800074.

[107] G. Gourcerol, L. Wang, D. W. Adelson, M. Larauche, Y. Taché, and M. Million, “Cholinergic giant migrating contractions in conscious mouse colon assessed by using a novel noninvasive solid-state manometry method: modulation by stressors,” *American Journal of Physiology-Gastrointestinal and Liver Physiology*, vol. 296, no. 5, pp. G992–G1002, May 2009, doi: 10.1152/ajpgi.90436.2008.

[108] M. Li, C. P. Johnson, M. B. Adams, and S. K. Sarna, "Cholinergic and nitrergic regulation of in vivo giant migrating contractions in rat colon," *American Journal of Physiology-Gastrointestinal and Liver Physiology*, vol. 283, no. 3, pp. G544–G552, Sep. 2002, doi: 10.1152/ajpgi.00114.2001.

[109] S. K. Sarna, "Schuster Atlas of GASTROINTESTINAL MOTILITY in Health and Disease," 2002.

[110] A. Shafik, A. A. Shafik, O. El-Sibai, and I. Ahmed, "Electrophysiologic Identification of the Location of the Colonic Pacemakers in Humans: Further Study," *Journal of Investigative Surgery*, vol. 16, no. 5, pp. 289–297, Jan. 2003, doi: 10.1080/08941930390230432.

[111] P. Vodička *et al.*, "The Miniature Pig as an Animal Model in Biomedical Research," *Annals of the New York Academy of Sciences*, vol. 1049, no. 1, pp. 161–171, May 2005, doi: 10.1196/annals.1334.015.

[112] L. Yin *et al.*, "Pig models on intestinal development and therapeutics," *Amino Acids*, vol. 49, no. 12, pp. 2099–2106, Dec. 2017, doi: 10.1007/s00726-017-2497-z.

[113] A. Ziegler, L. Gonzalez, and A. Blikslager, "Large Animal Models: The Key to Translational Discovery in Digestive Disease Research," *Cellular and Molecular Gastroenterology and Hepatology*, vol. 2, no. 6, pp. 716–724, Nov. 2016, doi: 10.1016/j.jcmgh.2016.09.003.

[114] T. T. Kararli, "Comparison of the gastrointestinal anatomy, physiology, and biochemistry of humans and commonly used laboratory animals," *Biopharm. Drug Dispos.*, vol. 16, no. 5, pp. 351–380, Jul. 1995, doi: 10.1002/bdd.2510160502.

[115] E. R. Miller and D. E. Ullrey, “The Pig as a Model for Human Nutrition,” p. 22.

[116] X. Pang *et al.*, “Inter-species transplantation of gut microbiota from human to pigs,” *ISME J*, vol. 1, no. 2, pp. 156–162, Jun. 2007, doi: 10.1038/ismej.2007.23.

[117] N. V. de Camp, A. Heimann, O. Kempski, and J. Bergeler, “Accelerometer-Based Assessment of Intestinal Peristalsis: Toward Miniaturized Low-Power Solutions for Intestinal Implants,” *IEEE J. Transl. Eng. Health Med.*, vol. 6, pp. 1–7, 2018, doi: 10.1109/JTEHM.2018.2864975.

[118] J. F. Schiemer *et al.*, “Five-fold Gastrointestinal Electrical Stimulation With Electromyography-based Activity Analysis: Towards Multilocular Theranostic Intestinal Implants,” *J Neurogastroenterol Motil*, vol. 25, no. 3, pp. 461–470, Jul. 2019, doi: 10.5056/jnm19045.

[119] c. sevcencu, n. j. m. rijkhoff, h. gregersen, and t. sinkjaer, “Propulsive activity induced by sequential electrical stimulation in the descending colon of the pig,” *Neurogastroenterol Motil*, vol. 17, no. 3, pp. 376–387, Jun. 2005, doi: 10.1111/j.1365-2982.2004.00637.x.

[120] C. Sevcencu, N. J. M. Rijkhoff, H. Gregersen, and T. Sinkjaer, “Electrical Stimulation to Induce Propulsive Contractions in the Porcine Descending Colon,” *Artificial Organs*, vol. 29, no. 3, pp. 246–249, Mar. 2005, doi: 10.1111/j.1525-1594.2005.29045.x.

[121] S. Aellen *et al.*, “Electrical stimulation induces propagated colonic contractions in an experimental model,” *British Journal of Surgery*, vol. 96, no. 2, pp. 214–220, Jan. 2009, doi: 10.1002/bjs.6455.

[122] M. Bertschi *et al.*, "Direct Electrical Stimulation Using a Battery-Operated Device for Induction and Modulation of Colonic Contractions in Pigs," *Ann Biomed Eng*, vol. 38, no. 7, pp. 2398–2405, Jul. 2010, doi: 10.1007/s10439-010-9985-6.

[123] j. vaucher *et al.*, "Electrical colonic stimulation reduces mean transit time in a porcine model," *Neurogastroenterology & Motility*, Jul. 2009, doi: 10.1111/j.1365-2982.2009.01359.x.

[124] S. Liu and J. D. Z. Chen, "Colonic Electrical Stimulation Regulates Colonic Transit Via the Nitrergic Pathway in Rats," *Dig Dis Sci*, vol. 51, no. 3, pp. 502–505, Mar. 2006, doi: 10.1007/s10620-006-3162-7.

[125] C. Sevcencu, N. J. M. Rijkhoff, and T. Sinkjaer, "Muscular vs. Neural Activation in Propulsion Induced by Electrical Stimulation in the Descending Colon of Rats," *Neuromodulation: Technology at the Neural Interface*, vol. 8, no. 2, pp. 131–140, Apr. 2005, doi: 10.1111/j.1525-1403.2005.00229.x.

[126] S. Chen *et al.*, "Effects of colonic electrical stimulation using different individual parameter patterns and stimulation sites on gastrointestinal transit time, defecation, and food intake," *Int J Colorectal Dis*, vol. 31, no. 2, pp. 429–437, Feb. 2016, doi: 10.1007/s00384-015-2457-6.

[127] M. A. Amaris, "Microprocessor controlled movement of solid colonic content using sequential neural electrical stimulation," *Gut*, vol. 50, no. 4, pp. 475–479, Apr. 2002, doi: 10.1136/gut.50.4.475.

[128] c. p. sanmiguel, s. casillas, a. senagore, m. p. mintchev, and e. e. soffer, "Neural gastrointestinal electrical stimulation enhances colonic motility in a chronic canine model of

delayed colonic transit," *Neurogastroenterol Motil*, vol. 18, no. 8, pp. 647–653, Aug. 2006, doi: 10.1111/j.1365-2982.2006.00783.x.

[129] S. Chen *et al.*, "Implantable Colonic Electrical Stimulation Improves Gastrointestinal Transit and Defecation in a Canine Constipation Model: Colonic Electrical Stimulation in Dogs," *Neuromodulation: Technology at the Neural Interface*, vol. 19, no. 1, pp. 108–115, Jan. 2016, doi: 10.1111/ner.12369.

[130] i. s. andersen, s. buntzen, n. j. m. rijkhoff, a. l. dalmose, j. c. djurhuus, and s. laurberg, "Ano-rectal motility responses to pelvic, hypogastric and pudendal nerve stimulation in the Gottingen minipig," *Neurogastroenterol Motil*, vol. 18, no. 2, pp. 153–161, Feb. 2006, doi: 10.1111/j.1365-2982.2005.00735.x.

[131] F. V. Møller, S. Buntzen, N. J. M. Rijkhoff, and S. Laurberg, "Pelvic Nerve Stimulation Evokes Nitric Oxide Mediated Distal Rectal Relaxation in Pigs," *Diseases of the Colon & Rectum*, vol. 51, no. 8, pp. 1261–1267, Aug. 2008, doi: 10.1007/s10350-008-9355-8.

[132] F. V. Møller, S. Buntzen, N. J. M. Rijkhoff, and S. Laurberg, "Rectal evacuation and antegrade colonic luminal transport by sacral anterior root stimulation in pigs.," *Dis Colon Rectum*, vol. 52, no. 9, pp. 1650–1656, Sep. 2009, doi: 10.1007/DCR.0b013e3181a872fb.

[133] J. Sobocki *et al.*, "Laparoscopically Implanted System for Stimulation of the Hypogastric Plexus Induces Colonic Motility, Defecation, and Micturition: Experimental Study," *Surg Innov*, vol. 22, no. 1, pp. 70–76, Feb. 2015, doi: 10.1177/1553350614530190.

[134] d. wattchow, s. brookes, e. murphy, s. carbone, d. de fontgalland, and m. costa, "Regional variation in the neurochemical coding of the myenteric plexus of the human colon

and changes in patients with slow transit constipation," *Neurogastroenterology & Motility*, vol. 20, no. 12, pp. 1298–1305, Dec. 2008, doi: 10.1111/j.1365-2982.2008.01165.x.

[135] J. Gonella, M. Bouvier, and F. Blanquet, "Extrinsic nervous control of motility of small and large intestines and related sphincters.," *Physiological Reviews*, vol. 67, no. 3, pp. 902–961, Jul. 1987, doi: 10.1152/physrev.1987.67.3.902.

[136] J. Delmas and J. G. Laux, "ANATOMIE MEDICO-CHIRURGICALE DU SYSTEME NERVEUX VEGETATIF. SYMPATHIQUE ET PARASYMPATHIQUE," *The Journal of Nervous and Mental Disease*, vol. 79, no. 2, 1934, [Online]. Available: https://journals.lww.com/jonmd/Fulltext/1934/02000/ANATOMIE_MEDICO_CHIRURGICALE_DU_SYSTEME_NERVEUX.90.aspx

[137] P. I. Collman, D. Grundy, and T. Scratcherd, "Vagal control of colonic motility in the anaesthetized ferret: evidence for a non-cholinergic excitatory innervation.," *The Journal of Physiology*, vol. 348, no. 1, pp. 35–42, Mar. 1984, doi: 10.1113/jphysiol.1984.sp015097.

[138] P.-E. Pahlin and J. Kewenter, "The Vagal Control of the Ileo-Cecal Sphincter in the Cat," *Acta Physiologica Scandinavica*, vol. 96, no. 4, pp. 433–442, Apr. 1976, doi: 10.1111/j.1748-1716.1976.tb10213.x.

[139] W. D. Tong, T. J. Ridolfi, L. Kosinski, K. Ludwig, and T. Takahashi, "Effects of autonomic nerve stimulation on colorectal motility in rats: Autonomic nerve stimulation and colorectal motility," *Neurogastroenterology & Motility*, vol. 22, no. 6, pp. 688–693, Jan. 2010, doi: 10.1111/j.1365-2982.2009.01461.x.

[140] G. Dubrovsky *et al.*, "Intestinal Electrical Stimulation to Increase the Rate of Peristalsis," *Journal of Surgical Research*, vol. 236, pp. 153–158, Apr. 2019, doi: 10.1016/j.jss.2018.11.044.

[141] Yi-Kai Lo, Chih-Wei Chang, and Wentai Liu, "Bio-impedance characterization technique with implantable neural stimulator using biphasic current stimulus," in *2014 36th Annual International Conference of the IEEE Engineering in Medicine and Biology Society*, Chicago, IL, Aug. 2014, pp. 474–477. doi: 10.1109/EMBC.2014.6943631.

[142] N. Stakenborg *et al.*, "Abdominal vagus nerve stimulation as a new therapeutic approach to prevent postoperative ileus," *Neurogastroenterol Motil*, vol. 29, no. 9, p. e13075, Sep. 2017, doi: 10.1111/nmo.13075.

[143] M. D. Unger, T. P. Maus, R. C. Puffer, L. K. Newman, B. L. Currier, and A. S. Beutler, "Laminotomy for Lumbar Dorsal Root Ganglion Access and Injection in Swine," *JoVE*, no. 128, p. 56434, Oct. 2017, doi: 10.3791/56434.

[144] R. T. Woodburne, "The sacral parasympathetic innervation of the colon," *Anat. Rec.*, vol. 124, no. 1, pp. 67–76, Jan. 1956, doi: 10.1002/ar.1091240105.

[145] T. C. Dudding, C. J. Vaizey, A. Gibbs, and M. A. Kamm, "Improving the efficacy of sacral nerve stimulation for faecal incontinence by alteration of stimulation parameters," *Br J Surg*, vol. 96, no. 7, pp. 778–784, Jul. 2009, doi: 10.1002/bjs.6637.

[146] V. Patton, L. Wiklendt, J. W. Arkwright, D. Z. Lubowski, and P. G. Dinning, "The effect of sacral nerve stimulation on distal colonic motility in patients with faecal incontinence: Sacral nerve stimulation for faecal incontinence," *Br J Surg*, vol. 100, no. 7, pp. 959–968, Jun. 2013, doi: 10.1002/bjs.9114.

[147] *Influence of Direct Colon Tissue Electrical Stimulation on Colonic Motility in Anesthetized Male Yucatan Minipig*. Blackfynn, 2020.

[148] "Regulation of gastrointestinal motility–insights from smooth muscle biology," *Nat Rev Gastroenterol Hepatol*, vol. 9, 2012.

[149] M. A. Maselli, A. L. Piepoli, G. Riezzo, and F. Pezzolla, "Motility, Nerve-Gut Interactions, Hormones, and Receptors-Motor Responsiveness of Proximal and Distal Human Colonic Muscle Layers to Carbachol and Neurotensin," *Digestive Diseases and Sciences*, vol. 43, no. 8, pp. 1685–1689, 1998.

[150] M. Corsetti *et al.*, "First translational consensus on terminology and definitions of colonic motility in animals and humans studied by manometric and other techniques," *Nat Rev Gastroenterol Hepatol*, vol. 16, no. 9, pp. 559–579, Sep. 2019, doi: 10.1038/s41575-019-0167-1.

[151] M. D. Crowell, F. Musial, W. French, D. Kittur, D. Anderson, and W. E. Whitehead, "Prolonged ambulatory monitoring of colonic motor activity in the pig," *Physiology & Behavior*, vol. 52, no. 3, pp. 471–474, Sep. 1992, doi: 10.1016/0031-9384(92)90332-V.

[152] J. Chen, G.-Q. Song, J. Yin, T. Koothan, and J. D. Z. Chen, "Electroacupuncture improves impaired gastric motility and slow waves induced by rectal distension in dogs," *American Journal of Physiology-Gastrointestinal and Liver Physiology*, vol. 295, no. 3, pp. G614–G620, Sep. 2008, doi: 10.1152/ajpgi.90322.2008.

[153] S. K. Sarna, B. L. Bardakjian, W. E. Waterfall, and J. F. Lind, "Human colonic electrical control activity (ECA).," *Gastroenterology*, vol. 78, no. 6, pp. 1526–1536, Jun. 1980.

[154] A. Shafik, “The motor efficacy of the artificial colonic pacemaker in colonic inertia patients,” *Front Biosci*, vol. 7, no. 2, pp. b6-13, 2002, doi: 10.2741/A754.

[155] D. Bourbeau, K. Aamoth, S. Brose, and K. Gustafson, “Electrical Colon Stimulation Reflexively Increases Colonic Activity,” *Neuromodulation: Technology at the Neural Interface*, vol. 23, no. 8, pp. 1130–1136, Dec. 2020, doi: 10.1111/ner.13035.

[156] P. G. Dinning *et al.*, “High-resolution colonic motility recordings *in vivo* compared with *ex vivo* recordings after colectomy, in patients with slow transit constipation,” *Neurogastroenterol. Motil.*, vol. 28, no. 12, pp. 1824–1835, Dec. 2016, doi: 10.1111/nmo.12884.

[157] K. Hipper and H. J. Ehrlein, “Motility of the large intestine and flow of digesta in pigs,” *Research in Veterinary Science*, vol. 71, no. 2, pp. 93–100, Oct. 2001, doi: 10.1053/rvsc.2001.0486.

[158] A. Luckey, E. Livingston, and Y. Tache, “Mechanisms and Treatment of Postoperative Ileus,” *ARCH SURG*, vol. 138, p. 9, 2003.

[159] P. A. Bampton and D. Z. Lubowski, “Prolonged Multi-Point Recording of Colonic Manometry in the Unprepared Human Colon: Providing Insight Into Potentially Relevant Pressure Wave Parameters,” vol. 96, no. 6, p. 11, 2001.

[160] S. K. Sarna, “Effect of fluid perfusion and cleansing on canine colonic motor activity,” *American Journal of Physiology-Gastrointestinal and Liver Physiology*, vol. 262, no. 1, pp. G62–G68, Jan. 1992, doi: 10.1152/ajpgi.1992.262.1.G62.

[161] C. E. J. Sloots and R. J. F. Felt-Bersma, “Effect of bowel cleansing on colonic transit in constipation due to slow transit or evacuation disorder,” *Neurogastroenterol Motil*, vol. 14, no. 1, pp. 55–61, Feb. 2002, doi: 10.1046/j.1365-2982.2002.00304.x.

[162] H. R. Berthoud, N. R. Carlson, and T. L. Powley, “Topography of efferent vagal innervation of the rat gastrointestinal tract,” *American Journal of Physiology-Regulatory, Integrative and Comparative Physiology*, vol. 260, no. 1, pp. R200–R207, Jan. 1991, doi: 10.1152/ajpregu.1991.260.1.R200.

[163] A. R. D. Bessant and J. Robertson-Rintoul, “Origin of the parasympathetic preganglionic fibers to the distal colon of the rabbit as demonstrated by the horseradish peroxidase method,” *Neuroscience Letters*, vol. 63, no. 1, pp. 17–22, Jan. 1986, doi: 10.1016/0304-3940(86)90005-4.

[164] G. Devroede and J. Lamarche, “Functional importance of extrinsic parasympathetic innervation to the distal colon and rectum in man.,” *Gastroenterology*, vol. 66, no. 2, pp. 273–280, Feb. 1974.

[165] S. Maruyama, S. Okabe, M. Endo, K. Sato, and T. Iwai, “The Role of the Rectal Branches of Pelvic Plexus in Defecation and Colonic Motility in a Canine Model,” *J Med Dent Sci*, p. 10.

[166] Y. Taché, T. Garrick, and H. Raybould, “Central nervous system action of peptides to influence gastrointestinal motor function,” *Gastroenterology*, vol. 98, no. 2, pp. 517–528, 1990.

[167] L. D. Hachem, H. Yan, and G. M. Ibrahim, “Invasive Neuromodulation for the Treatment of Pediatric Epilepsy,” *Neurotherapeutics*, vol. 16, no. 1, pp. 128–133, Jan. 2019, doi: 10.1007/s13311-018-00685-1.

[168] R. L. Johnson and C. G. Wilson, “A review of vagus nerve stimulation as a therapeutic intervention,” *JIR*, vol. Volume 11, pp. 203–213, May 2018, doi: 10.2147/JIR.S163248.

[169] A. Zanchetti, S. C. Wang, and G. Moruzzi, “The effect of vagal afferent stimulation on the EEG pattern of the cat,” *Electroencephalography and clinical neurophysiology*, vol. 4, no. 3, pp. 357–361, 1952.

[170] P.-O. Andersson, S. R. Bloom, A. V. Edwards, and J. Jarhult, “Effects of stimulation of the chorda tympani in bursts on submaxillary responses in the cat,” *The Journal of Physiology*, vol. 322, no. 1, pp. 469–483, Jan. 1982, doi: 10.1113/jphysiol.1982.sp014050.

[171] D. Grundy and T. Scratcherd, “Effect of stimulation of the vagus nerve in bursts on gastric acid secretion and motility in the anaesthetized ferret.,” *The Journal of Physiology*, vol. 333, no. 1, pp. 451–461, Dec. 1982, doi: 10.1113/jphysiol.1982.sp014463.

[172] R. I. Birks, “A long-lasting potentiation of transmitter release related to an increase in transmitter stores in a sympathetic ganglion,” *The Journal of Physiology*, vol. 271, no. 3, pp. 847–862, Oct. 1977, doi: 10.1113/jphysiol.1977.sp012028.

[173] E. A. Tanagho, R. A. Schmidt, and B. R. Orvis, “Neural Stimulation for Control of Voiding Dysfunction: A Preliminary Report in 22 Patients with Serious Neuropathic Voiding Disorders,” *The Journal of Urology*, vol. 142, no. 2, Part 1, pp. 340–345, Aug. 1989, doi: 10.1016/S0022-5347(17)38751-7.

[174] K. Noblett *et al.*, "Results of a prospective, multicenter study evaluating quality of life, safety, and efficacy of sacral neuromodulation at twelve months in subjects with symptoms of overactive bladder," *Neurourol. Urodynam.*, vol. 35, no. 2, pp. 246–251, Feb. 2016, doi: 10.1002/nau.22707.

[175] W. C. de Groat, I. Nadelhaft, R. J. Milne, A. M. Booth, C. Morgan, and K. Thor, "Organization of the sacral parasympathetic reflex pathways to the urinary bladder and large intestine," *Journal of the Autonomic Nervous System*, vol. 3, no. 2–4, pp. 135–160, Apr. 1981, doi: 10.1016/0165-1838(81)90059-X.

[176] E. Ganio *et al.*, "Neuromodulation for fecal incontinence: Outcome in 16 patients with definitive implant: The initial italian sacral neurostimulation group (GINS) experience," *Diseases of the Colon & Rectum*, vol. 44, no. 7, pp. 965–970, Jul. 2001, doi: 10.1007/BF02235484.

[177] E. Ganio *et al.*, "Short-term sacral nerve stimulation for functional anorectal and urinary disturbances: Results in 40 patients: Evaluation of a new option for anorectal functional disorders," *Diseases of the Colon & Rectum*, vol. 44, no. 9, pp. 1261–1267, Sep. 2001, doi: 10.1007/BF02234782.

[178] G. Gourcerol, V. Vitton, A. M. Leroi, F. Michot, A. Abysique, and M. Bouvier, "How sacral nerve stimulation works in patients with faecal incontinence: Mechanisms of action of SNS," *Colorectal Disease*, vol. 13, no. 8, pp. e203–e211, Aug. 2011, doi: 10.1111/j.1463-1318.2011.02623.x.

[179] W. C. De Groat and J. Krier, “The sacral parasympathetic reflex pathway regulating colonic motility and defaecation in the cat.,” *The Journal of Physiology*, vol. 276, no. 1, pp. 481–500, Mar. 1978, doi: 10.1113/jphysiol.1978.sp012248.

[180] G. Wallin, J. Cassuto, S. Högström, G. Rimbäck, A. Faxén, and P. O. Tollesson, “Failure of epidural anesthesia to prevent postoperative paralytic ileus.,” *Anesthesiology*, vol. 65, no. 3, pp. 292–297, Sep. 1986.

[181] A. Sato, Y. Sato, A. Suzuki, and S. Uchida, “Neural mechanisms of the reflex inhibition and excitation of gastric motility elicited by acupuncture-like stimulation in anesthetized rats,” *Neuroscience Research*, vol. 18, no. 1, pp. 53–62, Oct. 1993, doi: 10.1016/0168-0102(93)90105-Y.

[182] M. Sawan, M. M. Hassouna, Jin-Sheng Li, F. Duval, and M. M. Elhilali, “Stimulator design and subsequent stimulation parameter optimization for controlling micturition and reducing urethral resistance,” *IEEE Transactions on Rehabilitation Engineering*, vol. 4, no. 1, pp. 39–46, Mar. 1996, doi: 10.1109/86.486056.

[183] K. L. Kilgore and N. Bhadra, “Reversible Nerve Conduction Block Using Kilohertz Frequency Alternating Current,” *Neuromodulation: Technology at the Neural Interface*, vol. 17, no. 3, pp. 242–255, Apr. 2014, doi: 10.1111/ner.12100.

[184] A. Vučković and N. J. M. Rijkhoff, “Different pulse shapes for selective large fibre block in sacral nerve roots using a technique of anodal block: An experimental study,” *Medical & Biological Engineering & Computing*, vol. 42, no. 6, pp. 817–824, Nov. 2004, doi: 10.1007/BF02345216.

[185] N. Thompson, S. Mastitskaya, and D. Holder, “Avoiding off-target effects in electrical stimulation of the cervical vagus nerve: Neuroanatomical tracing techniques to study fascicular anatomy of the vagus nerve,” *Journal of Neuroscience Methods*, vol. 325, p. 108325, Sep. 2019, doi: 10.1016/j.jneumeth.2019.108325.

[186] P. G. Dinning *et al.*, “Bowel preparation affects the amplitude and spatiotemporal organization of colonic propagating sequences: Bowel preparation and colonic motility,” *Neurogastroenterology & Motility*, vol. 22, no. 6, pp. 633-e176, Feb. 2010, doi: 10.1111/j.1365-2982.2010.01480.x.

[187] J. W. Arkwright *et al.*, “The effect of luminal content and rate of occlusion on the interpretation of colonic manometry: Effect of luminal content on manometry,” *Neurogastroenterology & Motility*, vol. 25, no. 1, pp. e52–e59, Jan. 2013, doi: 10.1111/nmo.12051.

[188] C. Dagdeviren *et al.*, “Flexible piezoelectric devices for gastrointestinal motility sensing,” *Nat Biomed Eng*, vol. 1, no. 10, pp. 807–817, Oct. 2017, doi: 10.1038/s41551-017-0140-7.

[189] B. Kothapalli, “Origin of changes in the epigastric impedance signal as determined by a three-dimensional model,” *IEEE Trans. Biomed. Eng.*, vol. 39, no. 10, pp. 1005–1010, Oct. 1992, doi: 10.1109/10.161332.

[190] A. J. P. M. Smout, H. J. A. Jebbink, L. M. A. Akkermans, and P. P. M. Bruijs, “Role of electrogastrography and gastric impedance measurements in evaluation of gastric emptying and motility,” *Digest Dis Sci*, vol. 39, no. S12, pp. 110S-113S, Dec. 1994, doi: 10.1007/BF02300387.

[191] Z. Li and C. Ren, “Gastric motility measurement and evaluation of functional dyspepsia by a bio-impedance method,” *Physiol. Meas.*, vol. 29, no. 6, pp. S373–S382, Jun. 2008, doi: 10.1088/0967-3334/29/6/S31.

[192] M.-R. Huerta-Franco *et al.*, “Effects of metoclopramide on gastric motility measured by short-term bio-impedance,” *WJG*, vol. 15, no. 38, p. 4763, 2009, doi: 10.3748/wjg.15.4763.

[193] R. Huerta-Franco, M. Vargas-Luna, E. Hernandez, K. Capaccione, and T. Cordova, “Use of short-term bio-impedance for gastric motility assessment,” *Medical Engineering & Physics*, vol. 31, no. 7, pp. 770–774, Sep. 2009, doi: 10.1016/j.medengphy.2009.02.008.

[194] P. Aelen, A. Jurkov, A. Aulanier, and M. P. Mintchev, “Pilot acute study of feedback-controlled retrograde peristalsis invoked by neural gastric electrical stimulation,” *Physiol. Meas.*, vol. 30, no. 3, pp. 309–322, Mar. 2009, doi: 10.1088/0967-3334/30/3/006.

[195] Y.-K. Lo, J. Wagner, C.-W. Chang, J. D. Rouch, J. Dunn, and W. Liu, “619 Single-Electrode Colon Stimulation and Impedance Monitoring in an Intestinal Aganglionosis Model,” *Gastroenterology*, vol. 148, no. 4, p. S-121-S-122, Apr. 2015, doi: 10.1016/S0016-5085(15)30422-4.

[196] J. E. B. Randles, “Kinetics of rapid electrode reactions,” *Discuss. Faraday Soc.*, vol. 1, p. 11, 1947, doi: 10.1039/df9470100011.

[197] A. Lasia, “Electrochemical Impedance Spectroscopy and its Applications,” in *Modern Aspects of Electrochemistry*, vol. 32, B. E. Conway, J. O. Bockris, and R. E. White, Eds. Boston: Kluwer Academic Publishers, 2002, pp. 143–248. doi: 10.1007/0-306-46916-2_2.

[198] D. R. Merrill, "The Electrochemistry of Charge Injection at the Electrode/Tissue Interface," in *Implantable Neural Prostheses 2*, D. Zhou and E. Greenbaum, Eds. New York, NY: Springer New York, 2010, pp. 85–138. doi: 10.1007/978-0-387-98120-8_4.

[199] F. B. Hu, J. Goldberg, D. Hedeker, B. R. Flay, and M. A. Pentz, "Comparison of Population-Averaged and Subject-Specific Approaches for Analyzing Repeated Binary Outcomes," *American Journal of Epidemiology*, vol. 147, no. 7, pp. 694–703, Apr. 1998, doi: 10.1093/oxfordjournals.aje.a009511.

[200] J. A. Hanley, "Statistical Analysis of Correlated Data Using Generalized Estimating Equations: An Orientation," *American Journal of Epidemiology*, vol. 157, no. 4, pp. 364–375, Feb. 2003, doi: 10.1093/aje/kwf215.

[201] G. A. Ballinger, "Using Generalized Estimating Equations for Longitudinal Data Analysis," *Organizational Research Methods*, vol. 7, no. 2, pp. 127–150, Apr. 2004, doi: 10.1177/1094428104263672.

[202] Y. Ma, M. Mazumdar, and S. G. Memtsoudis, "Beyond Repeated-Measures Analysis of Variance: Advanced Statistical Methods for the Analysis of Longitudinal Data in Anesthesia Research," *Reg Anesth Pain Med*, vol. 37, no. 1, p. 99, Jan. 2012, doi: 10.1097/AAP.0b013e31823ebc74.

[203] R. J. Strand-Amundsen *et al.*, "*In vivo* characterization of ischemic small intestine using bioimpedance measurements," *Physiol. Meas.*, vol. 37, no. 2, pp. 257–275, Feb. 2016, doi: 10.1088/0967-3334/37/2/257.

[204] A. Uranga, J. Sacristan, T. Oses, and Nú. Barniol, "Electrode–Tissue Impedance Measurement CMOS ASIC for Functional Electrical Stimulation Neuroprostheses," *IEEE*

Trans. Instrum. Meas., vol. 56, no. 5, pp. 2043–2050, Oct. 2007, doi: 10.1109/TIM.2007.904479.

[205] S. F. Cogan, "Neural Stimulation and Recording Electrodes," *Annu. Rev. Biomed. Eng.*, vol. 10, no. 1, pp. 275–309, Aug. 2008, doi: 10.1146/annurev.bioeng.10.061807.160518.

[206] R. F. Yazicioglu, S. Kim, T. Torfs, H. Kim, and C. Van Hoof, "A 30 μW Analog Signal Processor ASIC for Portable Biopotential Signal Monitoring," *IEEE J. Solid-State Circuits*, vol. 46, no. 1, pp. 209–223, Jan. 2011, doi: 10.1109/JSSC.2010.2085930.

[207] Y.-T. Li, C.-W. Peng, L.-T. Chen, W.-S. Lin, C.-H. Chu, and J.-J. J. Chen, "Application of Implantable Wireless Biomicrosystem for Monitoring Nerve Impedance of Rat After Sciatic Nerve Injury," *IEEE Trans. Neural Syst. Rehabil. Eng.*, vol. 21, no. 1, pp. 121–128, Jan. 2013, doi: 10.1109/TNSRE.2012.2219883.

[208] S. Culaclii, B. Kim, Y.-K. Lo, L. Li, and W. Liu, "Online Artifact Cancelation in Same-Electrode Neural Stimulation and Recording Using a Combined Hardware and Software Architecture," *IEEE Trans. Biomed. Circuits Syst.*, vol. 12, no. 3, pp. 601–613, Jun. 2018, doi: 10.1109/TBCAS.2018.2816464.

[209] B. Colson, P. Marcotte, and G. Savard, "An overview of bilevel optimization," *Ann Oper Res*, vol. 153, no. 1, pp. 235–256, Jun. 2007, doi: 10.1007/s10479-007-0176-2.

[210] K. Kunisch and T. Pock, "A Bilevel Optimization Approach for Parameter Learning in Variational Models," *SIAM J. Imaging Sci.*, vol. 6, no. 2, pp. 938–983, Jan. 2013, doi: 10.1137/120882706.

[211] R. Marbach and H. M. Heise, “Calibration modeling by partial least-squares and principal component regression and its optimization using an improved leverage correction for prediction testing,” *Chemometrics and Intelligent Laboratory Systems*, vol. 9, no. 1, pp. 45–63, Aug. 1990, doi: 10.1016/0169-7439(90)80052-8.

[212] N. Nguyen, P. Milanfar, and G. Golub, “Efficient generalized cross-validation with applications to parametric image restoration and resolution enhancement,” *IEEE Trans. on Image Process.*, vol. 10, no. 9, pp. 1299–1308, Sep. 2001, doi: 10.1109/83.941854.